PROGRESS TOWARD GROUND-STATE SODIUM-RUBIDIUM MOLECULES

BY

MICHAEL A. HIGHMAN

DISSERTATION

Submitted in partial fulfillment of the requirements
for the degree of Doctor of Philosophy in Physics
in the Graduate College of the
University of Illinois Urbana-Champaign, 2022

Urbana, Illinois

Doctoral Committee:

Professor Brian DeMarco, Chair
Associate Professor Bryce Gadway, Director of Research
Assistant Professor Elizabeth Goldschmidt
Associate Professor Eric Chitambar

Abstract

In the last decade, ultracold polar molecules have emerged as one of the most exciting experimental platforms for the discovery of new physics and chemistry. Their complex internal structure, comprised of many kinds of states at vastly different energy scales, makes them well suited for a wide variety of scientific applications. In particular, ultracold molecules are promising candidates for tests of fundamental physics, quantum simulation and computation, and quantum chemistry. In this thesis we report on experimental progress in our lab toward the creation of ro-vibrational ground state sodium-rubidium (^{23}Na^{87}Rb) molecules. We explain the roadmap to their creation by first cooling ^{23}Na and ^{87}Rb gases, associating them into loosely bound molecules via the use of a Feshbach resonance, and lastly bringing them to their ro-vibrational ground state using Stimulated Raman Adiabatic Passage (STIRAP). Additionally, we detail a parallel theoretical effort to address the ability to nondestructively image rotationally excited ultracold molecules. This is done by using the molecule's inherent birefringence to rotate the polarization of a probing laser field. We thoroughly analyze the molecular states within the ground and first electronic excited potentials of ^{23}Na^{87}Rb and summarize the effectiveness of our proposed imaging scheme by choosing three promising probe laser wavelengths. Upon realization of ground state ^{23}Na^{87}Rb, we aim to demonstrate our imaging technique. We also discuss the next immediate experimental steps toward the realization of this goal.

For my mom

Acknowledgments

This may be the hardest section of this thesis for me to write. The adage "it takes a village" simply could not be more true. Unfortunately, in making a list of people to acknowledge there will inevitably be some that should have been mentioned that were not. If you are one of these people, I hope you accept my apology and recognize that you too are important. However, I will do my best to be thorough now.

First and foremost I would like to thank my advisor Bryce Gadway. Bryce has been a fantastic advisor since the first day – he is someone I feel both respects me intellectually and respects my time and commitments in life outside of our research. I've felt nothing but support and encouragement from Bryce through all the highs and lows that naturally occur in a graduate career. I've learned *so much* under his tutelage, and I will be forever grateful for my time in his lab.

Next, I would like to thank my committee, starting with my co-advisor and committee Chair, Brian DeMarco. I have learned an incredible amount from Brian. He has a way of making you really consider how well you know something, and simultaneously he has shown me great compassion and provided pointed wisdom when I needed it most. My thanks to Elizabeth Goldschmidt, too, for being one of the best teachers I think I've ever met. Elizabeth can explain just about anything in a crystal clear way, all the while providing a good laugh and conversation. Lastly, I would like to thank Eric Chitambar. I would like to think we'd have had more interaction if it weren't for that... uhh... *global pandemic*, but your time serving in my prelim and thesis defense is greatly appreciated.

On to the Gadway Lab! Garrett Williams has been my partner in the molecule experiment since Fall 2019 and I'm so incredibly grateful for it. Garrett wears passion on his face, sleeve, you name it. I don't know another person who so genuinely wants to *know* ("know what?" you may ask – everything). The experiment is in good hands with him. Thank you

for the years of laughs and companionship on our side of the lab. Next I'd like to thank Shraddha Agrawal. She is such a good friend, is incredibly funny, smart, and driven. She's been a voice of reason for me ever since we started working together. Sai Paladugu, as well, has been a true day one friend since Jim's E&M class all the way to now. Simon, Chen, Tao, and Ivan, I'm grateful for the time we've overlapped in lab. To those who were undergraduates during my time (some in grad school themselves, now!) Rithi, Hannah M and U, Sam, Frankie, Lingfeng, Yuhao, Autumn, Yaashnaa, Antonio, Jiarui, Jessie, and Devont – thank you.

To the now graduated Gadway Lab members Eric J. Meier, Fangzhao Alex An, and Jackson Okech Ang'ong'a – thank you. The three of you are firmly cemented in my heart as close friends with too many good memories to count. Any conversation with these three is just rapid fire inside jokes that are genuinely not funny to anyone except us. I'm happy that although we've scattered just about as far away from one another geographically as possible, that we still maintain regular (with Eric and Alex, daily) contact. Release the Barcelona Tapes!!

Next, others I've met at Illinois. I must first thank Kristina Meier as both she and Eric were my first true friends when I moved in from Ohio. I will always be forever grateful for them in ways words rarely do justice. Next, my longtime roommate and good friend Colin Lualdi. In addition to being a kind soul and a great housemate, you even taught me American Sign Language! I don't know how many people can say they learned a new language in graduate school, but I'm a lucky one who did. Thank you to Spencer Johnson for being a wonderful friend (and gamer). I would like to thank Lance Cooper for being, and I mean this seriously, the *best* graduate program head in the world. His advising, compassion, and patience is simply unmatched. To those who keep (or kept) the gears greased at the physics department such as Elaine Schulte, Kate Shunk, Matthew Macaraeg, DaShawnique Long, Wendy Wimmer, Nicolette Elam, Jerry Cook, Luke Prunkard, Cheryl Sabas, Susan Logan, Debbie McCarter, Tommie Wininger, and Doug Jeffers, thank you. Ellen Althaus has also provided me copious wisdom as my Sloan Academic Advisor and is another example of someone who has always had a positive influence on me. Also, I thank the National Science Foundation and the Sloan Foundatation for their years of funding.

I'd like to thank the many others who have helped me maintain my sanity through both graduate school and the aforementioned *global pandemic*. To this end are my two best friends in the world from Otterbein University, John Brandon and Evan Heintz. I want to thank my girlfriend Corrinne Spring for her support, both in real life and in Fortnite. And on that note, a thank you to my good friend and social butterfly Morgan Thompson. I would like to thank my undergraduate advisor Aaron Reinhard for his never-ending support. I also want to mention those who I've run with in the Second Wind Running Club, my kind bartenders at Riggs Brewery, Smitha Vishveshwara, Latrelle Bright, and the various casts of Quantum Voyages, my two incredibly talented tattoo artists Rick Kutch and Justin McCarty, and the Discord server I joined in January 2021 filled with fantasy reading fans who have all become so important to me (there's ≈ 50 of us who are regularly active so I'll spare the names, but you know who you are). Additionally, my friends Chris Warman and Élan Marché, authors of *Seasons of Albadone*, who allowed me the opportunity to narrate their book in 2021.

Last, but certainly not least, I would like to thank my family. My mother and father, Laura and Joe, have shown me nothing but love and support and are the pillars on which I stand today. I unfortunately do not possess the linguistic skills to express the depth of my gratitude to them. To grandpa Humberto and grandma Linda, Grams and Pops, grandma Mireille, Maddie, Andrew, Tanya, Zinn, Calib, Mini, Nicole, Diane, Teresa, Howard, to everyone – I love you and I'm sorry I don't call enough. Without the twenty-seven years of support my family has given me I would be nowhere near the person I am today.

Table of Contents

List of Figures

Chapter 1

Introduction

Located on the third floor of the Loomis Laboratory in Urbana, Illinois lies an apparatus that is progressing toward the generation of ground state sodium-rubidium (^{23}Na^{87}Rb) molecules. In 2017 in that very same room one would have seen two empty optical tables. This story is likely common amongst many other groups within the sphere of atomic, molecular, and optical physics. The rise of ultracold molecules has been quite incredible over the last two decades. The techniques for laser cooling and trapping atoms have advanced to the level where it is now possible to take mixtures of ultracold atomic gases and form them into ultracold molecules. Certain types of molecules can even be directly laser cooled in and of themselves. It's an exciting time to be in the field as ultracold molecules start to fit more comfortably into the physicist's toolbox for understanding the natural world.

Though there is still an immense amount of physics knowledge to be gained from ultracold atom experiments, in many ways the parallel development of ultracold molecule physics was inevitable. Nature likes to form molecules and crystals, as evidenced by the fact that you, the reader, are a collection of primarily molecular and crystalline structures. Very rarely are free atoms seen in nature, even the air we breathe is primarily composed of N_2 and O_2 molecules. This is because most atoms lower their summed energy by forming a molecular bond and releasing the remaining energy as light or kinetic energy of a spectating particle. In a universe that only ever increases entropy, the release of this internal energy into motional energy of some kind is almost always favored. In many ways, studying molecules brings us closer to the type of matter our universe prefers. We are now in a unique position to truly understand the quantum mechanical nature of molecules as we bring them to ultracold temperatures. Chemists and physicists can rejoice as the techniques for incredible quantum state control of atoms is now applicable to molecules, unleashing an entire new space of exploration into new physics and chemistry.

1.1 Ultracold Molecules

A running joke in the field of atomic physics is that a molecule is "one or more atoms too many." As I've come to work on an apparatus that has ambitions of creating molecules, in many ways I deeply relate to this joke. However, for the sliver of truth that it contains, it's also wrong. Molecules are a veritable playground for studying a vast array of physics. The *reason* for this joke is that molecules have a diverse set of internal states, each with unique energy scales and decay properties that typically make standard laser cooling and trapping techniques ineffective. However, in order to understand molecules, we must first understand these states.

1.1.1 Molecular States

Starting at the most energetically separated, and similar to their atomic counterparts, molecules have electronic states. The lowest lying of these are accessible from the electronic ground state via the use of laser light in the optical or near-infrared frequencies. For molecules, though, the energy of the electronic orbitals depends on the spatial separation of the constituent nuclei. Let us consider the energy of one sodium and one rubidium atom in their ground states. When the atoms are very far apart from one another we can treat their energy as simply the sum of the $3S_{1/2}$ and $5S_{1/2}$ energies, and we can say the energy of this sum is arbitrarily zero. With that reference, we can coarsely approximate the ground state electronic energy as a function of internuclear separation and consider the canonical Lennard-Jones potential seen in Equation 1.1 [1]:

$$V(r) = 4\epsilon \left[\left(\frac{\sigma}{r}\right)^{12} - \left(\frac{\sigma}{r}\right)^{6} \right]. \tag{1.1}$$

Here, σ is the distance corresponding to the zero-point in energy on the repulsive side of the potential, r is the separation of the nuclei, and ϵ is the depth of the potential. The Lennard-Jones potential qualitatively captures the short-range repulsion and intermediate-range attraction of multi-electron molecules. In the case of ^{23}Na^{87}Rb, the first term relates to the repulsive effects of Pauli exclusion and Coulomb repulsion of the two electrons, while

second term captures the induced dipole-dipole van der Waals attraction of the two neutral atoms. Though the Lennard-Jones potential is a simple phenomenological model, in general the structure of electronic molecular potentials is significantly more complicated. More sophisticated tools such as Molpro have been developed to give the most accurate form of these potentials.

As we know from quantum mechanics, if there is a potential well, there are bound states. To a good approximation, the Lennard-Jones potential can be described as a simple harmonic oscillator with corresponding simple-harmonic oscillator wavefunctions. A helpful picture one can consider is fixing one of the two atoms in the molecule at position zero while the other bounces around between the two walls of the potential. These harmonic oscillator solutions are the vibrational states. In the bi-alkali molecules these vibrational levels are separated in energy at the THz level, approximated by $E_{\text{vib}} \sim \sqrt{m_e/\mu}(e^2/a_0) \sim 10^{-2}E_{\text{el}}$ where m_e is the electron mass, μ is the reduced mass of the two nuclei, e is the fundamental charge, E_{el} is the energy of a low lying electronic excitation, and a_0 the Bohr radius [2].

In addition to the vibrational energy levels, molecules have other degrees of freedom that atoms do not that imbue them with other states. The next property to consider is the fact that the atoms constituting the molecule can rotate about their center of mass. For low-lying vibrational states, where the atoms in the molecule can be approximated as having a fixed distance, one can find the energies of the rotational states using the quantum rigid rotor Hamiltonian. Here, the diatomic molecule is treated as a single object with a reduced mass μ and moment of inertia I as given by $I = \mu R^2$ for a nuclear separation R. The solutions to this Hamiltonian are the spherical harmonics [3]. The energy separation of the rotational states is given by the characteristic $E = BJ(J+1)$ where $B = \hbar^2/2I$. For the bi-alkali molecules, it is common to find rotational constants, B/h, on the order of GHz. The eigenstates of the rigid rotor Hamiltonian have both the rotational angular momentum quantum number, J, as well as the projection of the angular momentum along a quantization axis, m_J.

Last, but certainly not least, are the nuclear hyperfine spin projection states. These states correspond to the many possible electron energies that depend on the magnetic spin orientation of the nuclei that compose the molecule. They arise due to the interaction of the

nuclear magnetic moment ($\mu_N \sim \mu_e(m_e/m_p)$) with the electron spin. For bi-alkali molecules in large magnetic fields (which are typically present to stabilize the molecules after their creation in the vicinity of a Feshbach resonance) the nuclear hyperfine projection states have energy separations on the order of kHz to MHz. In total, the number of projection states in a particular rotational level J of a diatomic molecule can be given by $(2J+1)(2I_1+1)(2I_2+1)$, where $I_{1,2}$ is the nuclear spin of nuclei 1 and 2, respectively.

Sodium-rubidium in its ro-vibrational ground state ($v = 0, J = 0, I_{\mathrm{Rb}} = I_{\mathrm{Na}} = 3/2$) has 16 different nuclear hyperfine spin states. In the first excited rotational level there are 48 such states. Considering that there are rotational states that exist within every vibrational level, one immediately sees that molecules have an incredible number of states. However, in spite of this, modern ultracold molecule physicists are capable of resolving and populating these myriad of states at will.

As a helpful picture, in Figure 1.1 we represent the energy separations of these states in a cartoon diagram against their equivalent temperatures. These units are chosen to underscore the fact that *ultracold* molecules at 10^{-4} K and below have thermal populations of their many internal states "frozen out," and we as experimentalists can coherently control these various state populations as desired.

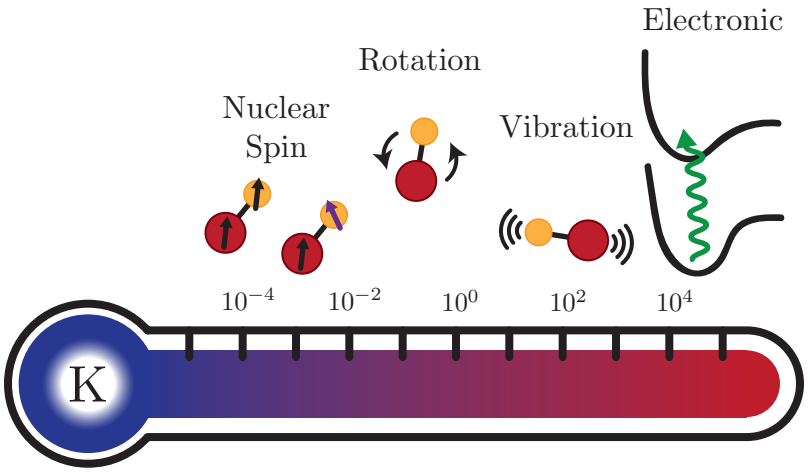

Figure 1.1: Molecular internal state temperature (energy) scales. Electronic energy level spacings occur at energies corresponding to $\sim 10^3$ Kelvin. Vibrational modes are excited around 10^2 K, rotational at $\sim 10^{-1}$ K, and nuclear spin state excitations at $\sim 10^{-6} - 10^{-2}$ K. Motional energy scales of ultracold molecules can be made far lower than any of these internal energies.

Typically, molecular states are written to varying degrees of specificity using the following notation:

$$|\psi\rangle_{\text{molecule}} = {}^{2S+1}\Lambda^{\pm}_{\Omega}|v, J, m_J, m_{I,1}, m_{I,2}\rangle. \tag{1.2}$$

For the bi-alkali molecules with two valence electrons, the top left $2S+1$ term is either a one or three for singlet and triplet spin configurations, respectively. Λ is the projection of the orbital angular momentum along the internuclear axis, and due to its similarity with atoms they are suggestively labeled $\Sigma, \Pi, \Delta, \ldots$ corresponding to $S, P, D, \ldots$ in the bare atom case. The $\pm$ denotes reflection symmetry of the molecular state about its internuclear axis, positive for symmetric and negative for anti-symmetric. Last, for the electronic state labeling, is Ω, that gives the projection of the total angular momentum about the internuclear axis. Within the ket lie the quantum numbers for the vibrational level v, the rotational level J, the projection of the rotational state along a quantization axis m_J, and the respective projections of the nuclear spins for the first and second nuclei $m_{I(1,2)}$.

Now, with an understanding of what the molecular states are, we can turn our attention to their creation.

1.1.2 Ultracold Molecule Creation

There are two dominant methods for creating ultracold molecules. The first is a "top-down" approach, wherein one starts with a hot gas of the molecule that needs to be cooled and applies some direct cooling mechanisms to bring them to ultracold temperatures. The second is a "bottom-up" technique, wherein the constituent atoms of the molecule are pre-cooled and then coerced into forming molecules via magneto- or photo-association.

With respect to the top-down technique, many creative mechanisms for cooling molecules have been developed. As a result of the vast number of states molecules have, especially vibrational levels that do not obey dipole selection rules, the standard approaches to laser cooling and trapping atoms are typically ineffective. As such, many top-down techniques rely on taking a beam-like source of molecules that is generally quite hot (as a result of heating in an oven, laser ablation, etc.) and applying some technique to slow them down. Nearly

all top-down approaches start with some implementation of buffer gas cooling [4, 5], with some applying additional techniques such as Stark deceleration [6, 7] (for polar molecules) or centrifuge deceleration [8]. In addition, for molecules that have a so-called inverted level structure, these techniques can be combined with laser cooling to create ultracold samples. Two "laser-coolable" molecules that have risen to prominence in the last few years are CaF [9, 10] and SrF [11].

To the creation of ultracold molecules via the bottom-up approach, there are two dominant strategies. The first is magneto-association via the use of a Feshbach resonance between pairs of ultracold atoms. This will be described more explicitly in Chapter 4, however the core of the idea is that the application of a magnetic field around a Feshbach resonance allows for an energetic tuning of the free atom collisional state such that it is degenerate with a loosely-bound state of their molecule. More specifically, near the resonance there is an avoided crossing between the free-atom scattering state and the bound state of the molecule and upon sweeping the magnetic field slowly enough through the resonance the atoms can be converted to bound molecules via adiabatic rapid passage. From there, a coherent two-photon process known as Stimulated Raman Adiabatic Passage (STIRAP) can be used to transfer the molecules to their ro-vibrational ground state. At a high level, this is diagrammed in Figure 1.2.

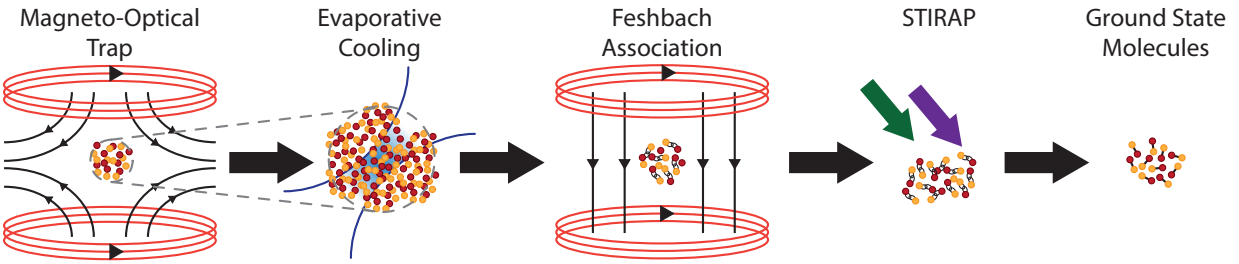

Figure 1.2: High level cartoon detailing the process by which ultracold molecules are created in their ro-vibrational ground state starting from an ultracold gas of atoms. Two atomic species are formed into a magneto-optical trap. Some form of sub-Doppler and evaporative cooling occur to bring their temperatures down and densities up for efficient creation of Feshbach molecules. The loosely-bound Feshbach molecules are then brought to their ro-vibrational ground state via the process of Stimulated Raman Adiabatic Passage.

The second mechanism for bottom-up molecule creation is photoassociation (PA). PA is the process of resonantly driving the two atom scattering state into a loosely bound and often short-lived electronically excited molecular state. Nominally, the rate of this molecule

creation scheme is quite low, and more complicated implementations of PA must be used in order to efficiently create ro-vibrational ground state molecules.

Lastly, ultracold molecules have begun appearing in setups utilizing optical tweezer arrays, one of the newest and most promising toolbox additions in atomic physics that has risen to prominence in the last 5-6 years. In Ref. [12] individually trapped sodium and cesium in optical tweezers were merged together and then Feshbach associated. As well, in Ref. [10] CaF was held and imaged an optical tweezer array. Molecules are rapidly catching up to atoms in their candidacy for exploring new physics. With the ability to create gases in well defined and controllable quantum states, the achievement of quantum degeneracy [13, 14], and the ability to be held and imaged at the single particle level, we can now turn our attention to the myriad of applications for ultracold molecules.

1.1.3 Applications of Ultracold Molecules

Ultracold molecules are an extraordinarily promising platform on which to discover new physics. In particular, molecules that are heteronuclear, or formed by atoms that have different electronegativities, have an additional layer of complexity that has not yet been mentioned that suit them to some interesting applications. When a heteronuclear molecule is formed there is a natural charge separation that leads to the creation of a permanent electric dipole moment. From here, we'll use the term polar molecule to describe this configuration.

Polar molecules have an inherent charge separation that results in massive internal electric fields, especially in comparison to what can be reasonably created in a laboratory setting. This fact has been utilized to a great deal of success by the ACME collaboration at Harvard, which employed ThO^+'s internal electric field to provide, to date, the best upper limit on the size of the electron electric dipole moment. This is an important measurement in understanding the Standard Model of Particle Physics [15]. Indeed, there are many prospects for utilizing properties of molecules to perform tests of fundamental physics [16].

Polar molecules interact via their dipole-dipole interaction. Clearly, this is quite useful in the study of dipolar spin physics. This interaction manifests in the rotational degree of freedom, wherein molecules in adjacent rotational states (i.e. $J_1 = 0, J_2 = 1$, or $J_1 = 1, J_2 =$

2, etc.) can exchange their internal rotational degrees of freedom back and forth. The dipole-dipole interaction in its simplest form, as in the case of fixed dipoles with conserved angular momentum, is shown below in Equation 1.3:

$$H_{\mathrm{dd}} = \sum_{i>j} J_{\perp} \frac{1 - 3\cos^2\theta_{ij}}{|r_i - r_j|^3} \left(\hat{S}_i^+ \hat{S}_j^- + \hat{S}_i^- \hat{S}_j^+ \right). \tag{1.3}$$

Here, $\hat{S}_i^{\pm}$ are the raising/lowering (pseudo)spin angular momentum operators (defined in relation to the appropriate rotational states that represent spin up and down) for molecule i, θ_{ij} is the angle between a quantization axis (usually set by a magnetic field) and the vector connecting molecules i and j, $J_{\perp} = -d^2/4\pi\epsilon_0$ where $d = \langle b|d|a\rangle$ is the dipole matrix element connecting states $|a\rangle$ and $|b\rangle$, and ϵ_0 the electric constant [17]. There are several properties of this "Heisenberg XX" interaction worth noting: it is long ranged, tunable either by adjusting the inter-molecular distance or angular configuration, and maximally entangling [18].

Coherent control of rotational states in polar molecules is of great interest to many different scientific goals. A few of the properties of rotational states that make them so enticing are:

1. Gigahertz frequency electric fields needed to address transitions between rotational states are easily synthesized by current microwave technologies. (In the language of quantum information science, this is the ability to perform arbitrary single qubit gates.)

2. Rotational states are effectively infinitely "long-lived" and demonstrate coherence times of a few to many milliseconds [19, 20].

3. In singlet electronic potentials these states are practically insensitive to stray magnetic fields, a common source of noise in many experiments. And while rotational states are sensitive to large electric fields, these do not typically occur by chance in experiment [21].

Polar molecules are well suited to explore a great range of different physics given that the rotational states inherently have such nice properties and they naturally have a dipole-dipole interaction. A non-exhaustive list includes studies of quantum magnetism [22, 23],

supersolidity [24–27], dipolar crystals [28], extensions to the Hubbard model [29], and much more [30]. In addition, combining the properties of the rotational states alongside the nuclear hyperfine spin states, molecules are a promising candidate for use in quantum information science. Superpositions of nuclear hyperfine spin states have already been shown to boast long coherence times [31, 32], a useful feature for the storage of quantum information.

Tangential to all of these applications is the fact that molecules play host to chemistry [33–36]. In working at ultracold temperatures, the last decade has seen the first experiments where molecular chemistry has been studied while the quantum state of the products and reactants are exactly known, rather than relying on some thermal kinematics to describe the relative state populations. Some of the most exciting studies in this regard have come from the group of Kang-Kuen Ni who, to date, has some of the most rigorous results understanding chemical reactions in potassium-rubidium [37]. Other molecule groups around the world are also finding interesting chemistry results, primarily in trying to understand how chemical reactions proceed and how they can be enhanced or inhibited [35, 38, 39].

1.2 Outline

The general motivation of my project has been to "expand the toolbox for ultracold molecules." For as much incredible work and progress that has been made to date, ultracold molecules are still a fairly nascent technology. In particular, for reasons described throughout this thesis, most molecules are particularly hard to nondestructively measure. Furthermore, it is generally hard to have any molecular imaging at all with high fidelity. However, the bulk of the actual work of my time in the lab has been toward building an apparatus that can create ultracold molecules. This thesis will be split into three primary sections. The first will be to describe the built apparatus as it exists today that creates ultracold gases of both sodium and rubidium. The second will detail a publication written with theoretical collaborators at Temple University and Virginia Tech that details a technique we developed to nondestructively measure molecules in excited rotational states. The last chapter will detail the remaining steps our apparatus needs to create ground state ^{23}Na^{87}Rb and the progress that has been done to date toward the realization of this goal.

- Chapter 2: The Experiment

  This chapter discuses our experimental effort at an apparatus designed to produce $^{23}Na^{87}Rb$ molecules. It is broken into sections pertaining to the choice of atomic species and their properties, followed by a detailed discussion of the vacuum chamber, laser systems, and control knobs. There is then a discussion on the creation and detection of ultracold atomic gases.

- Chapter 3: Nondestructive Imaging of Rotationally Excited Molecules

  This chapter includes the text of Ref. [40] with readability adjustments and comments. This paper details a theoretical analysis of an imaging scheme that enables the nondestructive measurement of molecules in excited rotational states. We discuss how rotationally excited molecules are naturally birefringent, and how their birefringence can cause a significant polarization rotation of light that is many linewidths detuned from a direct resonant transition.

- Chapter 4: Future Tasks and Outlook

  This chapter will describe two major experimental steps that are upcoming to the production of $^{23}Na^{87}Rb$ molecules, Feshbach Association and Stimulated Raman Adiabatic Passage (STIRAP). In this chapter I will detail the work that has been done and the equipment that is already in place to realize these two procedures. I will conclude with a discussion on how we will achieve implementation of our nondestructive imaging technique from Chapter 3.

Chapter 2

The Experiment

In my time here at Illinois I've taken two empty optical tables and turned them into the foundation of an ultracold molecule experiment. This has been an extraordinarily educational and rewarding endeavor while simultaneously being incredibly challenging, and sometimes frustrating. No experiment is "easy," per se, but atomic mixture experiments can be particularly challenging. An apparatus with two species of atoms, I've learned, is more than twice as complicated as an experiment with one. As such, the apparatus that has been built is correspondingly complex too.

The purpose of this chapter is twofold: catalog the experiment as it exists today and leave no stone unturned in the description of its components and operation. The second purpose is to provide practically useful explanations for some of the core concepts on which an experiment like this runs. We will begin by discussing the main characters of a ^{23}Na^{87}Rb molecule making machine, namely ^{23}Na and ^{87}Rb atoms.

2.1 The Atoms

2.1.1 Rubidium

If ever there was a perfect atom for laser cooling and trapping, it would be rubidium. Almost everything about it lends itself naturally to laser cooling. A non-exhaustive list of nice properties it has are:

1. a hyperfine splitting that is large in comparison to its excited state linewidth, thus allowing for precise addressing of specific hyperfine sublevels

2. a low melting point that gives it a relatively high vapor pressure at room temperature

3. a cycling transition with a natural wavelength of $\approx 780\,\mathrm{nm}$ (this wavelength is readily available using semiconducting laser diodes which can be made cheaply due to a coincidental industrial development of 785 nm diodes for use in CD players)

4. a natural scattering length of $\approx 95\,a_0$ at zero magnetic field, a property that lends itself well to evaporative cooling

A large motivation for the choice of atomic species in this experiment is related to the fact that rubidium is a naturally "easier" atom to work with than most others. Because ^{87}Rb is such a well behaved atom, there is a very large body of work, both past and present, that host rubidium as the star of the show. Rubidium is a boson, and therefore Bose condenses at sufficiently high phase space densities. The "niceness" of some of the properties listed above will become more obvious as this chapter progresses.

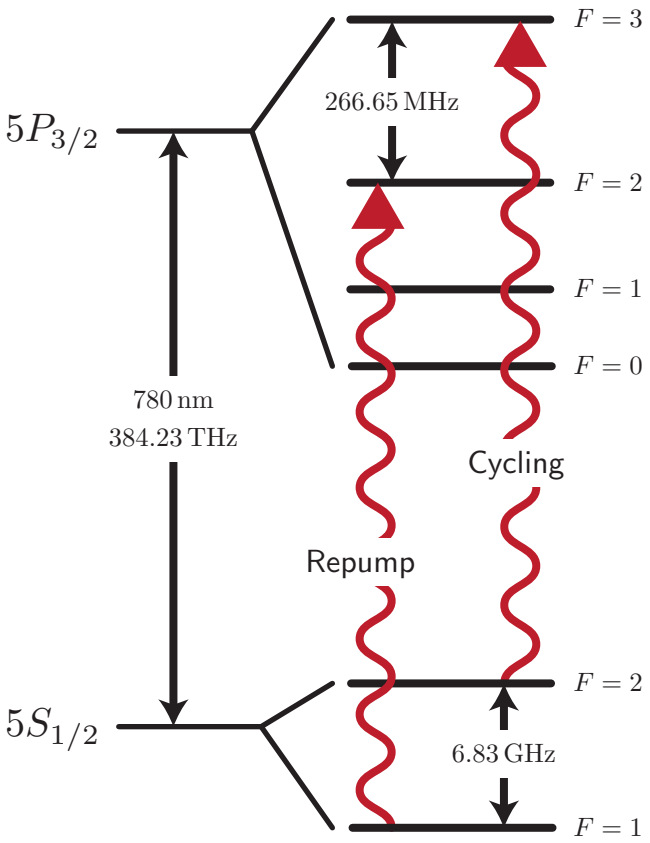

Figure 2.1: A simplified picture of the ^{87}Rb D2 hyperfine structure. Shown are the two laser frequencies used for laser cooling.

Rubidium's energy level diagram is adapted from Ref. [41] in Figure 2.1. The two laser

frequencies that are most necessary for bringing rubidium to ultracold temperatures are labeled as the "cycling" and "repump," the origin of these terms is described in Section 2.3.1.

2.1.2 Sodium

Sodium was the very first atom laser cooled into a magneto-optical trap in 1987 [42]. This incredible achievement was correspondingly celebrated with the awarding of the 1997 Nobel Prize in Physics. Sodium, also a boson, shares many similar favorable aspects to being laser cooled that rubidium does, however it also has a few significant drawbacks.
Among the favorable properties:

1. sodium has an excited state linewidth of 9 MHz compared to the $F' = 2$ to $F' = 3$ hyperfine splitting of 58 MHz.

2. a positive scattering length ($58\,a_0$ and $85\,a_0$ for $|F, m_F\rangle = |1, -1\rangle$, and $|2, 2\rangle$ combinations, respectively) at zero magnetic field that lends itself to well to evaporative cooling

Sodium's primary drawbacks are twofold:

1. it has five orders of magnitude lower vapor pressure than rubidium at room temperature, therefore requiring some kind of heating or oven to provide enough sodium gas to trap

2. sodium's transition wavelength of 589 nm lies directly in the so-called laser diode "dead zone." This wavelength must either be supplied via more complicated and finicky dye lasers, or requires an 1178 nm diode laser and second harmonic generation. Development of laser technology has made 1178 nm diodes readily available and reliable, so this is not really a drawback, only a modest complication to the laser system.

Sodium's energy level diagram is adapted from Ref. [43] below in Figure 2.2.

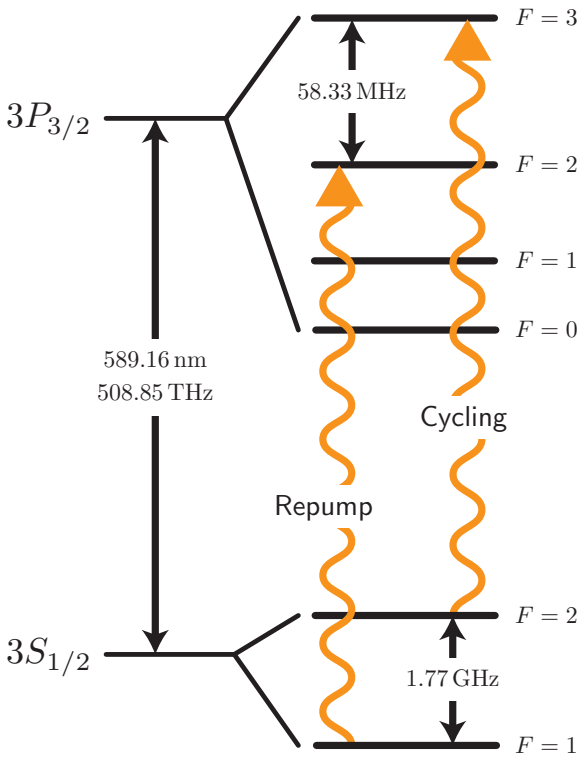

Figure 2.2: A simplified picture of the ^{23}Na D2 hyperfine structure. Shown are the two laser frequencies used for laser cooling.

2.1.3 Sodium-Rubidium

Not only are sodium and rubidium fairly well behaved atoms in their own right, but mixtures of sodium and rubidium have favorable properties as well. As both atoms have the same nuclear spin, their hyperfine quantum numbers are identical. For mixtures of sodium and rubidium in their $|1,1\rangle$ state, their background scattering length is $76.3\,a_0$ [44]. Additionally, they possess a reasonably accessible ($B = 347.6\,\mathrm{G}$) and broad ($\Delta = 4.26\,\mathrm{G}$) Feshbach resonance in their $|1,1\rangle$ pair, which is the mechanism by which loosely bound sodium-rubidium molecules are made.

Sodium-rubidium (^{23}Na^{87}Rb), much like its constituents, is also a very nicely behaved molecule. ^{23}Na^{87}Rb is endothermic, meaning that chemical reactions between them are energetically unfavorable and should be suppressed. As well, thanks to the sizable mass imbalance of the constituent atoms, ^{23}Na^{87}Rb has one of the larger permanent electric dipole moments of the bi-alkali molecule family at 3.3 D [45]. Two groups as of the writing of

this thesis are actively working with sodium-rubidium: the first is Dajun Wang's group at the Chinese University of Hong Kong [46] and second is the group of Waseem Bakr at Princeton [47].

Thankfully, the pathway to the creation of ground state $^{23}Na^{87}Rb$ has been rigorously documented by Dajun Wang's group. Many of the aspects of their experiment are replicated in some degree in ours. This includes our single-cell vacuum design, the implementation of light induced atomic desorption (discussed in Section 2.2.6), and implementation of a hybrid magnetic and optical dipole trapping scheme for evaporative cooling. In the next section of this chapter, I will detail explicitly the construction and operation of our apparatus.

2.2 The Apparatus

2.2.1 The Vacuum Chamber

Nearly all atomic physics experiments are built around a vacuum chamber. It is only in ultrahigh vacuum where extraordinarily cold substances can exist without immediately being destroyed by collisions with room temperature gas. Our vacuum chamber was constructed and prepared using a fairly standard method in the field, which I will detail below.

The Cell and Dispensers

At the heart of our vacuum system is a rectangular glass cell fabricated by Precision Glassblowing Inc. that measures $4 \times 4 \times 10\,\text{cm}$. The walls of this glass cell are not treated with any anti-reflection coating due to the wide range of wavelengths that are necessary for our experiment.

Appended to this cell are two cylindrical tubes that contain alkali metal dispensers for sodium and rubidium that were manufactured by SAES Group. The sodium dispensers are above, the rubidium dispensers are below as viewed in Figure 2.3. These dispensers are the source of the atomic gas that we cool and trap. Essentially, these devices are filaments that contain an alkali-metal salt. A current is run through them and an electrochemical process releases the bare alkali metal that is desired into the vacuum chamber. Observing

each dispenser arm in person, you will see four wires that breach through the glass for us to connect electrical leads. Three of the wires correspond to the positive lead of three separate dispensers, and the fourth wire (in the center of the arrangement) is the common negative lead. As of the writing of this thesis, only one dispenser for each atom has been used, and there is no indication that they will run out of atoms to dispense any time soon. Lastly, the current that is run through the sodium dispenser (4.25 A) is higher than that of the rubidium dispenser (3.0 A) due to some electrochemical differences in their operation. For further reading or reference, or in the event that a new one must be used, I would point the reader to this resource. One additional note on the dispenser wires is that they are the most sensitive part of the vacuum chamber. Care should be taken when modifying or changing dispenser arms so as not to move them significantly. Movement of the wires, particularly near the air/glass interface, has the potential to open small leaks. This can be combated with the use of vacuum sealing resin called Vacseal, though it is best to avoid the problem entirely.

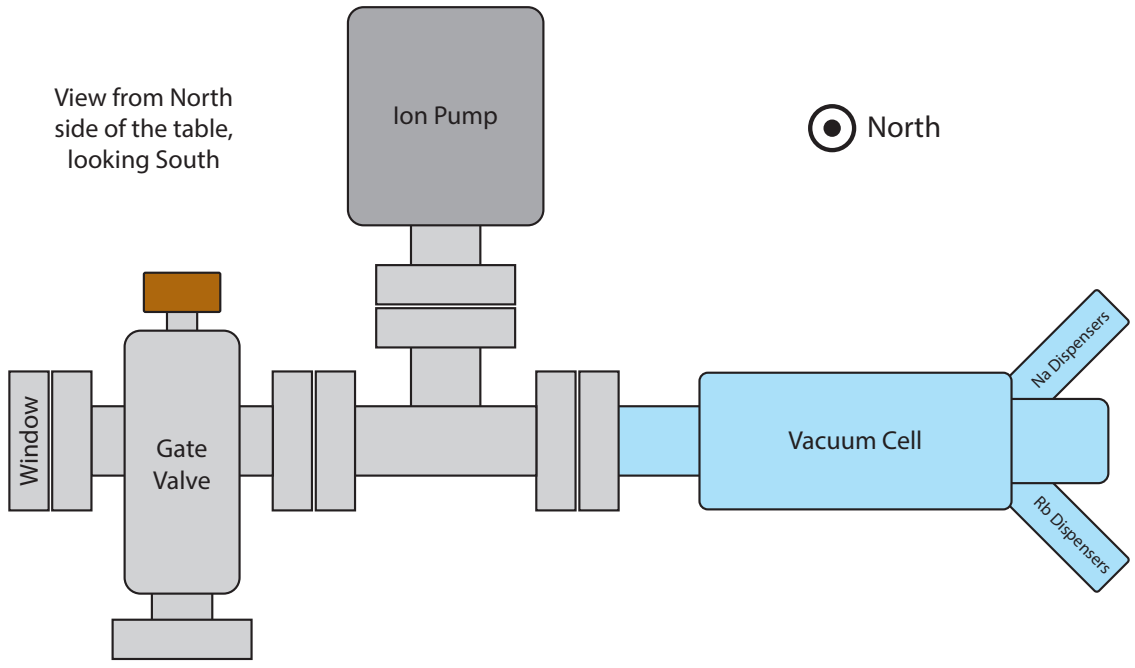

Figure 2.3: View of the bare vacuum chamber as viewed from the north side of the table.

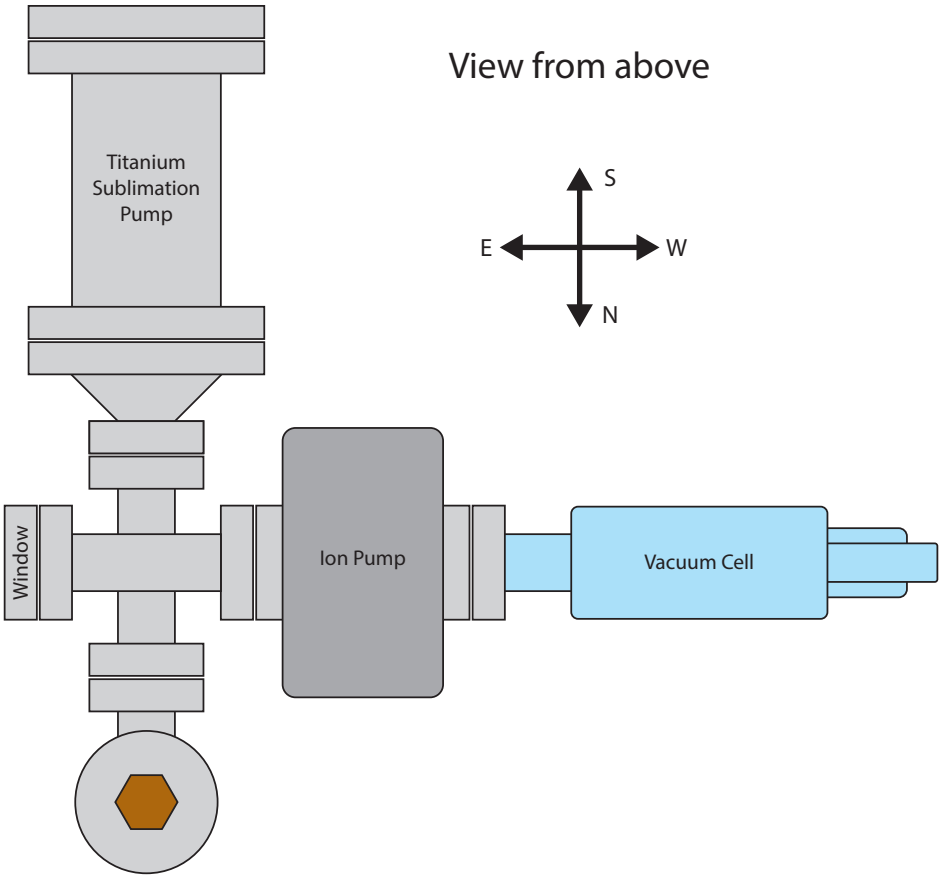

Figure 2.4: View of the bare vacuum chamber as viewed from above.

Vacuum Assembly and Bake

The entire vacuum system was assembled and "baked" back in 2017. A fairly typical approach to the assembly and baking was used in its construction. The list of parts is as follows:

1. The main glass cell and dispensers
2. A Gamma Vacuum 75 l/s TiTan Ion Pump
3. Gamma Vacuum Titanium Sublimation Pump Filaments
4. One stainless steel four-way cross and one stainless steel tee from Duniway Stockroom
5. One angle valve
6. One standard glass vacuum viewport

7. The requisite number of copper gaskets and silvered screws to connect every component

Each of these items (with the exception of the glass cell) was thoroughly cleaned in a sonicator bath using the "AIM" (Acetone, Isopropanol, Methanol) technique. Every part was first submerged in acetone and sonicated for a few hours. Afterward the parts were rinsed with distilled water and placed back in the sonicator that was filled with isopropanol. After that sonication stage, one more rinse and repeat occurred with methanol. The reason for this particular ordering is that acetone, while being a strong cleaning alcohol, leaves the most amount of residue. Methanol, the weakest cleaner, leaves the least amount of residue. Organic matter such as saliva or skin oils are highly antithetical to ultrahigh vacuum conditions, and therefore throughout this process the user must be wearing gloves and taking every precaution to keep the cleaned parts free of dust and grit.

The process of assembling a vacuum chamber is rather straightforward. The connectors between each vacuum component are known as conflat flanges. Two flanges are brought together and held via the tension of a screw and nut. In between any two flanges is a copper gasket. In the assembly process, the copper gasket gets a unique metal seal via the "knife-edge" that is cut into it by the two parts that are being brought together. It is important to note that if a connection must be undone a completely new copper gasket must be used. This is because the knife-edge, and thus the seal, is uniquely made every time two components are brought together.

After full assembly, the chamber was then prepared for "the bake." A roughing and turbomolecular (turbo) pump were connected to the chamber via the angle valve. The roughing pump is responsible for removing the bulk of the air within the chamber, and brings the pressure from atmosphere to $\approx 10^{-3}$ torr. Further reduction of pressure is attained with a turbo pump. This unit consists of a stacked arrangement of titanium fan blades that spin at tens of thousands of revolutions per minute. The turbo pump fans are designed in such a way as to kick particles out from the chamber while not permitting them to re-enter. At such low pressures, gases can be thought of as independent ballistic particles, and as such, a contaminant in the chamber will perform a random walk until it reaches the turbo pump and is essentially "kicked" out. The turbo pump is responsible for the next largest

removal of gas from the chamber, spanning five orders of magnitude to bring pressures to $\approx 10^{-8}$ torr. While the vacuum pumps work, the entirety of the chamber was wrapped in fiberglass heating tape and then wrapped in many layers of aluminum foil. Essentially, we created a literal oven in which we baked our vacuum chamber.

Baking is a process that accelerates the removal of various substances (primarily water) that are absorbed into walls of the various vacuum components. This is done by bringing the entire chamber to high temperatures while the roughing and turbopump operate. Since vapor pressure increases as a function of temperature, the hotter, the better. However, certain practical limitations must be observed. The primary limitation stems from the ion pump (more on that operation later). If the ion pump's magnets are included in the bake, such that the ion pump can be turned on as a diagnostic tool, the magnets must not exceed the temperature that would demagnetize them (the Curie temperature). Additionally, other components such as the angle valve, vacuum viewport, and dispenser feedthroughs all have temperature limitations to consider as well. Consequently we brought our chamber up to 220 °C and we maintained this temperature for two weeks. We monitored the temperature of the chamber via the use of thermocouple devices placed at various spots on the vacuum apparatus. Care was taken in raising the temperature of the fiberglass heating strips so as to ensure no part of the chamber got significantly hotter than another part. Monitoring of the temperature happened on a several hour basis to ensure continued uniformity of the temperature throughout the baking process. "Cold spots" can ruin the integrity of the bake by providing a place for gas to collect that is not at the turbo pump. Additional caution was used in regard to the glass cell, as significant temperature gradients can cause the glass to crack or shatter. When the bake was finished, the entire chamber was brought back to room temperature, the angle valve was closed, and the ion pump was initialized.

The ion pump brings pressures down to their lowest values, and it is solely responsible for continued vacuum maintenance. Its operation is rather simple. A high voltage (kV) is maintained across a parallel plate capacitor, generating a large electric field. Stray gas that gets into the ion pump is immediately ionized in this field. The plate capacitor is surrounded by the aforementioned permanent magnet. As we know from first semester electrostatics, charged particles in a magnetic field undergo circular orbits. The ion pump

works by "removing" particles from the chamber insofar as they are not able to escape the region of the ion pump. When the ion collides with the plate capacitor it will remain there indefinitely. The ion pump is capable of maintaining pressures at or below 10^{-10} torr. For reference, the insides of vacuum chambers in these kinds of experiments have pressures comparable to or lower than deep intergalactic space.

After achieving the ultra-high vacuum condition, we are ready to purposefully introduce the vacuum contaminants of ^{23}Na and ^{87}Rb via the use of the alkali metal dispensers. When the dispensers are on, the chamber can be considered to have very dilute and low pressure gases of our atomic species that we will then laser cool and trap.

2.2.2 The Laser Systems

To nobody's surprise, in order to laser cool and trap atoms, it is necessary to have lasers. In the next sections I will detail the laser systems we have for cooling sodium and rubidium.

Rb Laser System

Our rubidium laser system consists of two External Cavity Diode Lasers (ECDLs). The first is a DL100 from Toptica with a center wavelength of 780 nm. It is frequency referenced to rubidium's cycling transition using polarization spectroscopy, as described in Section 2.2.3. The second laser is a MOGLabs CEL002 that addresses the rubidium repumper, and it is frequency referenced using beatnote locking to the cycling laser (I turn the reader to the thesis of Eric J. Meier, Appendix A.2, for a detailed description of this procedure). A diagram of the "preparation" side is shown in Figures 2.5 and 2.6.

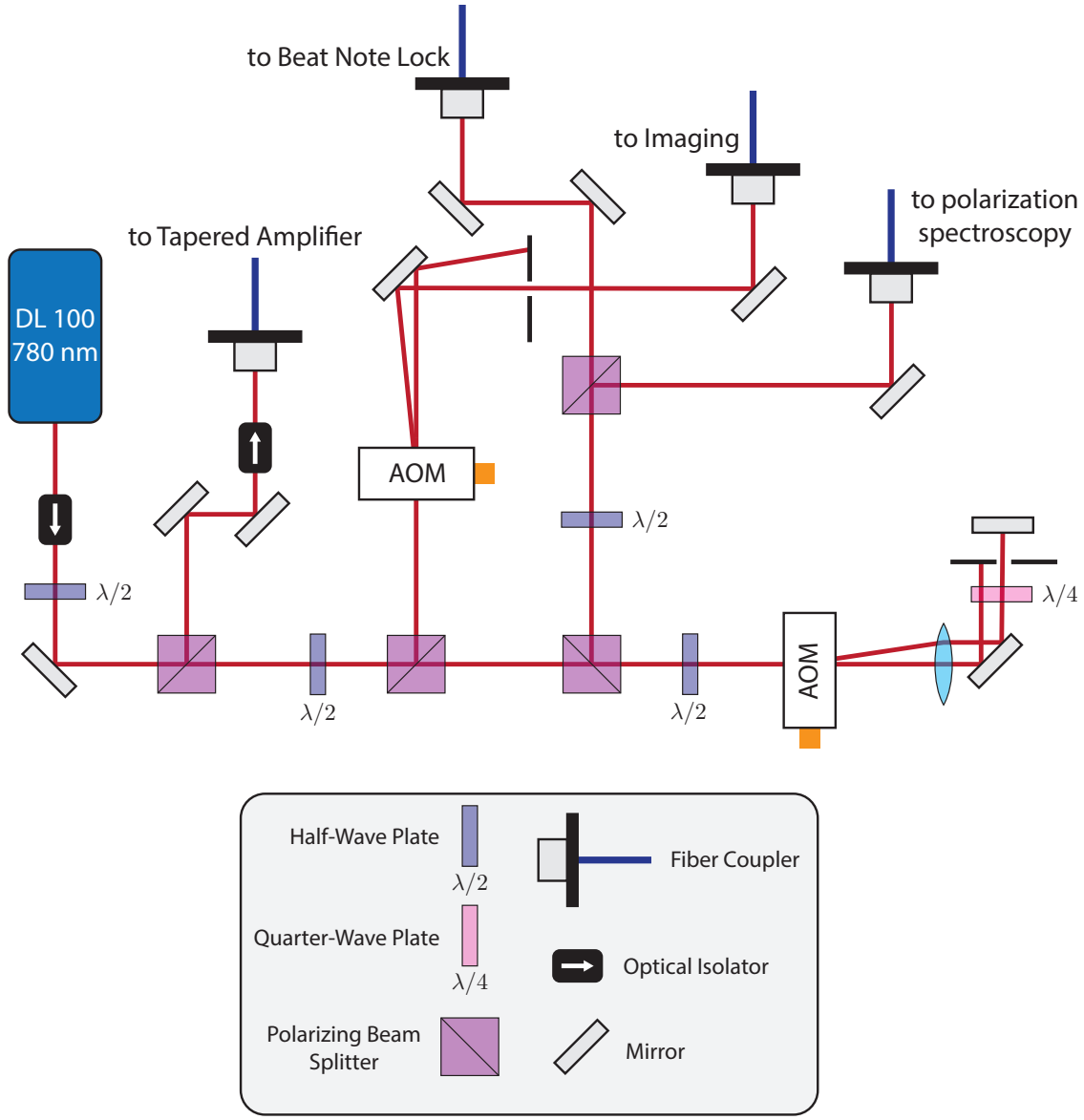

Figure 2.5: Rubidium cycling laser path configuration. A majority of the light from the laser is sent to the tapered amplifier that will provide the trapping light at the vacuum chamber. The remaining is split between polarization spectroscopy, beat note locking, and absorption imaging. An AOM is an acousto-optic modulator.

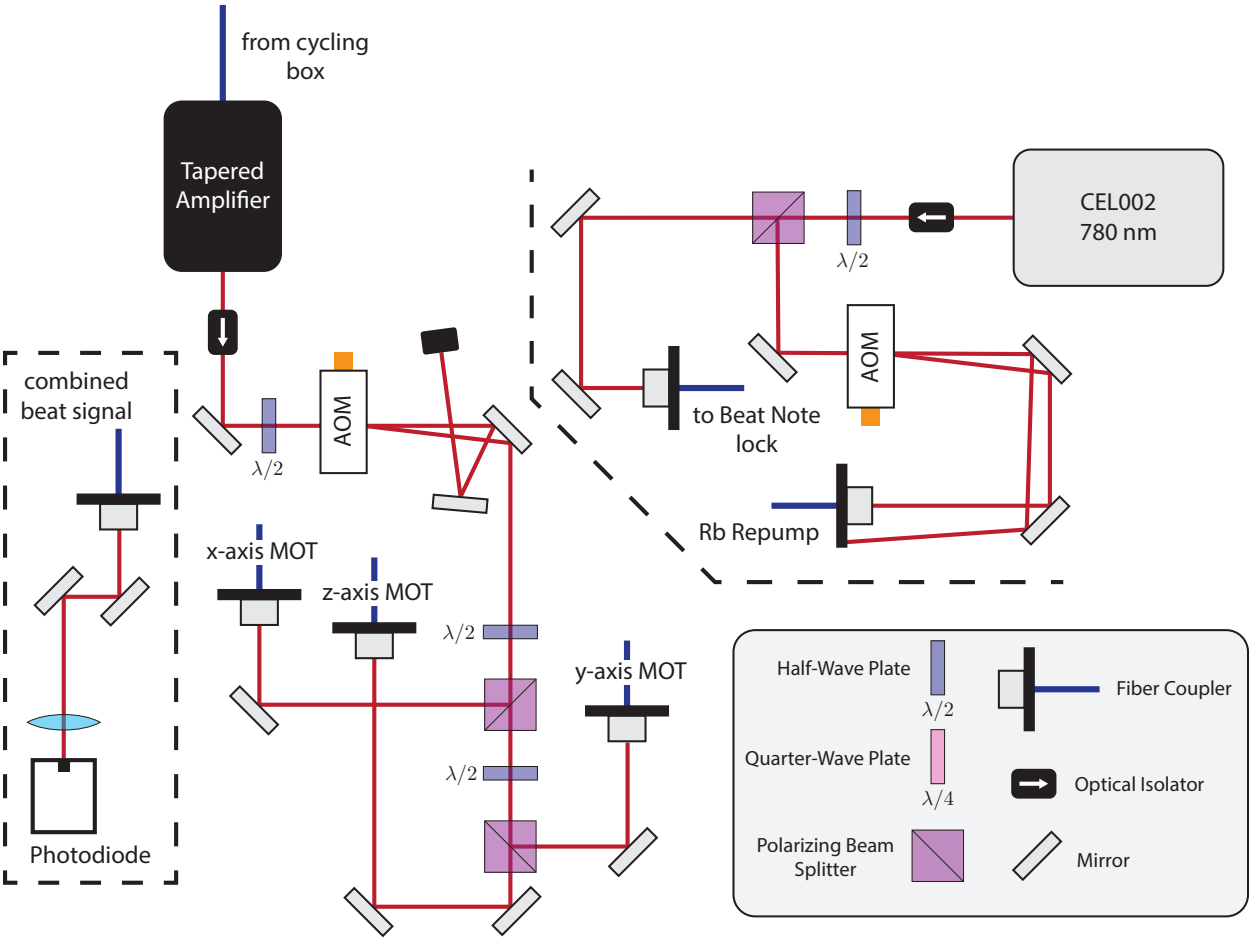

Figure 2.6: Remainder of the rubidium laser system preparation side. Shown is the tapered amplifier that outputs the requisite amount of power to trap rubidium at the chamber. As well, the beat note locking photodiode and repumper laser setup are shown. This is the view from the west side of the optical table.

In Figure 2.5 the acousto-optic modulator (AOM) in the "imaging" path has a frequency set to +100 MHz. The AOM at the bottom right in the "double-pass" (see Section 2.2.6) configuration has a dynamic frequency throughout the experiment, however is nominally set to +50 MHz. In Figure 2.6 the AOM after the tapered amplifier is set to +85 MHz, and the AOM on the repumper laser is set to -110 MHz.

Na Laser System

The sodium laser system consists of a single Toptica DL Pro laser with a center wavelength of 1178 nm. The light is amplified with the use of an MPB Communications Raman Fiber Amplifier (RFA, part number VRFA-P-1500-589-SF). The output of the RFA is sent via a

fiber into a second harmonic generator that frequency doubles the amplified seed light to the desired 589 nm wavelength necessary for cooling sodium. The entire system is capable of reliably outputting 1 W of power. The laser frequency is stabilized to a modulation transfer spectroscopy setup detailed in Section 2.2.3. A diagram of the laser preparation side is shown below in Figure 2.7.

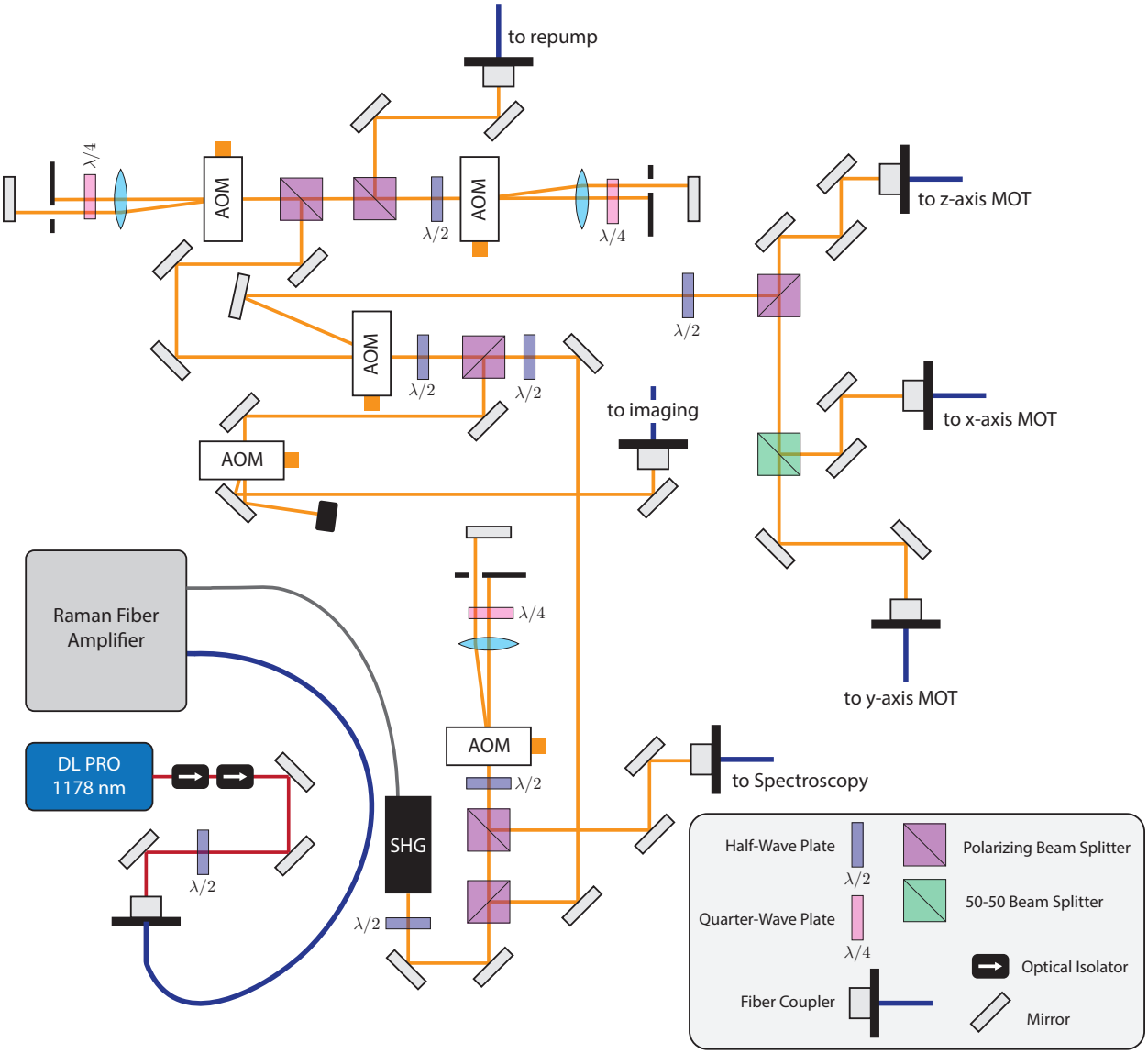

Figure 2.7: Diagram of the sodium laser preparation system prior to light delivery at the vacuum chamber.

The first AOM encountered after the SHG is in a double-pass configuration that goes to modulation transfer spectroscopy. Its frequency is dynamic in the experiment but is nominally set to +50 MHz. The "imaging" path AOM is set to +100 MHz, and the AOM

that diffracts to the MOT paths is set at +83 MHz. The remaining two AOMs, both in the double pass configuration that go into the repumper fiber, are set at a fixed frequency of +450 MHz.

The Chamber Paths

The previous two sections show the laser beam preparation prior to arriving at the vacuum chamber. Figure 2.8 shows the end result of this preparation. From left to right in the figure is the following:

1. A raised optical breadboard on the east side of the vacuum chamber hosts the beam paths for sodium and rubidium absorption imaging, as well as the output of a 1064 nm optical dipole trap and corresponding power stabilization photodiode (see: Section. 2.2.6)

2. A breadboard on the south side of the apparatus (above the cell) contains the outputs for the sodium and rubidium repumping light. They are combined on a dichroic mirror and sent into the cell. The z-axis MOT paths for both species combine on another dichroic (not shown) above the plane of the picture and sent directly down through the intersection of all the beams within the vacuum chamber. Additionally, the x- and y-axis MOT paths for both species are retro-reflected and pass through a bichromatic quarter-wave plate from Meadowlark Optics (these quarter-wave plates were specifically manufactured to work simultaneously for 589 and 780 nm light). Lastly, lenses, mirrors, and a half-wave plate designed to re-collimate, rotate the polarization of, and re-focus the 1070 nm optical dipole trap are shown.

3. A breadboard on the north side of the apparatus (below the cell) contains the source of the x-axis paths for the sodium and rubidium MOTs and the y-axis source for the rubidium MOT. The sodium and rubidium MOT beams are combined onto a dichroic mirror and are sent through a bichromatic quarter-wave plate. Additionally, the sodium and rubidium optical pumping beams combine on a dichroic mirror and are directed into the chamber. Lastly, the 1070 nm ODT is steered and focused into the cell with the use of mirrors and a lens.

4. An optical breadboard on the west side of the experiment contains the output for the sodium y-axis MOT path. So too, this path contains the imaging lens and camera for measurement of the atoms. Lastly, the source of the 1070 nm optical dipole trap is shown, with the corresponding AOM and photodiode used for active power stabilization.

Not shown for the sake of clarity are the "clean-up" polarizing beam splitters used at the outputs of these optical fibers that translate polarization fluctuations into power fluctuations. So too, the z-axis MOT beam paths are omitted for the sake of clarity as they exist in a plane above the figure and would obscure the shown beam paths. All solid-black squares are beam blocks.

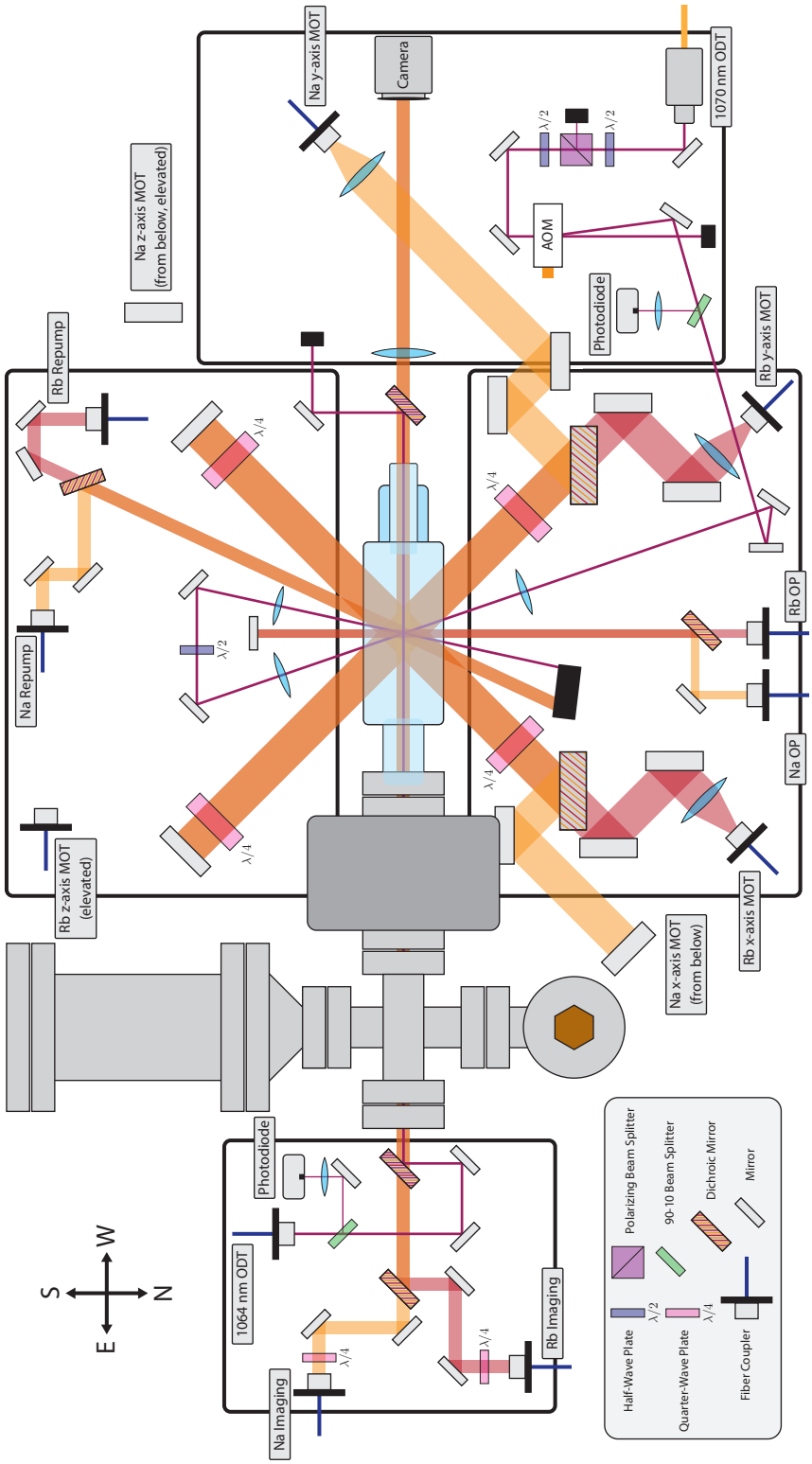

Figure 2.8: Top-down view of the laser beam paths from the north side of the apparatus (magnetic field coils not shown). Also not shown are the z-axis paths as they are elevated above the plane of the picture and would obscure what is shown.

2.2.3 Spectroscopy

Lasers have frequency stability granted by their build quality and "locking" electronics. However, this stability only corresponds to the precision of the laser frequency, and there is no guarantee that the *absolute* frequency of the laser is correct for a particular application. In order to provide the absolute reference a common technique is to use some kind of spectroscopy on the atom that is being laser cooled. The two methods employed in our experiment are detailed below; polarization spectroscopy on rubidium, and modulation transfer spectroscopy on sodium.

Rb Polarization Spectroscopy

The rubidium polarization spectroscopy setup is shown in Figure 2.9. A beam has its polarization "cleaned" via a polarizing beam splitter (PBS). (Cleaning the polarization refers to the condition where *if* a polarization drift or rotation occurs in the optical fiber delivering the light, to the spectroscopy this will present as a total power difference, rather than propagate the wrong polarization through the entire setup.) It then passes through a half-wave plate (HWP) and another PBS to split the beam into two paths, a lower power "probe" beam and a higher power "pump" beam. The probe beam with horizontal polarization passes through a rubidium vapor cell (glass tube with rubidium gas in it). It then encounters a half-wave plate set to 22.5 ° to make it diagonally polarized. Lastly, the probe beam encounters another PBS and the light splits into two paths and sent to a balanced photodiode. The output signal of this photodiode is the *subtraction* of the two powers. The pump beam, on the other hand, passes through a quarter-wave plate (QWP) set at 45 ° to give it circular polarization. The beam is then directed to counterpropagate through the rubidium vapor cell, overlapping the probe beam.

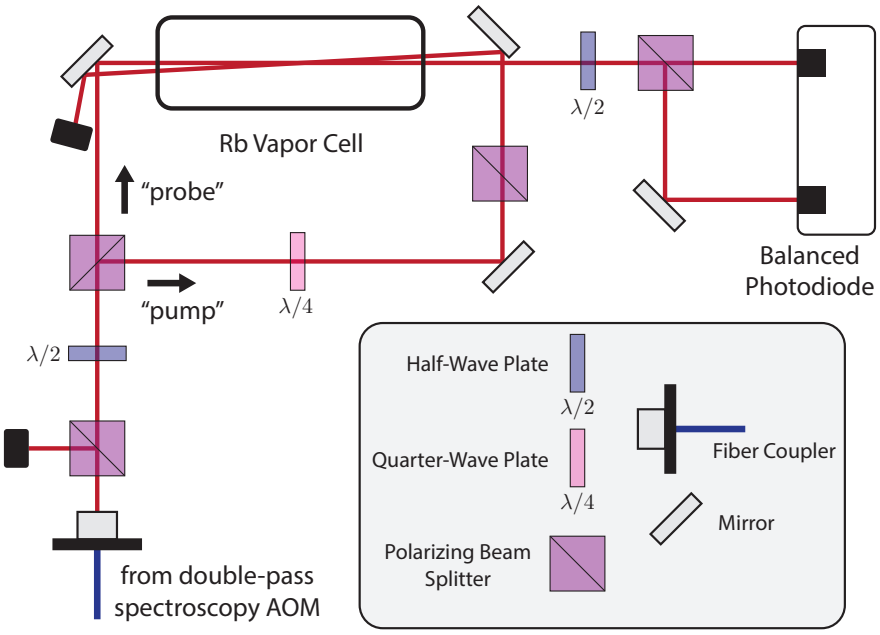

Figure 2.9: The laser beam paths for polarization spectroscopy of rubidium.

To understand how polarization spectroscopy works, it is instructive to think of two distinct cases. First, the case where the laser is not resonant with the atomic medium, and hence the light has no strong interaction with the atoms in the cell. The probe and pump beams pass through the vapor cell normally, not affected by either the gas or the other beam. The probe beam, therefore, encounters the last PBS, has its diagonal polarization split evenly into vertical and horizontal polarizations, and the photodiode will read no power difference between the two polarization components and output a signal of zero.

Now, we can consider the case where the laser is resonant with one of the atomic transitions. Here, the light and atoms have a strong interaction. The atoms will absorb light from the probe beam and scatter it out in all directions. Consider now the probe beam's polarization. It is nominally set to be horizontal based on the diagram in Figure 2.9. Horizontally polarized light may also be considered an equal linear combination of left and right-circularly polarized light. As the probe beam passes through the atomic medium, both left and right circular polarizations are capable of driving transitions. In the absence of the pump beam, the amount of power taken from each circular component of the polarization by the atoms is equal. Therefore the light is still horizontally polarized by the time it reaches the last HWP/PBS, and the power difference measured by the photodiode will be zero. *With* the

pump beam, however, the situation changes. The pump beam has solely one circular polarization as given by the quarter-wave plate. Compared to the probe beam, the pump beam with more power drives either the left or right-circular transitions at a higher rate. The effect on the probe beam is then that one of its circular polarization components is driving transitions at the normal rate while the other component does less. After passing through the cell, there is now an imbalance of left and right circular polarizations, and hence the probe beam's total polarization has rotated. Now, the HWP/PBS no longer equally split the power and the photodiode outputs a nonzero voltage.

This is the punchline of polarization spectroscopy. Near the atomic resonance the probe beam gets an effective polarization rotation as the pump beam polarizes the atomic medium, inducing a birefringence. This rotation can be measured, and the signal can be fed to the laser. Our ^{87}Rb polarization spectroscopy signal on the cycling transition is shown in Figure 2.10. Pictured is the signal from the photodiode as the laser frequency is scanned across resonance.

Figure 2.10: Oscilloscope trace of the cycling transition for ^{87}Rb using polarization spectroscopy.

Technical Note: Though polarization spectroscopy works fairly well, our particular setup has some practical considerations for control in the experiment. The first is related to the

fact that the acousto-optic modulator that sends laser power to the spectroscopy setup operates at a frequency near the lower limit of its specifications. Namely, the AOM has a center-frequency of 80 MHz, whereas we nominally drive it at 50 MHz. When we increase the frequency from 50 MHz to a higher value, as would be done in a "compressed MOT" stage or polarization gradient cooling, the diffraction efficiency of the AOM changes dramatically. This changes the laser power that gets to spectroscopy, and therefore modifies the size of the polarization spectroscopy signal. If it could be guaranteed that the signal size increase is symmetric on both sides of the zero crossing, this would not be an issue. However, this is not the case, and since we absolutely need dynamic laser frequency control in the experiment, we must also dynamically change the strength of the AOM radio-frequency (RF) drive to ensure the power getting to spectroscopy remains constant.

Na Modulation Transfer Spectroscopy

The sodium modulation transfer spectroscopy setup is shown in Figure 2.11. The input beam in 2.11(a) has its polarization cleaned via a PBS, then a HWP and PBS then split the power into a less powerful probe and more powerful pump beam. The probe beam passes through the atomic medium and is then directed onto a photodiode. The pump beam passes through another clean-up PBS and then an electo-optic modulator (EOM, QUBIG PM7-VIS). The EOM adds frequency sidebands to the light at ± 10.04 MHz, meaning it effectively turns the pump beam of frequency ω into three beams of frequencies $\omega, \omega \pm 10.04$ MHz. The pump beam is then directed to counterpropagate with the probe beam through the atomic medium. Figure 2.11(b) shows the signal processing side. The photodiode signal is passed through a high pass filter to block the DC voltage that corresponds to the power of the probe beam. In modulation transfer spectroscopy, the photodiode is there to detect the presence of the 10.04 MHz signal on the *probe* beam (more on this below). The signal passes through an amplifier and into an RF mixer. The second input of the mixer takes a 10.04 MHz local oscillator reference frequency from an arbitrary waveform generator that also drives the EOM. The output of the mixer is the sum and difference frequencies of the photodiode signal and the local oscillator. This resultant signal is then passed through a

low pass filter that will be used to lock the sodium laser.

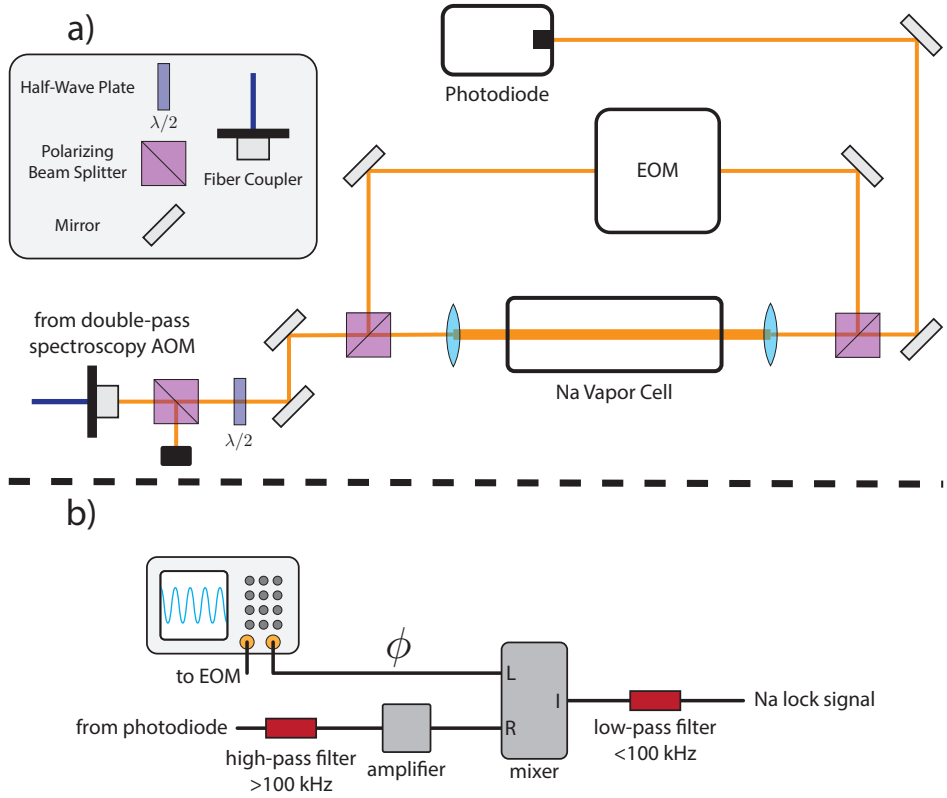

Figure 2.11: a) The laser beam path for modulation transfer spectroscopy of sodium. b) The electronic signal processing path for modulation transfer spectroscopy of sodium.

To understand what occurs in modulation transfer spectroscopy we will again consider what occurs both in the resonant and off-resonant case. The off-resonant case is the most simple. The light has no strong interaction with the atomic medium, and the probe and pump beams pass through the atomic medium with no effect. The probe beam hits the photodiode wherein after the low pass filter, there is no signal, and therefore no effect at the mixer, and thus a signal of zero.

In the resonant case, the effect of the atoms now becomes prominent. Atomic media are "non-linear" in that they can support multi-photon mixing processes. Essentially, what occurs is the atoms mediate an effect wherein the pump, sidebands, and probe intermingle, and the sidebands that were initially written onto the pump beam can then transfer to the probe beam. This is often described in the context of four-wave mixing, where one probe and pump photon at frequency ω with another pump photon at $\omega + \delta$ combine and stimulate the

emission of an additional photon at $\omega + \delta$ that propagates out in the direction of the probe beam. When the probe hits the photodiode, then, the 10.04 MHz frequency passes through the high pass filter and into the mixer at some phase, ϕ, relative to the local oscillator. The output of the mixer then becomes nonzero and is thus the source of the locking signal. The strength of the sideband transfer process is maximized on the cycling transition of the atomic medium and when the sideband frequency is comparable to the excited state linewidth (hence the choice of the 10 MHz modulation). I would direct the reader to Ref. [48] for a comprehensive analysis on the resultant signal of modulation transfer spectroscopy.

A nice feature of modulation transfer spectroscopy is that it is naturally background free. Though more complicated to setup initially, the result has been that our sodium laser system's frequency is never under question. A sample oscilloscope trace of sodium's spectroscopy is shown in Figure 2.12. One important side note in the acquisition of this signal: we tried for more than a month to diagnose why our modulation transfer spectroscopy signal would not show up, despite doing everything correctly per all of the resources we referenced. It turned out that due to the vapor pressure considerations from Section 2.1.2, the amount of gaseous ^{23}Na in our cell was too low to get a sizable signal. We had to wrap our cell in heating tape and raise the temperature to $\approx 80\,^{\circ}$C and miraculously our signal appeared.

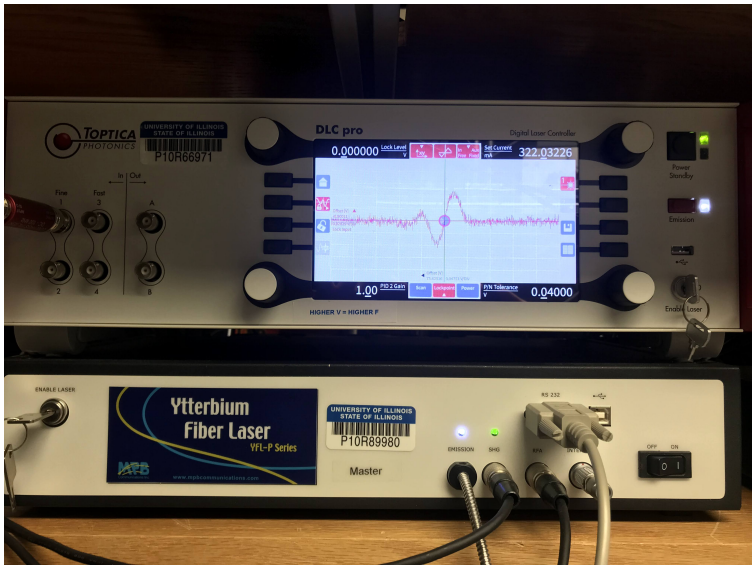

Figure 2.12: Oscilloscope trace of the cycling transition for ^{23}Na using modulation transfer spectroscopy.

2.2.4 Magnetic Field Coils

The "Feshbach" Coils

The primary magnetic field coils in our experiment are the so-called "Feshbach" coils, due to the fact that they will be responsible for generating the 347 G magnetic field necessary for the formation of loosely-bound $^{23}Na^{87}Rb$ molecules. However, these coils serve multiple roles in the experiment, first starting in the magnetic field gradient (anti-Helmholtz) configuration for the magneto-optical trap and quadrupole trap, and will eventually switch in the experimental sequence to the standard magnetic field (Helmholtz) orientation for Feshbach association.

A comprehensive guide was written back in 2018 on the construction of these magnetic field coils. That document is modified and transcribed for readability in Appendix A. In summary, they are two sets of 36 turn 1/8 inch hollow copper refrigerator tubing in a 6×6 array. The innermost radius of the coils is 3.3 cm. These coils were designed to provide a magnetic field of ≈ 380 G at a current of 80 A, well above the known Feshbach resonance necessary for $^{23}Na^{87}Rb$ formation as discussed in Chapter 4. They now additionally act to provide the magnetic field gradient necessary for magnetic trapping of both atomic species, with a 0-80 A range corresponding to 0-150 G/cm.

Shimming, Z-Field, and Imaging Coils

Additional magnetic field control is attained in our experiment via the use of "shim" coils. These coils are designed to produce small bias fields to cancel out systematic and undesired magnetic fields from the many different sources that surround the vacuum cell (i.e. the ion pump, ferrous materials nearby, etc.). In the experiment there are two sets of magnetic field coils in the east/west direction. The first set contains 100 turns of 22 gauge magnet wire in a Helmholtz pair. The second set in the east/west direction are 125 turn and 22 gauge magnet wire, also configured in a Helmholtz pair. The second set is connected to a small FET-based switching circuit that can be turned on and off via our experimental control software. These provide a "quantization axis" for our absorption imaging light that propagates in the same direction. In the north/south direction are two sets of 25 turn coils arranged in a Helmholtz pair. One provides the bias field, the other is connected to a TTL switching

circuit to provide a quantization axis for our optical pumping beam. In the up/down axis of the experiment, a set of 50 turn coils lie in the space between the Feshbach and "600-set" coils that provide a bias field in the up-down direction. The currents sent to the bias coils are quite low. They were optimized by feeding back on the temperature of our atomic clouds after polarization gradient cooling (described in Section 2.3.2). We found that primarily the up/down magnetic field shim had the most significant impact on the atoms' temperature.

The third knob of magnetic field control in the z-axis are from the so-called "600" coils. They are named after the number of loops in each holder. These are designed to provide sizable magnetic fields that can be dynamically controlled from our control software. Their primary use so far has been to work in conjunction with the Feshbach coils to provide the gradient (Feshbach) and field ("600") necessary to do Stern-Gerlach analysis on our atomic clouds. They will likely serve additional uses for Feshbach association and molecule control in the future.

2.2.5 Experiment Control

The mechanism by which the experiment is run is multifaceted, and there are many different kinds of equipment and software used. This section will explain the function of a majority of these components.

Cicero and Signal Control

Our experiment is run via a program called Cicero, written by Aviv Keshet back when he worked in the Ketterle Lab at MIT [49]. The program provides dynamical control of our apparatus by providing a user interface (Cicero) and a communication server (Atticus) that interfaces with a field-programmable gate array (FPGA - Opal Kelly XEM3001) and a National Instruments card/chassis (NI PXIe-1073).

There are two kinds of signals that we have Cicero control: analog and digital. Analog signals are ones where the voltage value matters to the component in the experiment. The prime example of this is the control voltage that gets sent to the voltage controlled oscillators (VCO) that provide the RF source to many of our acousto-optic modulators. The analog

signals are shown in the top part of the Cicero user interface. After the programming from the computer, an NI PXI-6733 card within the PXIe chassis generates and sends the signals to a BNC-based breakout unit (BNC-2110). From the BNC unit the signals then pass through an analog isolator box. The isolator box provides the function of making the BNC transmission line effectively uni-directional. It does so via using an integrated circuit with an LED and photodiode, wherein the LED power mimics the signal it receives from the NI unit, and the photodiode reads it and generates the equivalent voltage on the output. This is important, because if there is some noise or spurious voltage generated by the device receiving the signal, that disturbance does not propagate back through the BNC and into the NI card. A comprehensive guide on the construction of the analog isolator box is in the Gadway Lab Box folder under "Schematics and Tutorials."

Digital signals are treated in much the same way as the analog. After programming the signals are generated in an NI PXIe-6535 digital I/O card that breaks out into an NI SCB-68A, with a corresponding digital isolator box. The digital signals are used when something simply needs to be on or off, such as the diodes for light induced atomic desorption, or an RF switch that drives an AOM.

A sample experimental sequence is shown in Figure 2.13. Cicero's user interface breaks the experiment into blocks called time steps. Each column corresponds to a time step, and each row corresponds to a particular analog (middle, black rows) or digital (bottom, colorful rows) channel. Within each column one can see: the length of the time step, the modification of the analog signals in that timestep, and which digital channels are on or off based on the colors present. In this particular sequence shown in Fig. 2.13, ^{87}Rb atoms are being prepared at sub-Doppler temperatures in their $|F, m_F\rangle = |2, 2\rangle$ state. Time steps 1-3 correspond to loading a magneto-optical trap (Section 2.3.1), 7-11 correspond to sub-Doppler cooling (Section 2.3.2) and optical pumping, and the remaining time steps release the rubidium atoms in free fall and take an absorption image (Section 2.3.3).

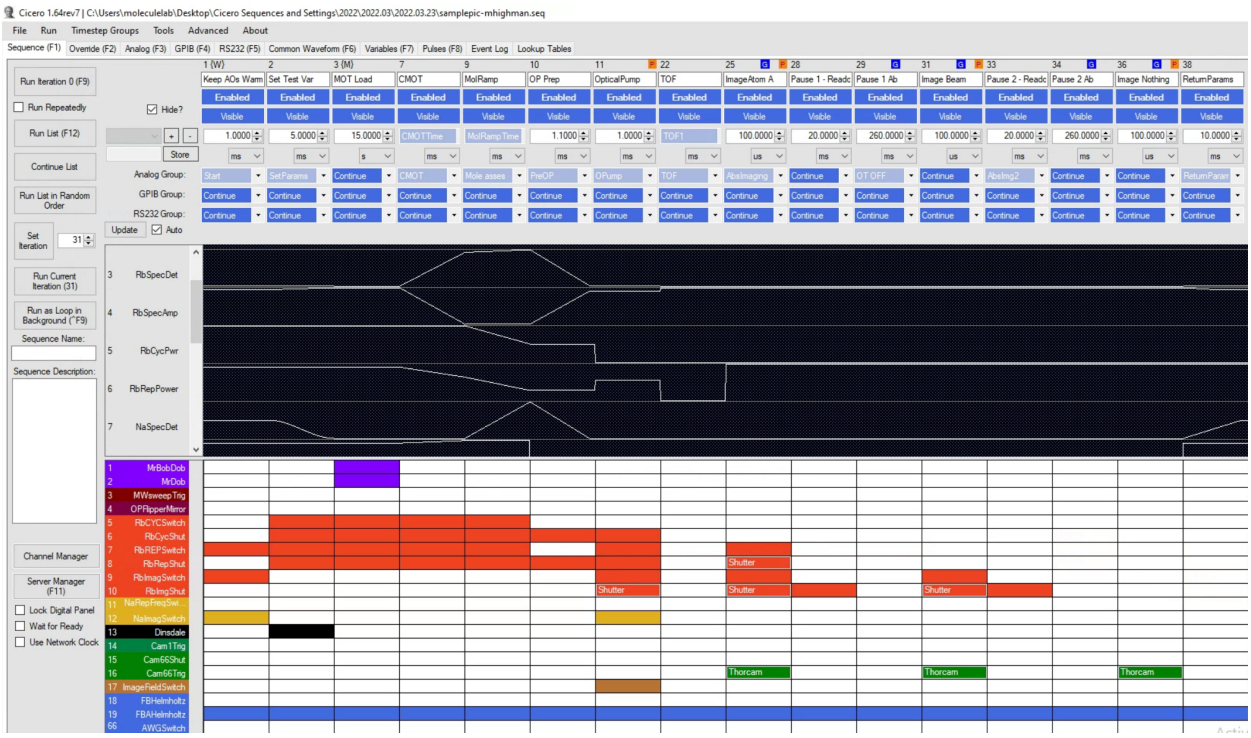

Figure 2.13: A picture of a typical experimental sequence used to prepare Rubidium atoms at sub-Doppler temperatures while optically pumped to the $|F, m_F\rangle = |2, 2\rangle$ state.

2.2.6 Hardware

There are many different hardware components necessary to create a gas of ultracold atoms. I will detail the primary workhorses of our lab here.

Light-Induced Atomic Desorption

Unrelated to laser frequency control is the mechanism by which we artificially increase the vapor pressure of atoms in our vacuum chamber to increase the amount of atoms loaded into our magneto-optical traps. We do so via a process called light-induced atomic desorption, or LIAD for short.

Within the vacuum chamber our atomic rubidium and sodium will, over time, form thin layers on the surfaces of the glass cell. This is an unavoidable process as the atoms are polarizable, and there is a van der Waals attraction between the free atom and the surface of the glass. This weak binding force can be overcome with the application of light. A wide array of wavelengths can be used for this process, however typically the higher frequency, the

better. In our application of LIAD we use two LED diodes from Thorlabs: an uncollimated M395L5 at 395 nm and a collimated M365LP1-C1 at 365 nm. Both LEDs are powered by their own driver, the LEDD1B. These drivers are capable of taking in a TTL signal from Cicero to enable and disable the diodes. When the diodes are on, the atoms that are adsorbed onto the surface of the glass break free and begin their ballistic travel through the vacuum chamber. This effectively increases the vapor pressure of the atoms in the cell, allowing for more free atoms to be caught into the magneto-optical trap. When the LIAD light is turned off, the free atoms within the cell are again permitted to adsorb back onto the glass walls. Figure 2.14 shows how the presence of the LIAD LEDs decreases the loading time and increases the maximum atom number that can be loaded into our sodium MOT. As sodium has a lower vapor pressure than rubidium, LIAD's effect is most pronounced on the sodium atom number. For rubidium, often the load time does not decrease much, and there is only a modest increase in the total atom number.

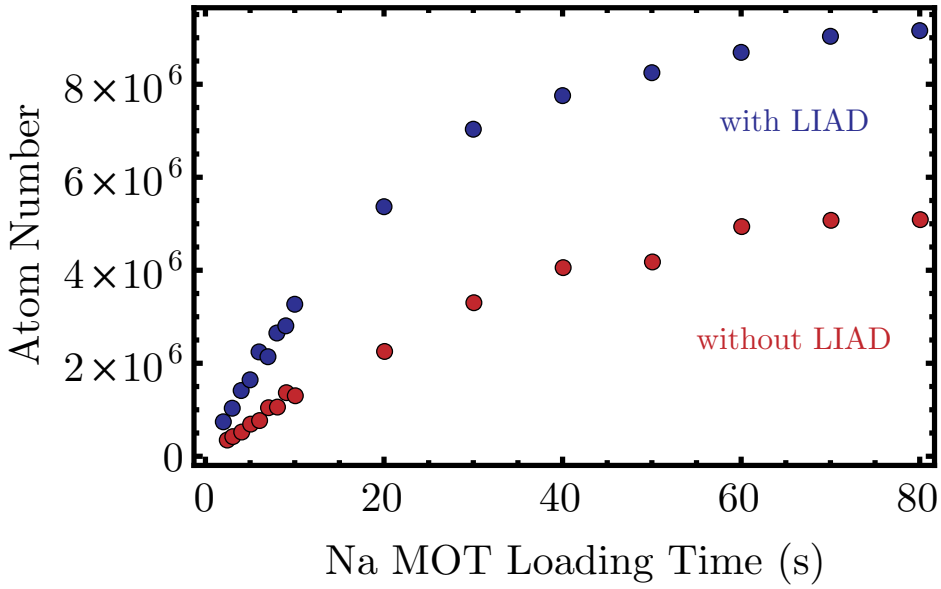

Figure 2.14: The number of atoms in a sodium MOT for a given loading time. In blue, the UV diodes for LIAD are on, while in red they are off. LIAD increases the total number of sodium atoms held in the MOT and decreases the loading time due to its enhancement of sodium's vapor pressure.

Perhaps most importantly, 365 and 395 nm light lie within the ultraviolet (UV) range. When employing these diodes in our experiment we must guarantee that we shield ourselves, the experimenters, from their light. UV light accelerates the formation of cataracts in the

eye and, just as from the sun, is a source of radiation that increases the risk of developing skin cancer. To protect ourselves we have a laser safety curtain that surrounds the entire table that completely encloses the apparatus during normal operation.

Acousto-Optic and Electro-Optic Modulators

Acousto-optic modulators (AOMs) are the primary mechanism by which the frequency of laser light is controlled. Their operation is rather simple to understand. A crystal is attached to a piezo-electric transducer that shakes at a driven RF frequency (say, ω_{RF}). This generates a pressure wave within the crystal, and when the laser light (frequency ω_0) passes through the crystal it diffracts and it leaves with a frequency $\omega_0 + \omega_{\mathrm{RF}}$. One may understand this as an RF drive providing a source of phonons, or vibrational excitations in the crystal. An incoming photon from the beam collides with the phonon, and due to energy and momentum conservation it leaves at an angle with the increased frequency of the phonon. Alternatively, one can consider the regions of higher and lower indicies of refraction in the crystal created by the RF pressure wave as a moving diffraction grating. The light encounters this diffraction pattern and splits into its Doppler-shifted diffraction orders. The amount into each diffracted order depends on the orientation of the crystal relative to the incoming beam. As such, AOMs are typically aligned to maximize the amount of diffraction into the first (or minus first) order, with frequency $\omega_0 \pm \omega_{\mathrm{RF}}$.

Nearly all of the AOMs used in our experiment are manufactured either by Gooch and Housego or IntraAction Corp. Unfortunately, at the writing of this thesis the founder and primary manufacturer at IntraAction has passed away, so his source of inexpensive yet quality AOMs may not be available for future purchase.

In the "single-pass" arrangement, AOMs act not only to shift the frequency by a set amount given by the RF drive frequency, but also to control the amount of power in the beam. The strength of the diffraction into the first order of an AOM is dependent on the power of the RF drive. As such, the electronics used to operate the AOM reflect this capability, as described later.

In the "double-pass" configuration [50], the AOM becomes a tool through which the

frequency of the diffracted beam can be dynamically changed without significantly affecting the beam alignment. Figure 2.15 shows a double-pass setup. Vertically polarized light bounces off a polarizing beam splitter (PBS) and through an AOM. The AOM diffracts most of the light to the first order. A lens is placed one focal length away and collimates the diverging output of the AOM. The undesired diffracted orders are blocked via an iris and the light passes through a quarter-wave plate (QWP) oriented at 45 °, after which the beam hits a mirror to directly reflect it on top of itself. After passing through the QWP and lens again, the light passes into the AOM. Since the incoming light is now at an angle, the desired diffraction order after the second pass will counterpropagate with the incoming beam, yet it will now have a frequency that is shifted by twice the AOM drive. Since the beam passed through the QWP twice, with a reflection in between, it leaves the second pass of the AOM with horizontal polarization that transmits through the PBS. The placement of the lens at the focal length from the AOM means that no matter the frequency of the RF drive, the lens will recollimate the beam and its alignment will not be significantly altered. This is especially useful for sending light to a spectroscopy setup, wherein a modification of the double-pass frequency can change the frequency of the entire laser.

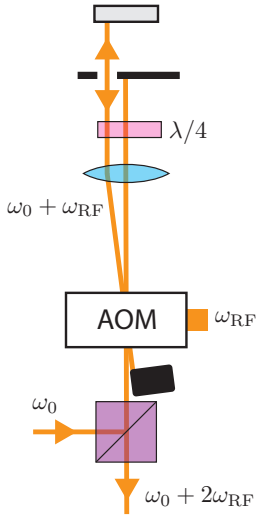

Figure 2.15: A standard double-pass AOM configuration. Light enters from the bottom left with vertical polarization at frequency ω_0. It diffracts in the first pass of the AOM wherein it is collimated by a lens placed one focal length away from the AOM. An iris blocks the other diffracted orders and the light passes through a quarter-wave plate and hits a mirror placed one focal length away from the lens. The light bounces back onto itself, and passes through the QWP, making it horizontally polarized. It diffracts a second time in the AOM and gains twice the RF drive frequency. Lastly, it passes through the PBS for use elsewhere.

On the rubidium side of the apparatus, the AOMs are driven by a collection of parts from Mini-Circuits as shown in Figure 2.16. The signal path is as follows: an RF signal is generated via the use of a voltage controlled oscillator (VCO). The VCO receives a voltage either via a potentiometer set up as a voltage divider, or via Cicero if the frequency needs dynamic control in the experiment. The VCO voltage then passes through a unidirectional coupler that samples a small amount of the RF drive directly to a BNC output. This is in place solely as a diagnostic tool through which a frequency counter can be connected and the frequency of the VCO can be measured. The majority of the RF signal continues past the coupler and into a voltage variable attenuator (VVA). As per its name, the VVA takes in a reference voltage either via a potentiometer set up as a voltage divider, or from Cicero. The VVA is responsible for providing the appropriate attenuation of the RF signal that drives the AOM and therefore controls the amount of power in the desired diffraction order. The last component in the AOM driver chain, prior to amplification, is an RF isolator switch. The switch receives a digital TTL signal from Cicero that switches its function from extreme to minimal attenuation, effectively turning the RF drive on and off.

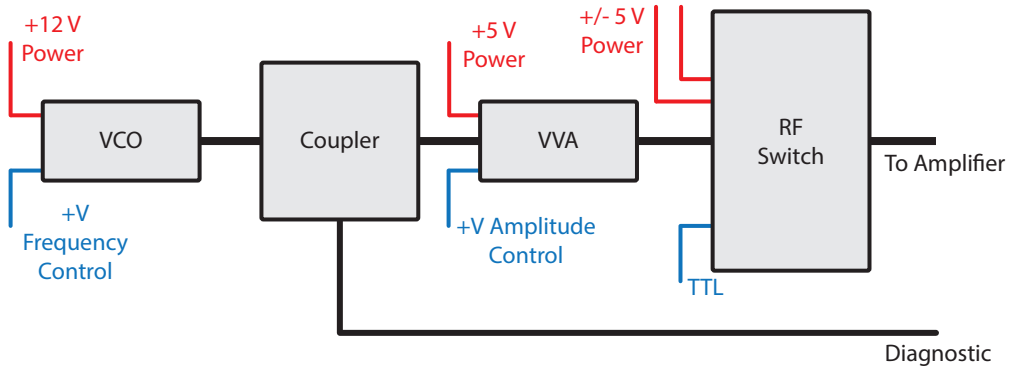

Figure 2.16: A common setup used for generating the RF signal that drives the ^{87}Rb AOMs in our experiment. The voltage controlled oscillator (VCO) generates the RF signal that primarily passes through the coupler, where a small fraction can be measured for diagnostic purposes. The voltage variable attenuator (VVA) then attenuates the signal before passing through an RF isolator switch that functions effectively as an on/off button for the signal to pass to the amplifier, and then the AOM.

The last component in the RF signal chain that controls the AOMs is an amplifier. Typically, the AOMs used in our lab can be fully driven via a 2 W amplifier. Often, there is some attenuation of the VCO signal using the VVA to achieve the highest diffraction efficiency the AOM is capable of providing (usually around 70-80%).

Technical note: On the Mini-Circuits links, it seems Mini-Circuits is cleaning house on what they're selling. Many of the components we've been using are near/are already end-of-life. It's quite possible future upgrades/changes will not use these parts.

On the sodium side of the experiment, the RF source looks different. The sodium spectroscopy double-pass AOM is driven by Mini-Circuits components as described above. The cycling and repumper AOMs, however, have their RF sourced from Direct Digital Synthesis (DDS) cards manufactured by Analog Devices. The DDS takes the role of the VCO, and in their current configuration they are programmed to only output a single frequency. The DDS signal passes through a variable gain amplifier (VGA) which performs the same function as the VVA from before. The VGA, however, has the ability to amplify the signal as well as attenuate, since often the DDS output power is lower than what can be sourced from a VCO. After the VGA, the RF signals are amplified using the standard 2 W amplifiers, as is the case on the rubidium side.

In a similar spirit, laser light frequency can be controlled via electro-optic modulators (EOMs). At the present moment, the only EOM active in the experiment is used for sodium modulation spectroscopy, as detailed in Section 2.2.3. Here, we will briefly cover their operation. Phase-modulated EOMs are constructed with piezo-electric crystals whose index of refraction can be modulated by the application of an oscillating (RF) electric field. Light interacts with this crystal and acquires frequency sidebands. Unlike in AOMs, the beam direction is not modified in this process, as the modulation occurs on the phase of the light. Similar to AOMs, the strength of the RF drive controls the "modulation depth" of the EOM, or the relative amplitude of the sidebands to the carrier, where higher RF power corresponds to a depletion of the carrier into the first- and higher-order sidebands. Unlike in the case of the AOMs, the EOM used for sodium spectroscopy is a *resonant* EOM, which means it does not need a high power amplifier to attain an appreciable modulation depth. The source of the RF drive for our EOM is a Keysight 33420B Arbitrary Waveform Generator.

Active Laser Power Control

Certain beam paths in the experiment, namely the optical dipole trapping (ODT) and future optical lattice beams, require more precise power stabilization than can be generated by the use of a VVA at a fixed set point. To implement active power stabilization we first install the AOM that will control the power. Next, we set the polarization of the first diffracted order such that it has minimal reflection off of a 90-10 beamsplitter (see the graphs here). We then take the reflected light and focus it onto a photodiode that generates voltage signal that is proportional to the ODT power. This signal is combined with a desired voltage setpoint from Cicero into a Stanford Research Systems SIM960 Analog PID controller. This device compares the Cicero setpoint voltage to the voltage of the photodiode and correspondingly sends out a voltage to a VVA or VGA to make adjustments to the strength of the AOM RF drive. Under proper PID settings, this unit dramatically increases the power stability of our ODTs to the $< 1\%$ level.

2.3 Creation and Detection of Cold Gases

One thing that gets lost in the thick of atomic physics research is the almost magical process by which, on a daily basis, we create the literal coldest entities in the universe so frequently that it becomes mundane. I imagine it's much like living in a beautiful area like Seattle, WA – eventually Mt. Rainer is just a background prop while you're stuck in traffic on your way to work. To an outsider, though, there really is stunning beauty to behold. In this section I will detail the process of taking a room temperature gas of atoms and making it millions to billions of times colder.

2.3.1 The Magneto-Optical Trap

To best understand the magneto-optical trap (MOT) it's instructive to know what it actually looks like. Thankfully, we can take pictures of the result with a standard cell phone camera as in Figure 2.17. In these pictures are millions (^{23}Na, yellow) to hundreds of millions (^{87}Rb, red) of atoms held in a space that is several millimeters wide. If you were to measure its

temperature you would see it on the order of hundreds of micro-Kelvin.

Figure 2.17: Cell phone camera images of the sodium (left) and rubidium (right) magneto-optical traps. Pictured are roughly 5-6 million ^{23}Na and 200 million ^{87}Rb atoms at $\sim$200 μK.

The workings of a magneto-optical trap are very nearly analogous to a damped harmonic oscillator from classical physics. Atoms experience two kinds of forces, one of which is purely an optical friction-like force known as optical molasses, the second is a combination of magnetic and optical effects that acts as a spring-like restorative force to coerce the atoms to collect in a particular spot. We'll begin by discussing the frictional force of optical molasses.

Optical Molasses

The friction force of our damped harmonic oscillator is given by a process known as optical molasses. To explain, we can consider a simple two level atom in one dimension with a ground and excited state as shown in Figure 2.18. The states are energetically separated by an amount $\hbar\omega_0$, where $\hbar$ is the reduced Planck's constant. Coming in from the left and right of this atom are two uniform laser beams of equal intensity and frequency ω (and hence energy $\hbar\omega$). The excited state of the atom has a natural linewidth Γ, which indicates that if the atom were excited, it would decay to its ground state and release a photon of energy $\hbar\omega_0$ in a characteristic time of $2\pi/\Gamma$. Now, we can consider what happens in this situation for various choices of ω and atom velocities $\vec{v}$.

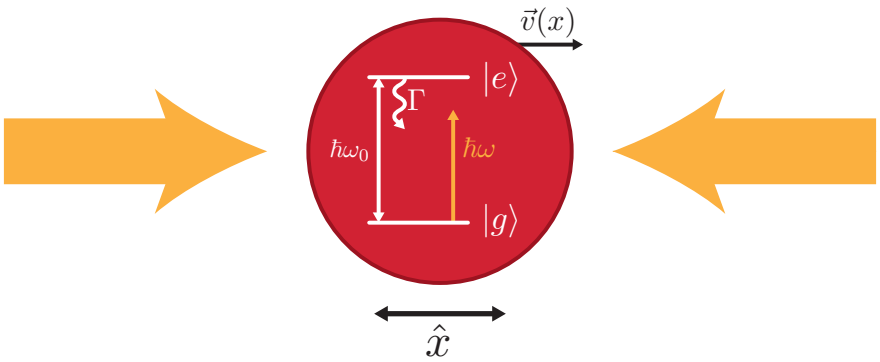

Figure 2.18: A two level atom in one dimension. Laser light has energy $\hbar\omega$ while the ground to excited state energy of the atom is $\hbar\omega_0$. The light is shone in with equal intensity from both the positive and negative $\hat{x}$ direction. The atom has an excited state decay rate of $\Gamma/2\pi$ and a velocity $\vec{v}(x)$.

Consider first the atom at rest and laser frequency $\omega = \omega_0$. The photons in the laser beam carry a momentum $\vec{p}_{\text{photon}} = \hbar\vec{k}$. Here, $\vec{k}$ is the wave vector whose magnitude is given by $2\pi/\lambda$. As the atom is illuminated from both sides, it is equally likely to absorb a photon from either beam and be promoted to its excited state. Momentum must be conserved, so the atom will begin to move with a velocity $\vec{v}_{\text{atom}} = \vec{p}_{\text{photon}}/m_{\text{atom}}$ in the direction of the photon that was absorbed from the laser field (for reference, in ^{23}Na and ^{87}Rb the velocity associated with the release or absorption of one resonant photon is 29 mm/s and 5.8 mm/s, respectively). At a later time, the atom will decay to its ground state via spontaneous emission and emit another photon in a random direction, and in so doing gain another momentum kick *opposite* the direction of the emitted photon. Imagining this process repeating over many cycles, the atom will continue to be excited and decay, gathering equal velocity kicks to the left and right from the laser fields, and the effect of spontaneous emission will average out as a zero-velocity contribution since emitted photons will travel out in all directions. If we consider what the goal of laser cooling is, which is to slow atoms down, this case is clearly not ideal. The atom we considered was already not moving, and we're causing it to effectively bounce around and go through cycles of excitation and decay.

Let us now consider the case of $\omega < \omega_0$, and more specifically $\omega_0 - \omega \approx 3\Gamma$ (we will refer to this as *red detuning* later in this text). For an atom at rest, the rate of absorbing photons from either beam is low to negligible. As mentioned, this is desirable since the atom is already doing what we want by not moving. Now consider the atom moving with some

velocity $\vec{v}$ to the left. In the reference frame of the atom, the beam from the left will be Doppler shifted to a higher frequency, much in the same way as a person standing on the sidewalk will hear an ambulance siren if the ambulance is moving toward them. If the atom is moving sufficiently fast enough, the beam gets closer to resonance and it will absorb photons from that beam at a higher rate. Since momentum is conserved the atom will continually be "kicked" opposite the direction of its travel upon photon absorption. As the atom decays by spontaneous emission, the additional momentum kicks will again average to zero. The net effect will be that the atom receives many kicks opposite the direction of its travel until it is moving slowly enough that the beam is sufficiently far from resonance in the atomic frame. If we consider the other beam that comes from the right, the opposite is true. This beam is Doppler shifted to even lower frequencies, and hence further from resonance, and therefore the likelihood of an atom absorbing a photon traveling left as it itself is moving left is reduced. The left-moving beam does, however, slow down atoms that move to the right. This is optical molasses. If you extend this to three dimensions, where red-detuned beams are shone from all three directions, it becomes the case that no matter which direction an atom is moving, it will receive a kick opposite the direction of its travel. The effect is much like friction, with a damping force that opposes motion ($\vec{F} \propto -\vec{v}$). In a sense, the atoms are moving through *molasses* when placed in this *optical* field.

The Zeeman Effect

Optical molasses is a powerful technique for slowing atoms down, however it alone is not a trap. There is no preferred *position* for atoms that are slowed. To coerce the atoms to collect in a specific point in space, we will need to add a position dependent force. We will do so by the application of a magnetic field gradient, but first we must understand the atomic states and to see why this strategy will work.

Consider the level diagrams from Section 2.1. The atomic states that are being connected via laser fields are hyperfine states with angular momentum F, and therefore also angular momentum projection m_F. As hyperfine states arise due to the interaction of the nuclear magnetic moment with the magnetic field of an orbiting electron, the energy of these states

is affected by the application of an external magnetic field $\vec{B}$. This is known as the Zeeman effect, and its magnitude is given by $V_{\text{Zeeman}} = -\vec{\mu} \cdot \vec{B}$. Here, $\vec{\mu}$ is the magnetic moment of the atom and is given by $\vec{\mu} = -g_J \mu_B \vec{J} + g_I \mu_N \vec{I}$, where $g_{J,I}$ are the Lande g-factors, $\mu_{B,N}$ are the Bohr and nuclear magnetons, and $\vec{J}, \vec{I}$ are the total electron and nuclear spins. In the case of a small magnetic field, the quantity $\vec{F} = \vec{I} + \vec{J}$ is conserved, and so the Zeeman effect simplifies to $V = g_F \mu_B m_F B$ where

$$g_F = \frac{F(F+1) + J(J+1) - I(I+1)}{2F(F+1)} g_J.$$

Now we will employ the information about the Zeeman effect to another two-level atom in one dimension. This time we will consider the ground state as $F = 0$, and the excited state as $F = 1$, indicating that it has $m_F = 0, \pm 1$ projections. Additionally, laser fields red-detuned from the atomic resonance are present and propagate in positive and negative x as shown in Figure 2.19. In the case of no magnetic fields, all of the same considerations from the previous section hold true. We will now consider the addition of a linear magnetic field gradient $B(x)$, where positive and negative values correspond to the direction of the field, and $B(0) = 0$. Shown in the figure is the response of the various m_F energy levels in the atom. In positive x, the $m_F = -1$ excited state lowers its energy, and therefore gets closer to resonance with the light field. Propagating in $-\hat{x}$ is a laser beam with σ_- polarization, or circularly polarized light with the correct chirality to drive $m \to m - 1$ transitions. Therefore, if an atom were displaced in $+\hat{x}$, the magnetic field will shift the $|F, m_F\rangle = |1, -1\rangle$ state closer to resonance with light that will push it into $-\hat{x}$. The case is mirrored with the opposite state and polarization when the atom is displaced in $-\hat{x}$. Therefore, the Zeeman shift and the application of a magnetic field gradient combine with the effect of radiation pressure from the light field to provide a *position* dependent force on the atoms.

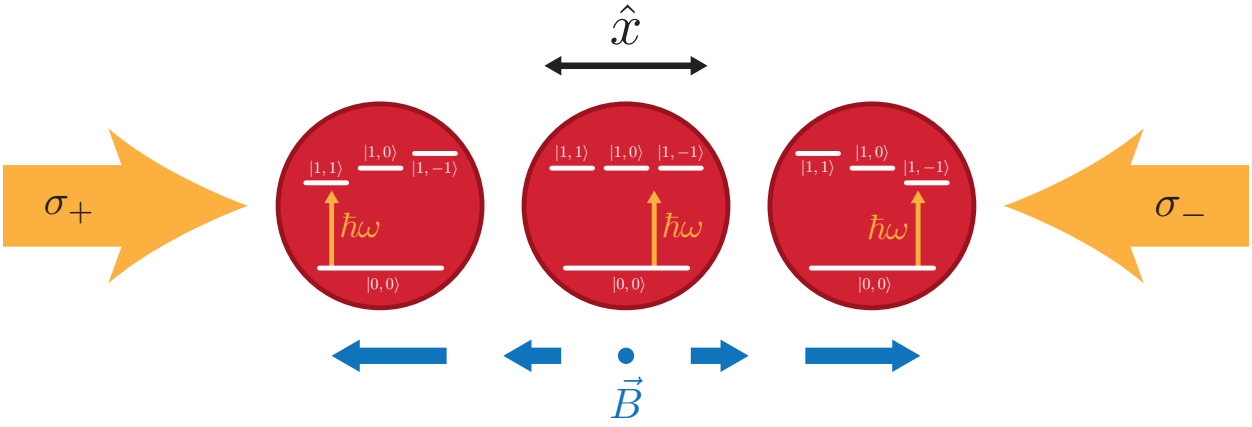

Figure 2.19: A two level atom in one dimension. Laser light with energy lower than the ground to excited state energy splitting ($\hbar\omega_0 > \hbar\omega$) is shown in positive and negative $\hat{x}$. A magnetic field gradient $\vec{B}(x)$ breaks the degeneracy of the excited state projections denoted by $|F, m_F\rangle$.

Real Atom Considerations

The explanations for optical molasses and the Zeeman effect on the hypothetical "two-level" atom go a long way in explaining how MOTs are formed, but there are more considerations when working with actual atoms. The first, and most important distinction, is that *real* atoms have more than two levels, as seen in Section 2.1. One key assumption in the previous description of optical molasses was that when the atom decayed, it would only decay to the one available ground state. However in the case of sodium and rubidium, there are two hyperfine ground states in $F = 1$ and $F = 2$, which are separated by GHz. Therefore, if one were attempting to do optical molasses from the $F = 2$ state, and there was an undesired decay into $F = 1$, that atom would no longer be resonant with the light and therefore the scheme would fail.

To counteract this, we can utilize the fact that there are multiple excited states and effectively make the many-level atom as similar to a two level system as possible. Recall in the case of sodium and rubidium that the D_2 excited state (3 or 5 $P_{3/2}$) has hyperfine levels $F' = 0, 1, 2, \text{and } 3$. We can define driving an atom from $F = 2 \rightarrow F' = 3$ as the cycling transition. The dipole selection rules governing how a spontaneous decay can occur indicate that $\Delta F = 0, \pm 1$. Since the $F' = 3$ state cannot decay to a lower $F = 3$ or $F = 4$ state, as those states don't exist, then it must decay back to $F = 2$. Therefore, the

two-level approximation is quite good. Unfortunately, though, the $F' = 2$ state also exists. When driving the cycling transition there is a small probability (that varies depending on the specific atom) that a transition from $F = 2 \rightarrow F' = 2$ occurs. In this case, again dipole selection rules indicate that the decay must be to $F = 1, 2, \text{or } 3$. Since $F = 3$ doesn't exist, that doesn't matter, but $F = 1$ certainly does. If the atom decays to this state it is effectively lost to the cycling light, and therefore we must add an additional laser for this eventuality.

This leads to the introduction of the repumper transition. In both sodium and rubidium, this is an additional laser field which couples $F = 1$ to $F' = 2$ such that *if* an atom decays to $F = 1$, it'll get re-excited to $F' = 2$ until it decays back to $F = 2$ and can rejoin in the cycling transition. They key determining factor to how important this repumper transition is, is the size of the excited state linewidth compared to the excited state hyperfine splitting, where lower ratios are preferred. In rubidium, the excited state linewidth is about 6 MHz, while the $F' = 2$ to $F' = 3$ hyperfine splitting is about 267 MHz. In sodium, these numbers are 9 MHz and 58 MHz, respectively. In both cases, the fraction of atoms that are accidentally leaked into the repumper transition is low, therefore when laser cooling we can get away with having a significantly lower repumper power as compared to cycling.

The summed effect of optical molasses, the Zeeman effect, and the additional repumping laser all combine to give the magneto-optical trap. This is the starting point of many modern atomic physics experiments today. Figure 2.20 shows, in our experiment, what the effect of (a) cycling light detuning from resonance, (b) total cycling light power, (c) the strength of the magnetic field gradient, and (d) the repumping beam power have against the loaded atom number in a magneto-optical trap of ^{87}Rb. This procedure is done to optimize sodium's atom number as well.

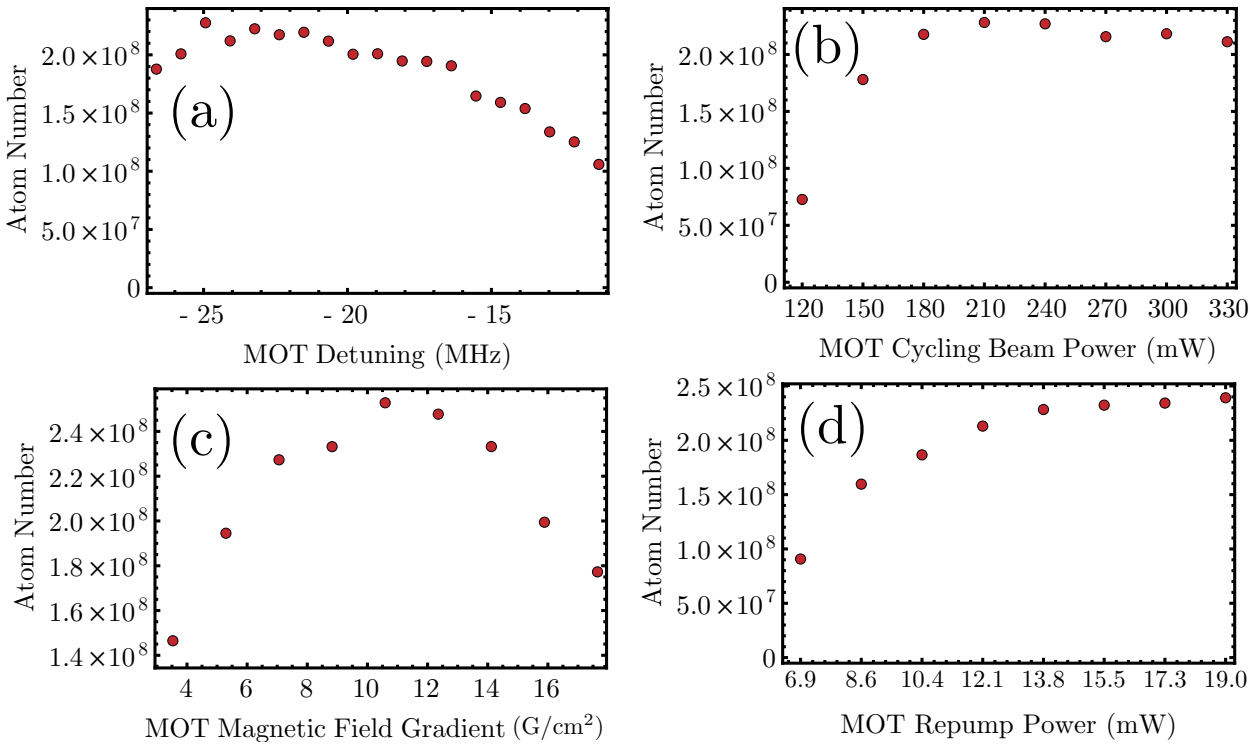

Figure 2.20: Graphs showing the number of ^{87}Rb atoms loaded into a magneto-optical trap as a function of: (a) the detuning of the cycling beam from resonance, (b) the combined power of the cycling beams, (c) the strength of the magnetic field gradient, and (d) the total power of the repumper beam.

2.3.2 Sub-Doppler Cooling

Despite being many orders of magnitude colder than any daily lived experience, magneto-optical traps are actually quite hot on the scale of atomic physics experiments. The naïve limit on how cold magneto-optical traps can get is set by the atom's natural linewidth, which factors into the Doppler temperature, $T_D = \hbar\Gamma/2k_B$. For rubidium and sodium, these correspond to 145.57 μK and 235.03 μK [41, 43]. In order to circumvent the Doppler limit and achieve temperatures in the single micro-Kelvin to hundreds of nano-Kelvin regime, additional cooling stages must occur. We will discuss two of the primary mechanisms, polarization-gradient cooling (annoyingly, the colloquial term for this is optical molasses) and evaporative cooling.

Polarization Gradient Cooling

The famed explanation for polarization gradient cooling refers one to the ancient Greek legend of Sisyphus. As the story goes, the god Zeus was particularly unhappy with King Sisyphus for his having cheated death, amongst other wrongdoings. Consequently, Zeus forced Sisyphus to spend an eternity in the underworld, with Hades, pushing a boulder up a hill only to have it fall back down such that he'd have to push it up again. What Zeus could not have foreseen, for a variety of reasons, was that atomic physicists in the late 20th century would appropriate his punishment to explain how atomic state energy levels could be manipulated in particular polarization landscapes created by interfering laser beams.

Consider two laser fields with orthogonal linear polarizations. The interference of two such beams creates a landscape of changing *total* polarization [51]. Over the span of a half-wavelength this total polarization changes between linear, left-circular, linear, and right-circular as shown in Figure 2.21. Polarization gradient cooling relies on the fact that different internal state transitions in atoms have different strengths, as given by their Clebsch-Gordan coefficients. As seen in the figure, the transition mediated by a σ_+ photon between an atom in a ground state $m_F = 1/2$ to the excited state $m_{F'} = 3/2$ is three times stronger than that same photon driving $m_F = -1/2$ to $m_{F'} = 1/2$. Therefore, the effect of the light in a region where there is σ_+ polarization is to lower the energy of the $m_F = 1/2$ state three times more than $m_F = -1/2$. The opposite is true in a region with σ_- polarization, where the $m_F = -1/2$ state is at a lower energy. Now, we can consider the cooling mechanism.

The polarization landscape creates an effective energy landscape for the atoms. Over one half wavelength, there is one region where the $m_F = 1/2$ atoms have the lowest energy, and one region where the $m_F = -1/2$ atoms have the lowest energy. Assume an atom starts in $m_F = -1/2$ in the region of σ_- polarization, if it were to move to a region of σ_+ it will have exchanged some of its kinetic energy for internal potential energy. If the atom were to absorb a σ_+ photon and be promoted to the excited state $m_{F'} = 1/2$, it is more likely to decay down to the $m_F = 1/2$ state that has the lower energy. This process can then repeat many times, where the atom exchanges some kinetic energy for internal potential energy, and then decays to the state that has the lower energy in that region. This repeated process, known

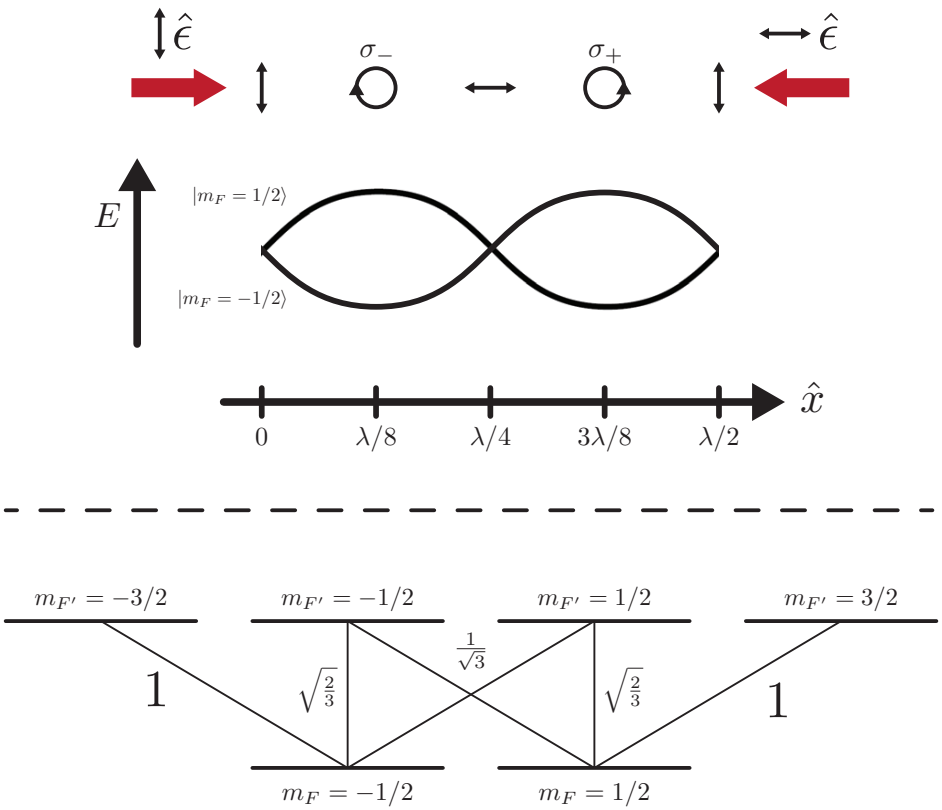

Figure 2.21: Schematic of how polarization gradient cooling works. From $\pm\hat{x}$ are two laser fields with orthogonal polarizations ($\hat{\epsilon}$) interfere and create a cyclic polarization landscape. In this landscape, the energy levels of the two different m_F ground states are modified due to the imbalance of the Clebsh-Gordan coefficients (below) coupling the ground and excited state levels. As such, an atom in the $m_F = -1/2$ moving from position $\lambda/8 \rightarrow 3\lambda/8$ will exchange kinetic for potential energy, is more likely to be excited by a σ_+ photon, and is then most likely to decay down into $m_F = 1/2$, where the process can continue. This figure adapted from Ref. [51].

as Sisyphus cooling, can bring atoms much closer to the *recoil* temperature. Practically in our experiment, this brings rubidium from 150 μK to $\approx$20 μK, and sodium from 200 μK to $\approx$35 μK. As well, in our experiment, the polarization gradient cooling is implemented not by the interference of two linear polarizations as shown here, but by σ_+/σ_- interference. The interfering of two circular polarizations makes the actual description of polarization gradient cooling more involved, but qualitatively they work in the same way.

In our experiment, polarization gradient cooling is implemented by shutting off the magnetic field gradient that generates the MOT, linearly lowering the power of the cycling and repumper beams over several milliseconds, and increasing detuning of the cycling light from resonance. The optimal values of these parameters is found by minimizing the temperature

after polarization gradient cooling. Temperature is calculated from the expansion of the atomic gas in a time of flight as described in Section 2.3.3, and an example is shown in Figure 2.22. In 2.22(a), the effect of the cycling power to polarization gradient cooling is shown. On the left side of 2.22(a) the is the time-of-flight expansion data that is used to generate the temperature data points on the right. Figure 2.22(b) demonstrates the effect of cycling detuning for ^{23}Na on the left and ^{87}Rb on the right. Polarization gradient cooling is a powerful technique for atoms whose excited state hyperfine splittings are well defined, as is the case with both ^{23}Na and ^{87}Rb.

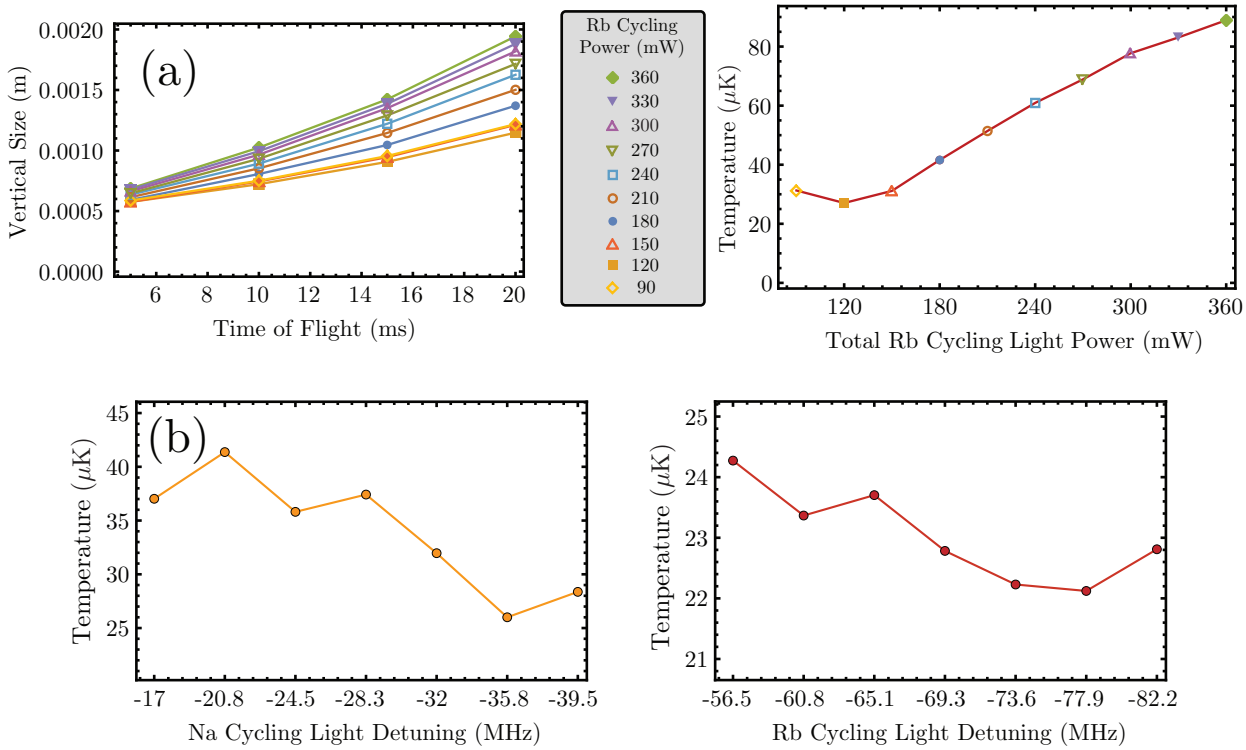

Figure 2.22: (a) Left: expansion of an ^{87}Rb atomic gas after polarization gradient cooling as a function of free expansion time. Each curve represents a different cycling power. Right: the translation of the expansion into a temperature. (b) Temperature of ^{23}Na/^{87}Rb (left/right, respectively) as a function of cycling light detuning from resonance.

Evaporative Cooling

Polarization gradient cooling goes a long way in reducing the temperature of rubidium and sodium, yet it alone is not enough to attain the temperatures and densities necessary for efficient molecule creation. In order to bridge the gap between the tens of micro-Kelvin

after polarization gradient cooling, and the hundreds of nano-Kelvin necessary for molecule creation, we must employ evaporative cooling.

Thankfully, evaporative cooling is a rather simple concept to explain since it has a direct analog to real life human experiences. For instance, a hot cup of coffee set out on a table will undergo evaporative cooling. As the cup sits, the hottest water molecules leave the coffee as water vapor and escape out into the room, leaving the colder water molecules behind. How quickly a cup of coffee gets cold, at least in terms of evaporation, depends on how well the heated water vapor is trapped. Multinational coffee corporations trap the heat of coffee using a "lid," which, on top of making it harder for you to spill your beverage, also forces the hottest water molecules to bounce off of the lid and back onto your coffee.

So too, atoms can be kept hot or made cold using evaporation by having the laser cooling and trapping equivalent of a lid. Translating to more technical language, we can change the potential a gas of atoms experiences in such a way that encourages the hottest atoms to leave, leaving behind a colder collection in the trap. We will see how this works in two cases, the optical dipole trap and RF evaporation from a magnetic trap.

Consider an atom with a resonant frequency ω_0 and excited state linewidth Γ and a laser field with frequency ω such that $\omega_0 - \omega \gg \Gamma$. This is the case, for instance, of a rubidium atom and a laser with wavelength 1070 nm. Since the atom is composed of charged particles, the application of an oscillating electric field at frequency ω creates a force on the atom that induces a dipole moment that will also oscillate with frequency ω [52]. The strength of the induced dipole is given simply by $\vec{p} = \alpha\vec{E}$ where $\vec{p}, \vec{E}$ are the induced dipole moment and the applied electric field, while α is the complex polarizability. The polarizability, in a classical picture of an electric field and dipole, is given by

$$\alpha = \frac{e^2}{2m_e}\frac{1}{\omega_0^2 - \omega^2 - i\omega\Gamma_\omega}. \tag{2.1}$$

Where e is the fundamental charge, m_e the mass of the electron, and Γ_ω is the radiative loss rate. The potential generated by the electric field is $U = -1/2\left\langle \vec{p}\cdot\vec{E}\right\rangle$ where the the brackets indicates the time average. Expanding this, the interaction potential works out to

$$U = -\frac{1}{2\epsilon_0 c}\mathrm{Re}[\alpha]I \tag{2.2}$$

where I is the intensity of the electric field, ϵ_0 the vacuum permmitivity, c the speed of light, and $\mathrm{Re}[\alpha]$ the real part of the polarizability. Now, we can consider the case of large detuning where further simplification gives

$$U(\vec{r}) = \frac{3\pi c^2}{2\omega_0^3}\frac{\Gamma}{\Delta}I(\vec{r}). \tag{2.3}$$

Here, Γ is the linewidth of the excited state and $\Delta = \omega - \omega_0$ is the detuning. One sees the depth of the potential is linearly proportional to the intensity of the laser creating the optical dipole trap. Therefore, for application in evaporative cooling, we will dynamically lower the intensity of the beam (by reducing the power) in such a way that the hottest atoms with the most kinetic energy are able to escape, leaving the coldest behind.

To give a frame of reference for the strength of the optical dipole force let us consider ^{87}Rb atoms and an optical dipole beam with wavelength 1070 nm with a power of 10 W that is focused via a lens to a minimum beam waist (radius) of 100 μm. The optical dipole potential depth in these conditions translates to approximately 80 μK. This is why it is still necessary to pre-cool the atoms in a magneto-optical trap and perform sub-Doppler cooling prior to using this evaporation scheme, as a room temperature gas is simply too hot to be affected in a meaningful way by this optical dipole force. An example of atoms held in an optical dipole trap is shown in a false color image in Figure 2.23.

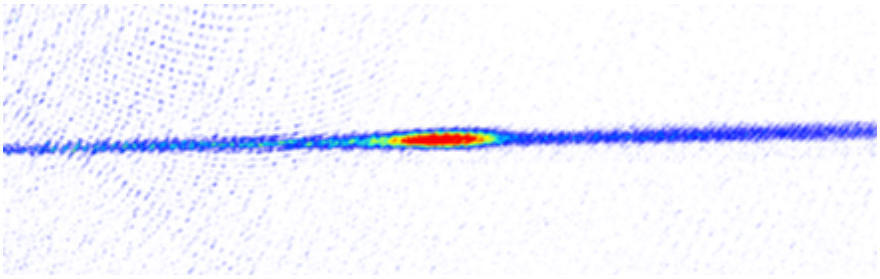

Figure 2.23: A false color image of ^{87}Rb atoms in a 1070 nm optical dipole trap. The atoms can be seen collecting in the region of highest beam intensity.

A second pathway to evaporating atoms is via the use of a magnetic field gradient and

an oscillating RF or microwave magnetic field. First, we must understand a how a magnetic trap works.

The hyperfine quantum numbers of ^{23}Na and ^{87}Rb relate to their respective magnetic moments. In both cases, the $|1,-1\rangle$, $|2,1\rangle$, and $|2,2\rangle$ states are known as "low-field seeking" due to the fact that their energies are increased in the presence of a magnetic field (well below the Paschen-Back regime where F is no longer a good quantum number) [41, 43]. As such, in applying a magnetic field gradient as one does in a magneto-optical trap, the region of lowest $|\vec{B}|$ is directly at the center of the gradient. The potential a magnetic dipole feels in a magnetic field gradient is given by

$$U(x,y,z) = \mu B' \sqrt{\frac{x^2}{4} + \frac{y^2}{4} + z^2}, \tag{2.4}$$

where B' is the magnetic field gradient, μ is the magnetic moment, and x, y, and z are the distances from the zero point of the gradient. The factors of 4 in x and y are due to the geometry of a pair of circular magnetic field coils with a radius to coil separation ratio of 1/2, and it practically means the z-axis confinement is twice that of x and y. The size and temperature of a gas are closely related in a magnetic trap. The potential created by the magnetic field gradient looks like a "V" (say, if one fixes $x = y = 0$ and looks at the form of the potential in the z direction). An atom with some kinetic energy will explore a range of distances within the V-shaped potential, consistently exchanging kinetic and potential energies as it moves back and forth around the magnetic field zero. Atoms with higher temperatures will reach further away from the zero before they turn around and repeat their journey. Notably, hotter atoms will, on average, spend less time near the center of the magnetic quadrupole trap. This is because their higher kinetic energy gives them faster speeds as they pass through the magnetic field zero. This leads to the primary drawback of magnetic trapping.

As mentioned, only certain $|F, m_F\rangle$ states that increase their energy in a magnetic field are trapped by a quadrupole trap. However, at zero magnetic field, the energies of every projection state (that is to say $|1, m_F\rangle$ or $|2, m_F\rangle$) are degenerate. Therefore, for very cold gases in a magnetic quadrupole trap, the amount of time spent in a region where all the m_F

states are degenerate means the atoms can change to an untrapped state and be removed. This phenomenon is known as Majorana loss, and it requires some additional complication to the quadrupole trap in order to achieve very low temperatures. We will revisit this complication after discussing the mechanism by which evaporation occurs in a magnetic trap.

The very thing that makes a magnetic quadrupole trap ineffective at low temperatures is also what allows evaporation to occur - namely that the energy level spacings of the $|F, m_F\rangle$ hyperfine states are position dependent. The differential energy level splitting between the m_F projection states in both ^{23}Na and ^{87}Rb is 0.7 MHz/G, meaning in a 10 G magnetic field, the $|1, -1\rangle \rightarrow |1, 0\rangle$ energy splitting is 7 MHz. As mentioned, atomic temperature and position within a quadrupole trap are related, therefore the transition frequency between m_F states is also temperature dependent, with the hottest atoms experiencing the largest m_F Zeeman splittings. Therefore, via the application of an RF magnetic field, one can selectively drive transitions for hotter atoms from a trapped to an untrapped m_F state. Practically, this involves applying an RF magnetic field that sweeps its frequency from a high to low value, kicking out all atoms that were hot enough to have the corresponding Zeeman splittings. This provides the energy selectivity necessary for RF evaporative cooling. For appropriately timed RF frequency sweeps, after the hottest atoms are removed the remaining atoms rethermalize to a colder temperature. This process can continue until Majorana losses become significant as a result of the cold atoms spending too much time near the magnetic field zero. A similar procedure can be done with microwaves, driving instead the transition from either $|2, 2\rangle \rightarrow |1, 1\rangle$ or $|1, -1\rangle \rightarrow |2, -2\rangle$.

For evaporative cooling of sodium and rubidium simultaneously, magnetic trapping with microwave evaporation is desired. The reason for this is twofold. One is that in our experiment we start with significantly more rubidium than sodium. Therefore, we want to evaporate rubidium to colder temperatures and use it to sympathetically cool sodium. (Sympathetic cooling just means the two atomic species can thermalize with one another, and they will due to their nice scattering properties as mentioned in Section 2.1.3). Selective evaporation of rubidium can occur with microwaves, since its $|1, -1\rangle \rightarrow |2, -2\rangle$ transition occurs at 6.8 GHz, compared to sodium's 1.7 GHz. The second reason is that sodium's trap

depth in an optical dipole trap is generally lower than rubidium's (e.g., for near-infrared wavelengths such as 1070 nm). This means that in a typical all-optical evaporation scheme, sodium will always evaporate prior to rubidium. As well, less sodium is collected in an all-optical trap due to the fact that its post-polarization gradient cooling temperature is hotter and its trap depth is lower than that of rubidium. A magnetic trap is equally strong for both atomic species due to the fact that they have the same magnetic moments.

The last hurdle to overcome in the magnetic trapping scheme is the fact that sufficiently cold gases suffer from Majorana losses. This can be overcome via the use of a "hybrid" trap, which is the combination of both the optical dipole trap and the magnetic trap. Essentially, the primary evaporation occurs in the magnetic trap. A displaced optical dipole trap creates a second potential minimum for the atoms away from the magnetic field zero. Consequently, when the atoms are cold enough they can be adiabatically loaded into this displaced optical dipole trap. A rigorous explanation of hybrid trapping can be found here [53]. We will seek to implement a similar hybrid trapping approach to Dajun Wang's group as detailed in Ref. [54, 55]. To diagnose how close our optical and magnetic traps are, though, we must be able to see them both. This takes us to our next section on how to image atomic gases.

2.3.3 Imaging Atom Number and Temperature

One of the main diagnostic tools atomic physicists have to interface with their atoms are pictures. Taking images of atoms under various conditions can allow for a quantitative analysis of atoms or atomic cloud properties. We employ two techniques to this end, absorption and fluorescence imaging. We will also discuss how to measure the temperature of an atomic cloud using its expansion in time of flight.

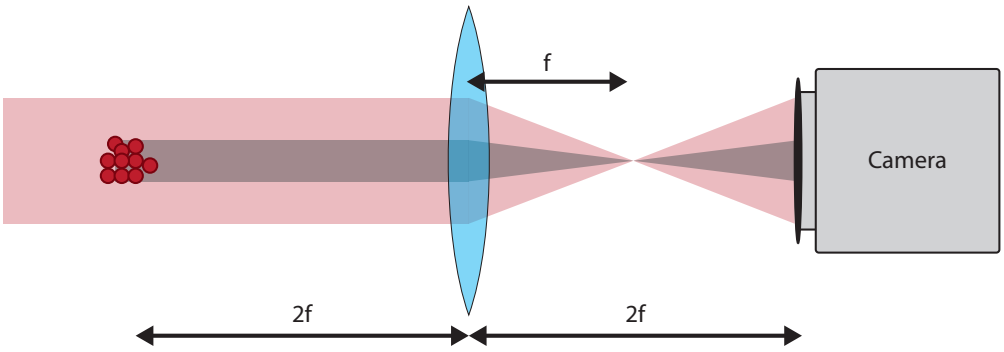

Figure 2.24: Cartoon image depicting the process of absorption imaging. Resonant light incoming from the left is absorbed and re-emitted by the atoms, casting a shadow. The light is collected in a 2f-2f imaging system that recreates the size of the shadow and imaging beam on the camera.

In absorption imaging, diagrammed in Figure 2.24, the primary idea is that atoms cast a shadow in a beam of resonant light. The "darkness" of the shadow is a measure of the number of atoms present, while the size of the shadow corresponds to the atom cloud size. The sequence for our absorption imaging is the following:

1. Shine a resonant beam of light on the atoms for approximately 100 μs while the camera is exposed
2. Wait for camera pixels to clear and reset for another image, approximately 200 ms
3. The atoms will have dissipated in the previous step, now expose the camera to just the imaging beam for the same exposure time of 100 μs
4. Wait again for the camera to recover from the exposure
5. Take an image with nothing to calibrate the "background."

Translating the three images to an atom number requires the application of Beer's law. The primary idea is captured in the equation below:

$$n(x,y) = -\frac{1}{\sigma}\ln\left(\frac{I(x,y) - I_{\text{bg}}(x,y)}{I_0(x,y) - I_{\text{bg}}(x,y)}\right). \tag{2.5}$$

Here, $n(x,y)$ is the column density of the atoms, σ is the scattering absorption cross section, $I(x,y)$ is the intensity of the imaging beam when atoms are present, $I_{\text{bg}}(x,y)$ is the background image with no light or atoms present, and $I_0(x,y)$ is the intensity of the beam with no

atoms present. The negative of the logarithm quantity is known as the optical depth (OD), where higher values correspond to higher atomic densities. The scattering absorption cross section depends on a variety of factors, primarily the detuning of the light from resonance, the polarization, and the states that are being used for imaging. For our analysis, where we keep certain to be below the saturation intensity [41, 43] the scattering cross section is given by

$$\sigma = \frac{\sigma_0}{1 + 4(\Delta/\Gamma)^2 + (I_0/I_{\text{sat}})}, \tag{2.6}$$

where $\sigma_0 = \hbar\omega\Gamma/2I_{\text{sat}}$ is the resonant scattering cross section, Γ is the excited state linewidth, Δ is the detuning from the cycling transition, and I_{sat} is the saturation intensity.

In practice for our experiment, the MATLAB code in absorption imaging mode outputs a 2D array with values corresponding to the quantity $-\ln(I(x,y)/I_0(x,y))$, so the Mathematica code simply takes the file and divides it by the scattering cross section, which is determined by a user defined Δ and I_0 per Equations 2.5 and 2.6. Two sample images of rubidium absorption imaging under nearly identical situations are shown in Figure 2.25. These highlight an additional consideration when doing absorption imaging which is *saturation*. Ideally, one would always work with a detuning $\Delta = 0$ to be the most sensitive to the effect of the atoms on the imaging light. However, when the atomic cloud is so dense that none of the imaging light can pass through, the optical depth "saturates." This makes it impossible to gather accurate density information about the atomic cloud and necessitates an intentional detuning from resonance. In order to agree on the number of observed atoms we divide by the appropriate off-resonant scattering cross section for our detuning. Saturation effects become important when the optical depth of the sample exceeds 2. As OD is a logarithmic quantity, an OD of 2 corresponds to $1/e^2$ of the incoming light passing through the atoms.

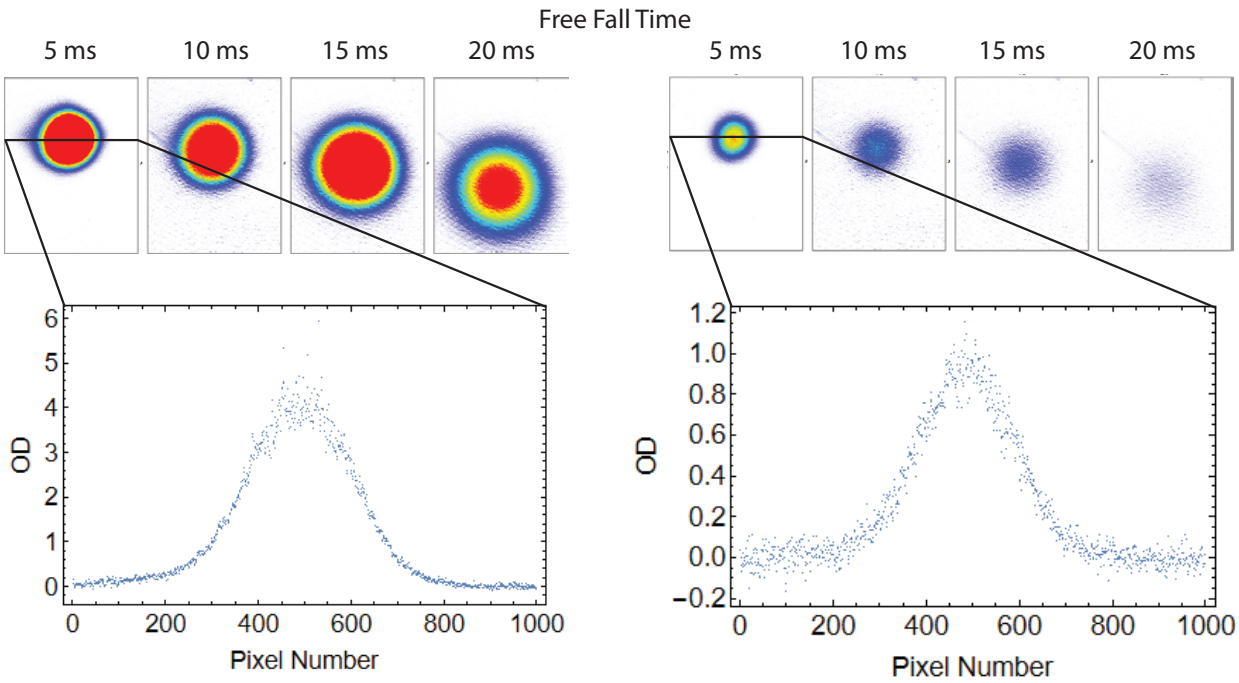

Figure 2.25: Absorption images taken of rubidium after being released in free fall for varied times. The images are a false color representation of column density of the atoms. On the left is an example of on-resonant imaging and a display of saturation. On the right is a collection of atoms taken under the same condition but imaged with an intentionally detuned beam. The black bar corresponds to a "line-cut" of the image, where the plots below the images shows the optical depth as a function of pixel number for that particular row in the image.

Lastly, we need to determine the size of the atomic cloud from the image. As the camera is composed of pixels, the base assumption is that the real space dimensions of the pixels translate directly to the real space dimensions of the picture. For the Thorcam we use, this is $5.86\,\mu$m/pixel. Refinement of this size comes from understanding the magnification of our imaging system. In Figure 2.24 a "2f-2f" imaging system is shown, which nominally has a magnification of one. However, imperfect placement of the lens and camera can modify this slightly. As such, we can verify the actual imaging system magnification by checking against a simple concept - release the atoms in free fall for a defined amount of time and measure how far they drop. Their center of mass motion should correspond very well to $z(t) = gt^2/2$ from first semester introductory physics, where g is the gravitational acceleration constant near the earth's surface, and t the amount of time spent falling. Our measure of g against the expected value gives a magnification, and hence an effective pixel size for our imaging system. Once we are confident on the calibration of our pixel size, we attain the information

on the total cloud size by doing OD integration along both the x and y directions. We fit the integrated ODs to a Gaussian distribution to extract the cloud sizes. This concept is shown in Figure 2.26.

The second mechanism we employ for atom detection is fluorescence imaging. In this scheme, near-resonant light is shone onto the atoms, however not directly along the imaging axis of the camera. By measuring how much light is re-emitted from the atoms we can extract the atom number. There are several parameters to consider in this imaging scheme. First, is that our imaging system is only able to capture some fraction of the re-emitted light based on the *numerical aperture* (NA) of our first imaging lens, known as the *objective*. The remaining factors for determining how much light makes it to the camera are again captured by the scattering absorption cross section σ. Since this is a function of the intensity and detuning of the light used to fluoresce the atoms, we must ensure that we characterize the fluorescing light well (we typically use the beams that create the MOT) in order to extract an accurate atom number. Fluorescence provides a good alternative when imaging particularly dense clouds where absorption may fail due to saturation effects.

The two imaging methods described above allow us to routinely gather information about the number of atoms we have and their size. In order to measure the atomic temperatures, we use "time-of-flight" (TOF) expansion. At its core, TOF expansion relies on the fact that a classical gas of some temperature T has a characteristic Maxwell-Boltzmann distribution to describe the velocities of the constituent atoms. When released in free fall the atoms will expand, and based on the rate of expansion the temperature can be calculated. There is nice online reference for understanding this expansion here, but practically for us we can consider the below equation:

$$\sigma_i(t) = \sqrt{\sigma_{0,i}^2 + \frac{k_b T}{m} t^2}. \tag{2.7}$$

Here, $\sigma_i(t)$ is the size of the atomic cloud in dimension i at a given expansion time t, $\sigma_{0,i}$ is the cloud size in dimension i at $t = 0$, k_B is Boltzmann's constant, m the mass of the atom, and T is the temperature. We collect the information of $\sigma(t)$ in our experiment and fit the σ_0 and T parameters accordingly. For the images shown in the non-saturated sequence in

Figure 2.25, the time of flight expansion analysis is shown in Figure 2.26. In this particular sequence, the atomic cloud was measured to be $40.2 \pm 1.2\,\mu$K.

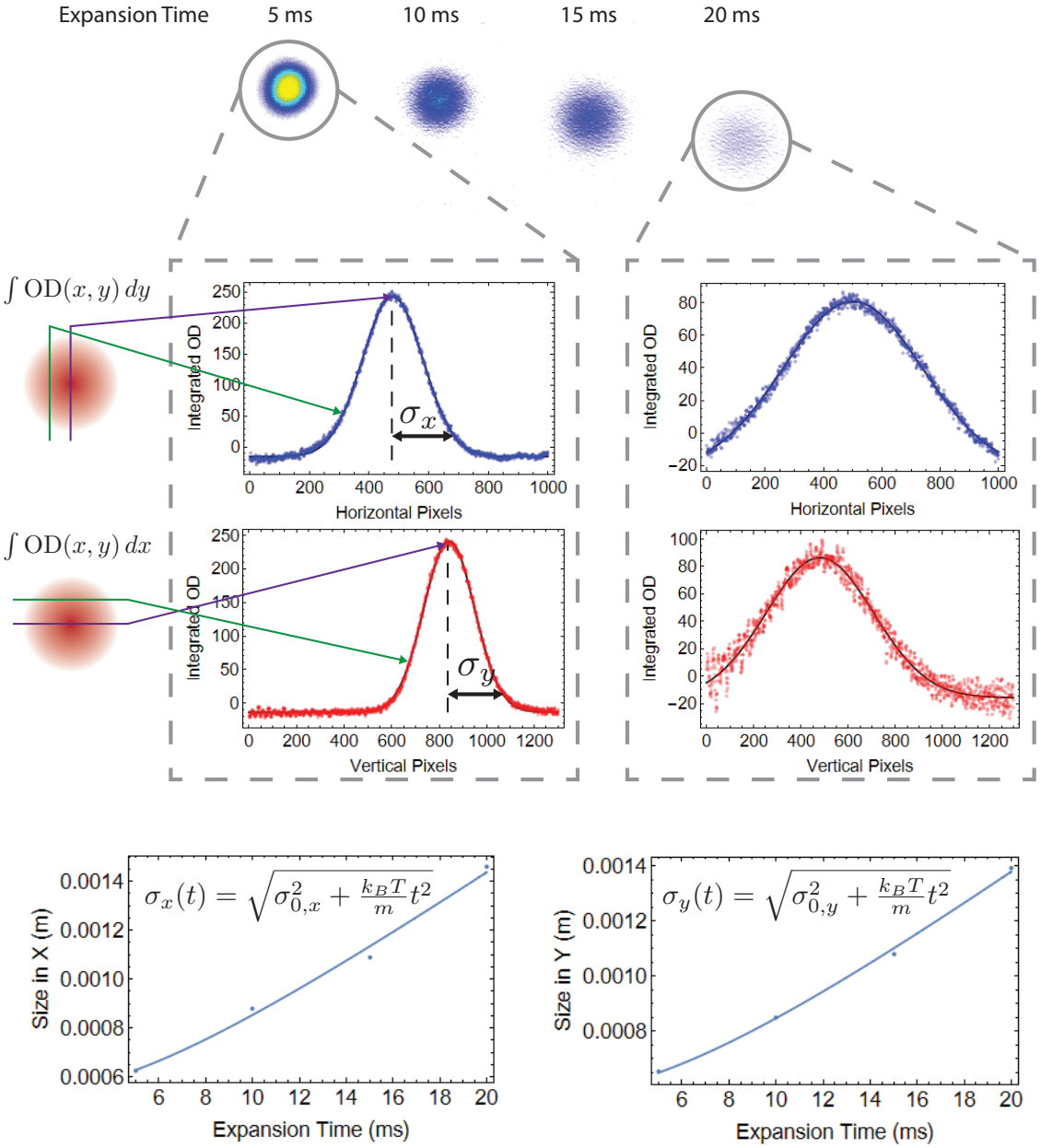

Figure 2.26: A standard time-of-flight analysis to measure the temperature of an atomic gas. Pictures are taken at different free expansion times. The integrated optical depth in both the x and y directions are plotted and fit to a Gaussian distribution to extract their size. The sizes are then plotted and fit using Equation 2.7 to measure the temperature. This particular rubidium cloud has a temperature of $40.2 \pm 1.2\,\mu$K.

2.4 The Walk-In Guide

I beg the reader, if you are not a member of the molecule experiment in the Gadway lab, turn away now. Open a new section of this thesis or even that book you've been meaning to read for the last month. This section contains nothing but an absolutely ultra-specific set of instructions for how to operate our experiment from the moment you walk in to when you're taking images of the atoms. It contains no fruitful scientific insights or explanations, you've been warned.

Upon walking in the lab the first thing to do is turn on the lasers to let them warm up. For rubidium, the laser system is on the northern table. To get this system ready:

1. Turn on the repumper laser using the controller by flipping the switch on the left side of the controller
2. At the corner of the table turn on the beat note locking photodiode with the switch
3. Turn on the cycling laser with the button on the right side of the controller
4. Wait roughly five minutes before looking for lock signals

For sodium's laser system on the south table the turn on procedure is as follows:

1. Enable the seed laser by pressing the "Emission" button on the right side of the DL PRO Controller
2. Turn on the amplification laser (the Ytterbium fiber laser below the DL PRO Controller) by flipping the rocker switch on the bottom right side
3. Allow five minutes to warm up
4. Turn the key on the amplification unit, the SHG indicator light should change from orange to green
5. Go to the north experiment computer and open the VRFA GUI Interface as seen in Figure 2.27.

i. Verify that the input power is ≈12-15 mW (green box)

ii. Set the unit to AUTO mode (blue box) and set the output power to 1 W (purple box)

iii. Enable the laser output (red box)

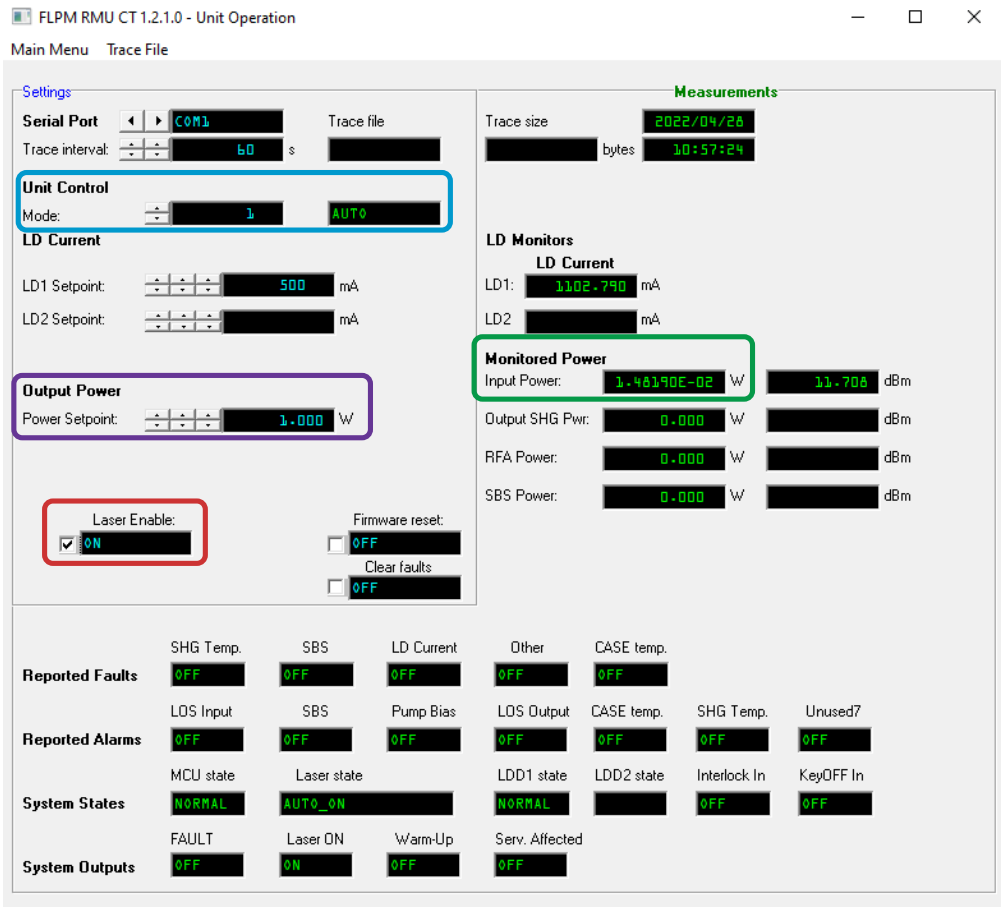

Figure 2.27: The graphical user interface for the ^{23}Na laser. When steps 1-4 are followed you will need to check the input power (green box), set the laser to AUTO (blue box), give the desired output power (purple box), and enable the laser output (red box).

While the lasers warm up, the other components of the apparatus can be turned on. On the south side of the lab turn on the two Keithley Power supplies for our shim coils and the power supply for the 600 turn z-axis coils directly to the right. Next, on the west side of the vacuum chamber table there are the power supplies for the rubidium and sodium dispensers on the top and bottom, respectively. Next, head into the utility room on the north side of the room and turn on the closed loop water pump. There is a switch on the back of the

device that requires a 90° turn. Indicator lights on the front should turn on, and the up arrow should be pressed until the lights align with the marked set point. This corresponds to 120 psi in the line which is more than enough to cool our Feshbach coils. From here, the main power supply for the Feshbach coils can be turned on. It is on the ground on the north side of the vacuum chamber table. Above the table, turn on the power supply for the automotive switches that set the coil's orientation, there will be an audible click.

In a standard day where procedures will be done on the atoms to achieve some goal, the imaging system will need to be turned on. Head to the south computer and open MATLAB. On the left side of the program is the home-built ThorCam interface program. Select the program and hit F9 to start it. Follow the prompts as desired. The correct answer to "Does Micheal Suc?" is "y" (what this actually does is enable or disable a chime that plays any time an image is acquired, and it's typically unnecessary). An example is shown in Figure 2.28.

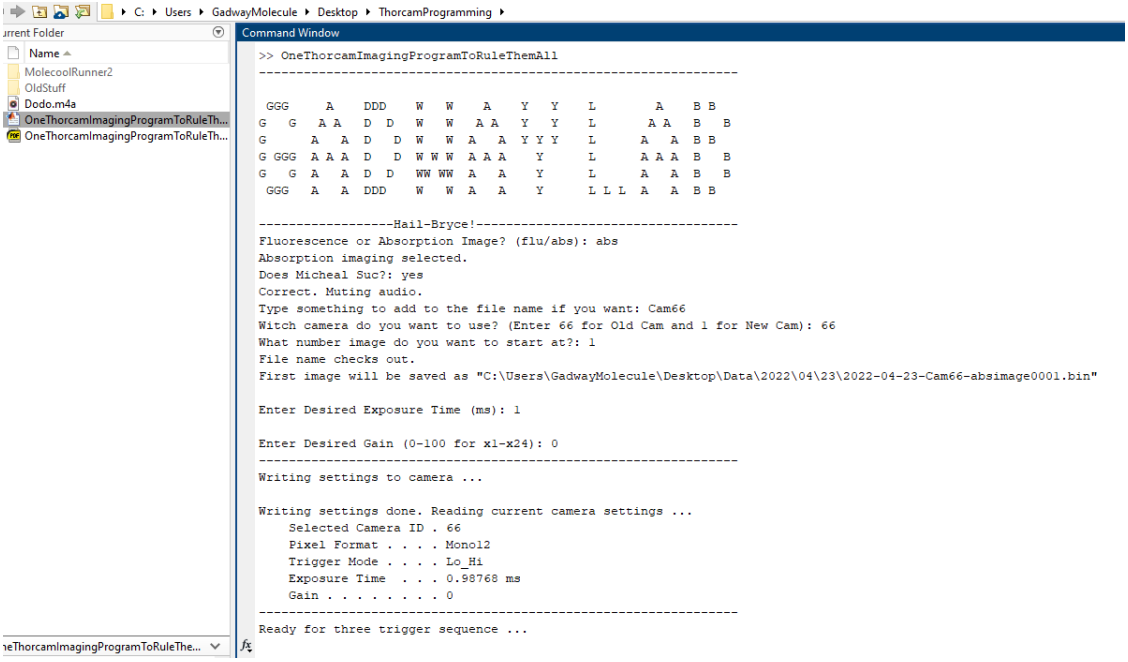

Figure 2.28: Example of how to set up absorption imaging on the Thorcam using the custom MATLAB software.

Next, look for the spectroscopy signals. For rubidium you will start with the cycling laser. Set the scan amplitude to 2-3 using the "amplitude" knob at the top left of the controller. For those who are very lucky, you may immediately see the characteristic signal as shown in Fig. 2.10. Otherwise, you're most likely to be encountered with a flat line on

the oscilloscope trace. **Typically**, the only thing that needs to be done to see the correct signal is to increase the current by turning the current potentiometer ("current/power" black potentiometer on the right side of the controller) clockwise until you see the flat line on the oscilloscope trace "jump" up. Then, slowly reduce the current and the spectroscopy signal is likely to emerge in the lowering process. You will then modify the piezo voltage ("offset adjust" black potentiometer on the left side of the controller) and current in such a way as to center the zero-crossing of the slope to the center of the scope. You should verify that the peak and trough of the spectroscopy signal lie within the two green horizontal cursors to ensure that you're locking the laser to the same point on a day-by-day basis. Once the signal is appropriately centered you should confirm that the laser is not near a mode hop by slightly increasing and decreasing the current ($\pm$1-2 mA). You should watch the signal move left and right but *not* change in size or go away completely. If it does, you likely need to adjust the current and piezo slightly to move the mode hop further away. For the last couple years, the current has not needed to stray very far from 268 mA, and the potentiometer for the piezo should be close to the middle of its range, indicated by a "5" on the top part of the knob. Once the spectroscopy signal is behaving well, turn down the scan amplitude such that it looks like you're zooming in on the negative slope zero-crossing. Continue to decrease the scan amplitude all the way until there is a flat line, then switch on the lock using the "lock–off–scan" switch in the second panel of the controller.

Once the cycling laser is locked, remove the paper card that blocks the input light to the tapered amplifier (just to the right of the laser body). Head to the tapered amplifier and press the "LD On" button to enable its output. Next, head to the repump laser. More likely than not the characteristic locking signal is already there. This laser has the best day-to-day stability in the lab and often only needs a minor frequency and current knob adjustment to get the appropriate zero-crossing at the center of the oscilloscope trace with no mode hops nearby. Confirm the signal appears as it does in Figure 2.29. This laser does *not* need its scan amplitude turned down. Once the zero crossing is in place, switch the lock on using the lock/scan switch in the center of the controller.

For sodium, the search for the spectroscopy signal is typically not arduous. If it does not immediately show up, press the "scan" button on the bottom left of the screen and use a

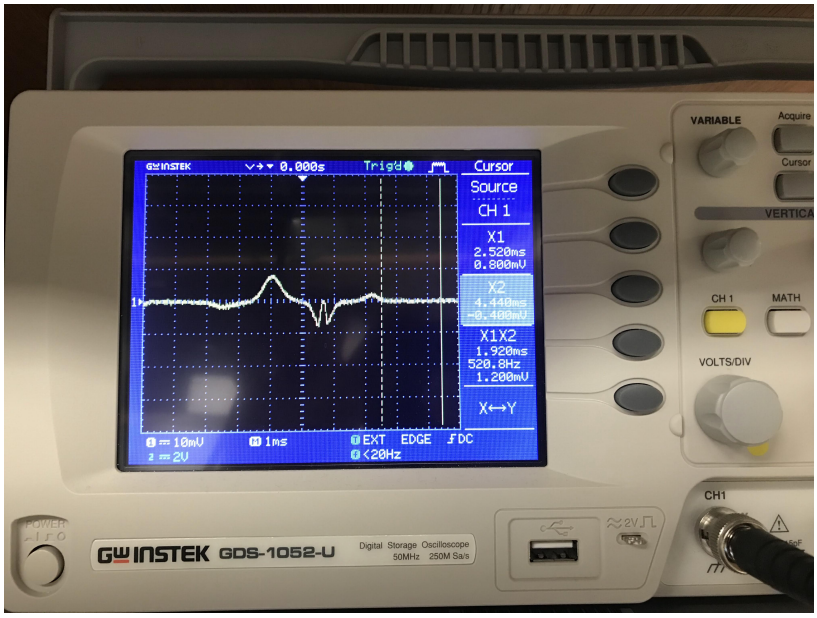

Figure 2.29: Standard oscilloscope trace for the rubidium repumping laser. The desired zero crossing is shown centered on this trace.

horizontal pinching motion to "zoom out," which is increasing the scan amplitude (you can see the scan voltage in the bottom left of the screen). Set this to be about 1-2 V. You will then look in the piezo voltage range between 70-90 V. You can adjust the DC piezo voltage level by using one finger and dragging the signal to the left or right. The spectroscopy signal should be somewhere in this range. If not, you'll want to determine if there are any mode hops. These typically manifest as the entire signal noise level that looks larger than that seen in Fig. 2.12. The current can be adjusted using the top right knob to see these mode hops go away. Typically the spectroscopy signal can be found with a current near 320 mA and a piezo voltage around 75 V. Once the lock signal is found, press the "Lockpoint" button at the bottom center of the screen. The controller should have automatically found the lock point. Ensure that it is selected and then press the lock button (third rectangular button from the top at the left side of the screen, also nominally shows an open padlock).

Once this set of instructions is followed the experiment should be ready for normal operation. Before running the apparatus you'll want to copy over the previous day's Mathematica notebook into the new folder generated in "Data" by the MATLAB program and make appropriate file naming changes.

Chapter 3

Nondestructive Imaging of Rotationally Excited Molecules

3.1 Preamble

This chapter is primarily a transcript of Ref. [40] with edits made for readability and updated information since its publishing. This paper was written in collaboration with Qingze Guan and Svetlana Kotochigova from Temple University, as well as Vito Scarola from Virginia Tech. I would like to extend my gratitude to them for their incredible work.

3.2 Background on Dispersive Imaging

Dispersive imaging is based upon interference of two or more off-resonant laser beams that have acquired a relative phase due to their different propagation through an atomic [56, 57] or molecular medium. While the two beams can propagate along distinct paths [58, 59] or involve distinct spatial regions of a single probe beam [57, 60], approaches based upon co-propagating polarization [61, 62] or frequency [63] components have the benefit that they are simple, robust, and inherently afford significant common-mode noise rejection. For atoms, which typically possess cycling transitions, dispersive imaging has proven especially useful for niche applications in which one does not want to disturb density or temperature, so as to allow for continuous monitoring of a sample [64, 65].

For molecules that lack true cycling transitions, however, dispersive imaging may provide the best means to achieve high-fidelity imaging. Therefore, the development of such a technique has the potential to find more widespread use for bi-alkali molecules and other species, while still allowing for nondestructive imaging. Polarization-based dispersive imaging thus promises to leverage one of the characteristic qualities of molecules – their anisotropic tensor polarizability [19] – for high-fidelity imaging and internal state detection.

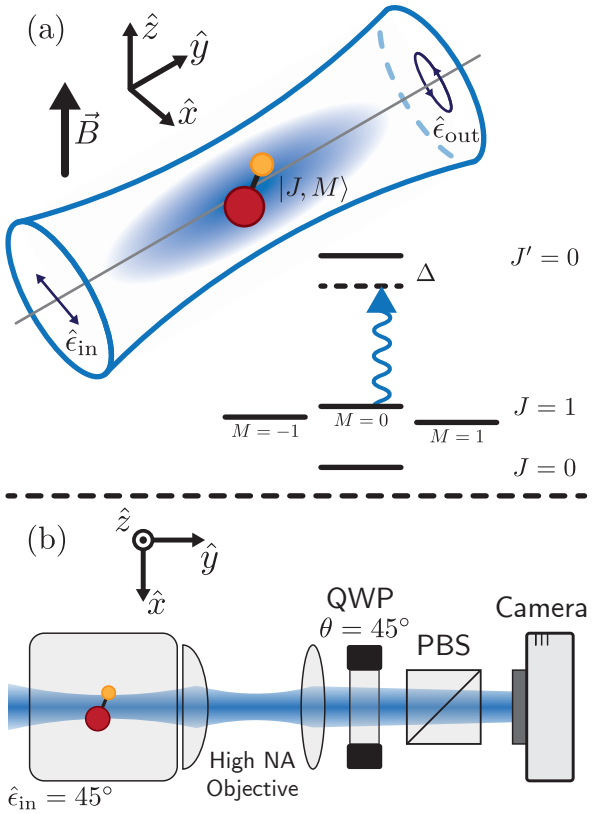

Figure 3.1: Schematic of dispersive imaging setup for molecules. **(a)** Molecules are illuminated by a probe beam propagating along the $\hat{y}$ direction, perpendicular to an external magnetic field $\vec{B}$ along the $\hat{z}$ direction. The $\hat{z}$ axis serves as the quantization axis. The probe laser polarization $\hat{\epsilon}_{\text{in}}$ is linear and in the x-z plane. The ellipticity of the output polarization $\hat{\epsilon}_{\text{out}}$ depends both on $\hat{\epsilon}_{\text{in}}$ and the rotational state $|J, M\rangle$ of the molecule(s). The probe beam in the perpendicular imaging case off-resonantly (with a frequency detuning of Δ) couples an excited rotational state with primarily $M = 0$ character to a $J' = 0$ excited electronic state, as displayed in the level diagram. **(b)** One possible experimental setup for perpendicular imaging. Light with linear polarization at 45° to the quantization axis acquires a differential phase shift through rotationally excited molecules. The light is collected by a high numerical aperture (NA) objective. The phase shift is translated to a polarization rotation via a quarter wave plate (QWP) with fast axis set at 45° from vertical. A polarizing beam splitter (PBS) turns the rotation into a power difference that is detected by a camera.

Figure 3.1(a) schematically shows an example of a polarization-based setup for the dispersive imaging of molecules. A probe laser propagates through a molecular cloud along the $\hat{y}$ axis perpendicular to a uniform magnetic field $\vec{B}$ applied along the $\hat{z}$ axis. We call this the "perpendicular" imaging scheme, in reference to the fact that the probe laser propagation and magnetic field direction are perpendicular. For bi-alkali molecules that are first associated from atoms into molecules by means of a sweep across a Feshbach resonance, the magnetic field strength B would typically be a few hundred Gauss, as determined by the Feshbach resonance. We consider the incident probe laser polarization $\hat{\epsilon}_{\text{in}}$ as being linear

and in the x-z plane. If both the molecular rotational state $|J, M\rangle$ has an anisotropic dynamic polarizability tensor $\alpha_{\epsilon\epsilon'}(\omega)$, for which the indices ϵ and ϵ' are x, y, or z in Cartesian coordinates, and $\hat{\epsilon}_{\text{in}}$ has a component both parallel and perpendicular to the quantization axis, then the output laser polarization $\hat{\epsilon}_{\text{out}}$ becomes elliptical. Here, the rotational quantum number J labels eigenstates of $\vec{J}$, the sum of the electronic and molecular-orbital angular momenta and M is the projection along the quantization axis. The phase difference $\phi(\omega)$ between the z- and x-components of the output laser beam is given by

$$\phi(\omega) = \frac{2\pi\rho cL}{\lambda}\Delta\alpha(\omega), \tag{3.1}$$

where λ is the photon wavelength of the probe laser of angular frequency ω, ρ is the number density of the molecules, L is the sample length, c is the speed of light in vacuum, and $\Delta\alpha(\omega) = \alpha_{zz}(\omega) - \alpha_{xx}(\omega)$ is the differential polarizability. Equation 3.1 assumes a low differential index of refraction: $\Delta n = \rho c\Delta\alpha \ll 1$. It is also important to note that α is actually a modified polarizability *volume*, where $\alpha = \alpha_{\text{SI}}/2\epsilon_0 c$, ϵ_0 is the vacuum permittivity, and α_{SI} is the polarizability in standard SI units. As will be conveniently used later in this paper, α/h, where h is Planck's constant, has units MHz/(W/cm^2), which is experimentally understood as the ac Stark shift at a given laser intensity. Equation 3.1 defines our key observable and therefore motivates evaluation of $\Delta\alpha(\omega)$. As we will see, large differential polarizability arises from anistropic states which we find in the $J = 1$ manifold depicted in Fig. 3.1(a).

Figure 3.1(b) shows a schematic of a proposed detection apparatus. After passing through the molecular sample, the phase difference of the two polarization components of the probe beam is translated to a polarization rotation by the use of a quarter wave plate. The rotation is then translated to a probe power difference by, *e.g.*, a polarizing beam splitter and a camera.

Alternative to this "perpendicular" probing scenario, the system can be probed using a linearly polarized laser beam propagating parallel to the magnetic field direction. This may be useful in certain contexts, *e.g.*, as in the case of planar 2D samples resolved by a quantum gas microscope. In this "parallel" imaging scheme, the phase shift is also given by

Eq. 3.1 with $\Delta\alpha = \alpha_{++}(\omega) - \alpha_{--}(\omega)$ where the indices "+" and "−" indicate spherical tensor components of the dynamic polarizability tensor. We note that for this case in which the molecular sample displays circular birefringence, optical activity leads to a direct rotation of the probe beam's linear polarization.

The efficiency of the perpendicular and parallel imaging schemes are comparable, yet the distinction is critical as the orientation of the probe laser and quantization axis will determine the relevant states that display the largest anisotropy. A detailed derivation of Eq. 3.1 for the two probing schemes is given in Appendix 3.9. In what follows we will focus primarily on the perpendicular imaging scheme in the main text and reserve the discussion of the parallel imaging scheme to Appendix 3.10.

A strong signal in an experimental setup will be induced by a large differential polarizability. For example, in a typical ultracold sample density of $\rho = 10^{12}\,\mathrm{cm}^{-3}$, probe wavelength $\lambda = 770\,\mathrm{nm}$, and a sample length $L = 30\,\mu\mathrm{m}$, the differential polarizability $\Delta\alpha/h$ must have a value of $3.6\,\mathrm{MHz}/(\mathrm{W/cm}^2)$ to achieve a phase difference of 1°. As we will discuss, these magnitudes of $\Delta\alpha$ can be found near resonant electric dipole transitions from anisotropic $J \neq 0$ rotational states of molecules. We note that even the $J = 0$ rotational ground state may have an induced anisotropic polarizability, if the degeneracy of the $J' = 1$ manifold's M states is broken by an amount that is large compared to their natural linewidth. For imaging on narrow transitions, this can be accomplished by the application of an electric field for polar molecules, and potentially even by state-dependent ac Stark shifts.

We expect our scheme to be generally applicable to molecular states with large anisotropies in dynamic polarizability. Such states should appear for generic families of molecules. To make quantitative estimates we focus on states of two specific bi-alkali molecules. In the text we focus on imaging $^{23}\mathrm{Na}^{87}\mathrm{Rb}$ molecules occupying the $J = 1$ rotational level of its $v = 0$ vibrational level of the electronic ground state $\mathrm{X}^1\Sigma^+$.

3.3 Selection of Imaging States

The optimal imaging states have a large differential polarizability. Since anistropy enhances differential polarizability, we search for states that are as anisotropic as possible. Specifically,

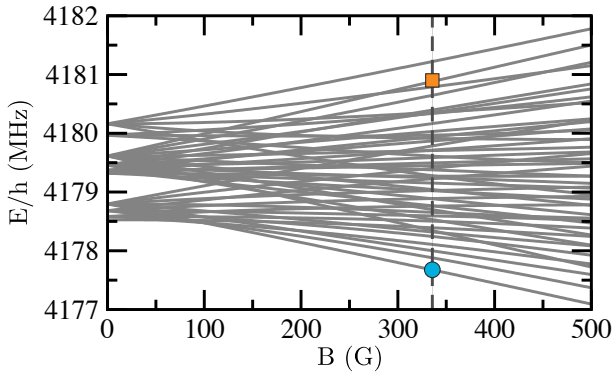

Figure 3.2: Eigenenergies of the hyperfine states of the $v = 0$, $J = 1$ ro-vibrational level of the $X^1\Sigma^+$ electronic ground state of $^{23}Na^{87}Rb$ as a function of magnetic field strength B. The dashed vertical line indicates the magnetic field strength $B = 335.6\,G$. The cyan dot and orange square mark states used for the perpendicular and parallel (Appendix 3.10) imaging schemes, respectively. The zero of energy of this plot relates to the zero-field ($B = 0$) energy of the $v = 0, J = 0$ level with no electron-nuclear quadrupole interaction.

we focus on the $J = 1$ rotational manifold, and we look for the state with the highest occupation of the $M = 0$ projection at the relevant magnetic field for the specific Feshbach resonance used in the molecule creation. For $^{23}Na^{87}Rb$ molecules occupying the $v = 0, J = 1$ ro-vibrational state of their electronic state $X^1\Sigma^+$ we are guided by recent work [46] using a magnetic field strength of 335.6 G. We will show that the best imaging state at this field also happens to be lowest in energy.

As depicted in Fig. 3.1(a), the $J = 1$ rotational state of the $v = 0$ ground-state molecule has three projections $M = -1, 0, +1$. The projection degeneracy is broken by hyperfine interactions between the two nuclear quadrupole moments and the rotation of the molecule as well as Zeeman interactions for the nuclear spins [66–68]. We denote the nuclear spins of ^{23}Na and ^{87}Rb by $\vec{\imath}_{Na}$ and $\vec{\imath}_{Rb}$, respectively. Both have quantum number, or value, of 3/2. Their projection quantum numbers along the magnetic field direction are m_{Na} and m_{Rb}, respectively. For all interactions the sum $M_{tot} = M + m_{Na} + m_{Rb}$ is a conserved quantity. We use the nuclear quadrupole moments and nuclear g factors from Refs. [46, 69]. Coupling to rotational states $J \neq 1$ is negligible as the rotational constant [70] is orders of magnitude larger than the energy scales of the hyperfine and Zeeman interactions.

There are 48 hyperfine-Zeeman eigenstates of the $v = 0$, $J = 1$ level of ground state $^{23}Na^{87}Rb$. In zero magnetic field the total angular momentum $\vec{F}_{tot} = \vec{J} + \vec{\imath}_{Na} + \vec{\imath}_{Rb}$ is conserved

and states can also be labeled by $F_{\rm tot}$ as well as $M_{\rm tot}$. For magnetic field strengths larger than about 100 G the nuclear Zeeman interaction is stronger than the hyperfine interactions and states with the same $M_{\rm tot}$ avoid each other. There, the energetically lowest $J = 1$ state has $M_{\rm tot} = +3$. For B fields not exceeding 500 G the 48 levels span an energy range of no more than $h \times 5\,\mathrm{MHz}$. Fig. 3.2 plots the relevant eigenenergies.

For perpendicular dispersive imaging we investigate the lowest energy state depicted in Fig. 3.2 (cyan dot). We check that the hyperfine state has a relatively high component of the projection quantum number $M = 0$ and relatively small contribution of other M projections. Our calculations show that the energetically lowest $J = 1$ level has the largest $M = 0$ contribution and to very good approximation is described by the superposition

$$\begin{aligned} |\varphi_{\rm perp}\rangle \;\; = \;\; & c_0 \left| \mathrm{X}^1\Sigma^+; \begin{array}{c} v=0, J=1, M=0 \\ m_{\rm Na}=3/2, m_{\rm Rb}=3/2 \end{array} \right\rangle \\ & + \; c_1 \left| \mathrm{X}^1\Sigma^+; \begin{array}{c} v=0, J=1, M=1 \\ m_{\rm Na}=3/2, m_{\rm Rb}=1/2 \end{array} \right\rangle \end{aligned} \tag{3.2}$$

with coefficient $c_0 = 0.892$ and $c_1 = 0.452$. We will therefore proceed with this state as the imaging state.

3.4 Selection of target excited states

3.4.1 Selection Criteria and Relevant Quantities

We aim to select target excited states that satisfy three criteria. First and foremost the dynamic polarizabilty should display a large anisotropy near the resonance transition to the target excited state. This will ensure detectability via large phase differences in Eq. 3.1 for our imaging state, $|\varphi_{\rm perp}\rangle$. Secondly, the target state, $|\psi_{\rm t}\rangle$, should have a small natural linewidth in order to minimize heating, particle loss, and dephasing. We also impose a third criteria as a matter of practical experimental concern. We additionally search for a target state where the transition has as large a transition width as possible, thus allowing for easier laser stabilization as well as more robust operation. This section defines the quantities we need: the natural linewidth, dynamical polarizability and photon scattering rate, to search

for useful target excited states based on the above criteria.

We first consider the natural linewidth, $\gamma_{\rm n}$, of the target state [71, 72]:

$$\gamma_{\rm n} = \frac{4}{3}\frac{1}{4\pi\epsilon_0\hbar c^3}\sum_{g\vec{\epsilon}}\omega_{\text{t-}g}^3|\langle\psi_{\rm t}|d_{t\leftarrow g}(R)\hat{R}\cdot\vec{\epsilon}|\varphi_g\rangle|^2\,. \tag{3.3}$$

Here the sum of $\vec{\epsilon}$ is over the polarization direction of the spontaneously emitted photon and the summation g for hetero-nuclear alkali-metal dimers is over all eigenstates $|\varphi_g\rangle$, both bound and scattering states, with energy E_g of the $X^1\Sigma^+$ and $a^3\Sigma^+$ potentials. Both potentials dissociate to atoms in the electronic ground state. The transition energy reads $\hbar\omega_{\text{t-}g} = E_{\rm t} - E_g$, where $E_{\rm t}$ is the energy of the target state. The quantity $d_{t\leftarrow g}(R)$ is the R-dependent transition electric dipole moment operator, where R is the interatomic separation. The interatomic axis has orientation $\hat{R}$.

We find it convenient to define the orientation-dependent "transition widths" $\Gamma_{\epsilon\epsilon}$ for transitions between the imaging state $|\varphi_{\rm perp}\rangle$ and target state $|\psi_{\rm t}\rangle$ using probe polarization $\vec{\epsilon}$ as:

$$\Gamma_{\epsilon\epsilon} \;=\; \frac{4}{3}\frac{1}{4\pi\epsilon_0\hbar c^3}\omega_{\text{t-im}}^3|\langle\psi_{\rm t}|d_{t\leftarrow g}(R)\hat{R}\cdot\vec{\epsilon}|\varphi_{\rm perp}\rangle|^2. \tag{3.4}$$

Here, $\hbar\omega_{\text{t-im}} = E_{\rm t} - E_{\rm im}$ and $E_{\rm im}$ is the eigenenergy of the imaging state. Since the imaging state $|\varphi_{\rm perp}\rangle$ is a bound state of the $X^1\Sigma^+$ potential, it is thus included in the sum over states in Eq. 3.3. All else held equal, target states with as large a value of $\Gamma_{\epsilon\epsilon}$ as possible may be practically desirable, as transitions to these states will be less sensitive to laser noise and technical variations of the state energies.

To highlight the anisotropy in $\Gamma_{\epsilon\epsilon}$ we define the differential transition width:

$$\Gamma = \Gamma_{zz} - \Gamma_{xx} \tag{3.5}$$

for $\Delta\alpha(\omega)$. We argue (See Appendix 3.9) that for our particular choice of target excited states, Γ fully captures the anisotropy. For the n'-th ro-vibrational target states we use here,

$|\psi_{\mathrm{t},n'}\rangle$, we find (See Appendix 3.9):

$$\Gamma = \frac{4}{3}\frac{1}{4\pi\epsilon_0\hbar c^3}\left(\frac{|c_0|^2}{3} - \frac{|c_1|^2}{6}\right)\omega_{\text{t-im}}^3|\mu_{n'}|^2\,, \tag{3.6}$$

where the vibrational matrix elements $\mu_{n'}$ depend on the target state and are defined explicitly in Appendix 3.9. Here $n' = 0, 1, 2, ...$ is used to label the eigenstates by order of their eigenenergies.

We now turn to the dynamic polarizability. The dynamic polarizability tensor components $\alpha_{\epsilon\epsilon}(\omega)$ of the imaging state $|\varphi_{\text{perp}}\rangle$ at probe frequency ω are determined by a sum over ro-vibrational levels and scattering states of all electronic states. For frequencies close to the target state resonance, such that $\omega \approx \omega_{\text{t-im}}$ but $|\omega - \omega_{\text{t-im}}| \gg \gamma_n$, the polarizability can be described as

$$\alpha_{\epsilon\epsilon}(\omega) \;\; = \;\; -\frac{3\pi}{2}\frac{c^2}{\omega_{\text{t-im}}^3}\frac{\Gamma_{\epsilon\epsilon}}{\Delta} + \alpha_{\epsilon\epsilon}^{(0)}, \tag{3.7}$$

where $\Delta = \omega - \omega_{\text{t-im}}$ is the probe laser detuning. The background polarizability $\alpha_{\epsilon\epsilon}^{(0)}$ contains the contributions from all other far-detuned molecular states and for our purposes can be taken as independent of ω. We note that a similar background contribution to the polarizability anisotropy, $\Delta\alpha(\omega)$, can also be defined. This background anisotropy is several orders of magnitude smaller than the MHz/(W/cm^2)-level contributions we consider near resonance, and in practice can be safely neglected. We seek to find states where the difference of two components of this polarizability tensor, $|\alpha_{zz} - \alpha_{xx}|$, is maximized for a fixed detuning. Such an anisotropy can be achieved by looking for transitions with significant angular dependence of $\Gamma_{\epsilon\epsilon}$.

Finally, we will also compute the photon scattering rate to estimate heating and loss of coherence near a resonance. For $|\Delta| \gg \gamma_{\text{n}}$ it is given by:

$$\gamma_{\text{sc}} = \sum_{\epsilon\epsilon}\left(\frac{3\pi}{4}\frac{c^2}{\omega_{\text{t-im}}^3}\frac{\Gamma_{\epsilon\epsilon}\gamma_{\text{n}}}{\Delta^2} + \beta_{\text{sc}}^{(0)}\right) \times I\;, \tag{3.8}$$

where I is the probe laser intensity and $\beta_{\text{sc}}^{(0)}$ the background imaginary polarizability. Mini-

mal values of γ_{sc} are ideal to avoid heating and scattering loss into dark states.

3.4.2 Target Excited States for $^{23}Na^{87}Rb$

In this section we will show that starting from the imaging state (a hyperfine state of the $v = 0, J = 1$ ro-vibrational level of the $X^1\Sigma^+$ state) we can use optical wavelengths to access mixed $J' = 0$ ro-vibrational states of the coupled $A^1\Sigma^+$-$b^3\Pi_0$ complex. We will show by direct calculation that these states satisfy the criteria discussed in Sec. 3.4.1.

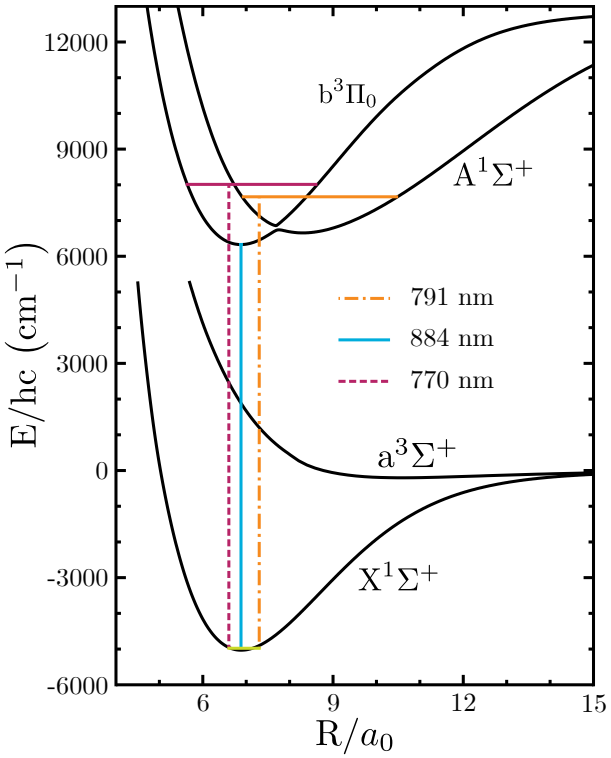

Figure 3.3: Ground and relevant excited adiabatic relativistic potentials of the $^{23}Na^{87}Rb$ molecule as functions of atom-atom separation R. The two energetically lowest adiabatic potentials are identified by non-relativistic labels $X^1\Sigma^+$ and $a^3\Sigma^+$ respectively. The zero of energy of the graph is set at their dissociated limit. The two remaining excited adiabatic potentials have a narrow avoided crossing at $R_c \approx 7.5a_0$. For $R > R_c$ the electronic wavefunctions of the third and fourth adiabat are well described by the non-relativistic $A^1\Sigma^+$ and $b^3\Pi_0$ symmetry, respectively. For $R < R_c$ this assignment is inverted. The three vertical lines indicate transitions from the $v = 0, J = 1$ imaging state in the $X^1\Sigma^+$ state to three mixed $J' = 0$ ro-vibrational states of the coupled $A^1\Sigma^+$-$b^3\Pi_0$ complex. The transition wavelengths are 770 nm, 791 nm, and 884 nm for the magenta, orange, and cyan lines, respectively. The magnetic field is $B = 335.6$ G.

We now present results for our exhaustive search for useful target states. Fig. 3.3 effectively summarizes the findings of this section by plotting the transition to the relevant target states against the molecular potential. The details in obtaining these target states can be

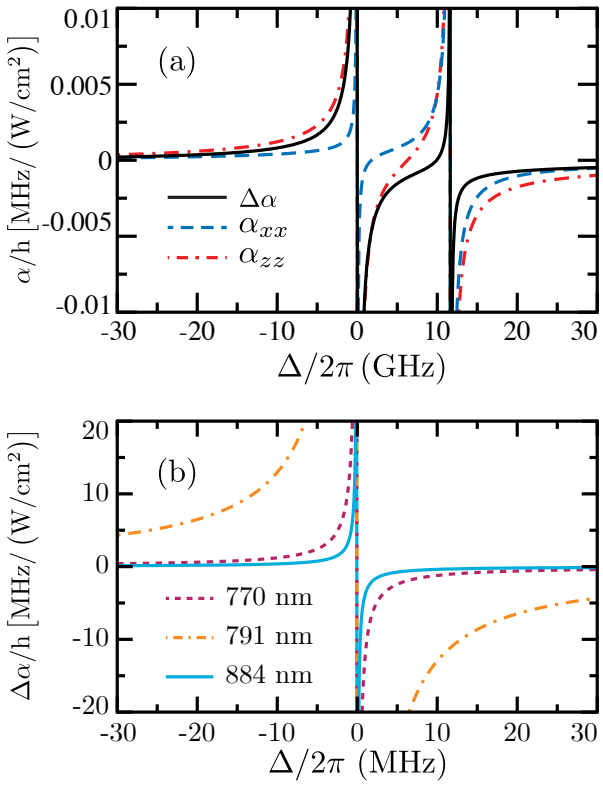

Figure 3.4: **(a)** Values of α_{xx}, α_{zz}, and $\Delta\alpha$ for a large range of detunings of the 770 nm transition from the ground $v = 0, J = 1$ $X^1\Sigma^+$ imaging state $|\varphi_{\text{perp}}\rangle$. The second resonance at roughly 12 GHz corresponds to transitions to the $J' = 2$ states. **(b)** Differential dynamic polarizabilities $\Delta\alpha$ as a function of frequency detuning Δ to the target states for the 770 nm, 791 nm, and 884 nm transitions of $^{23}Na^{87}Rb$ identified in Fig. 3.3. The magnetic field in both graphs is 335.6 G.

found in Appendix 3.8. Our search led to a focus on three states highlighted in Fig. 3.3. To select target states that are convenient for imaging we have computed the natural linewidth and differential transition width for all eigenstates of the $J' = 0$ $A^1\Sigma^+$-$b^3\Pi_0$ system. The lowest energy excited level is to the $n' = 0$ eigenstate. It has a 99.75 % admixture $a_{b,n'=0}$ in the $|b^3\Pi_0\rangle$ state. A transition from an imaging state to this target state has a wavelength of 884 nm. The transition from our imaging state to the $n' = 29$ target eigenstate has a wavelength of 791 nm. This target state has a 96.85 % admixture in the $|A^1\Sigma^+\rangle$ state. Finally, the 770 nm transition is to the $n' = 39$ eigenstate. This target state has a 94.65 % admixture in the $|b^3\Pi_0\rangle$ state and was used in Ref. [46] as the intermediate state in the STIRAP process to form $^{23}Na^{87}Rb$ molecules in their absolute ground state.

Figure 3.4(a) shows the components of the differential dynamic polarizability of $|\varphi_{\text{perp}}\rangle$ for the 770 nm transition as a function of detuning Δ. Visible are the poles of both a $J' = 0$

and $J' = 2$ transition. Since the state $|\varphi_{\text{perp}}\rangle$ has an 80 % and 20 % population in the $M = 0$ and $M = 1$ components, respectively, the transition width Γ_{xx} of $\alpha_{xx}(\omega)$ is much smaller than the corresponding width of $\alpha_{zz}(\omega)$. Due to these unbalanced populations, the differential transition width Γ is positive for negative detuning, hence the differential dynamic polarizability $\Delta\alpha$. On the vertical scale of the figure the background contribution $\Delta\alpha^{(0)}$ to $\Delta\alpha(\omega)$ is negligible. Narrowing in on the $J' = 0$ transition, we summarize in Fig. 3.4(b) the results for $\Delta\alpha$ for the 770 nm, 791 nm, and 884 nm transitions. Here we see the resonant transition near 791 nm to target state $n' = 29$ with its large $A^1\Sigma^+$ admixture has the largest differential transition width Γ by far. This is a consequence of the large transition dipole moment between the $X^1\Sigma^+$ and $A^1\Sigma^+$ states. Naively, this suggests that this transition is the best of the three candidate transitions for perpendicular imaging. We, however, must also account for spontaneous emission and, in particular, whether the photon scattering rate γ_{sc} is minimized.

To look for the transition with the best balance between large transition width and small photon scattering rate, we have additionally determined $\Delta\alpha(\omega)$ for $|\varphi_{\text{perp}}\rangle$ as a function of ω near transitions to many of the $J' = 0$ eigenstates of the $A^1\Sigma^+$-$b^3\Pi_0$ complex. We have also computed the natural linewidths and differential transition widths, γ_{n} and Γ, of these target states. Fig. 3.5 shows widths γ_{n} and Γ as well as the ratio γ_{n}/Γ for the first 66 $J' = 0$ eigenstates of the $A^1\Sigma^+$-$b^3\Pi_0$ complex. The colored markers in each panel correspond to the three transitions shown in Figs. 3.3 and 3.4(b). The left-most four points with the smallest transition energy correspond to transitions to the bound states at the bottom of the $b^3\Pi_0$ potential.

Figure 3.5(a) shows that the natural linewidths γ_{n} group roughly into three bands: those with values smaller than $2\pi\times2$ MHz, those with values larger than $2\pi\times5$ MHz, and those in between. The first corresponds to transitions to target states with a dominant admixture of the $|b^3\Pi_0\rangle$ state and thus would have been forbidden without spin-orbit coupling between the $A^1\Sigma^+$ and $b^3\Pi_0$ states. The second group corresponds to transitions to target states with a dominant admixture in the $A^1\Sigma^+$ state leading to the largest γ_{n}. Finally, the scattered points between these two bands correspond to target states with almost equal admixture of $b^3\Pi_0$ and $A^1\Sigma^+$ components. The natural linewidths for the 884 nm, 791 nm, and 770 nm transitions

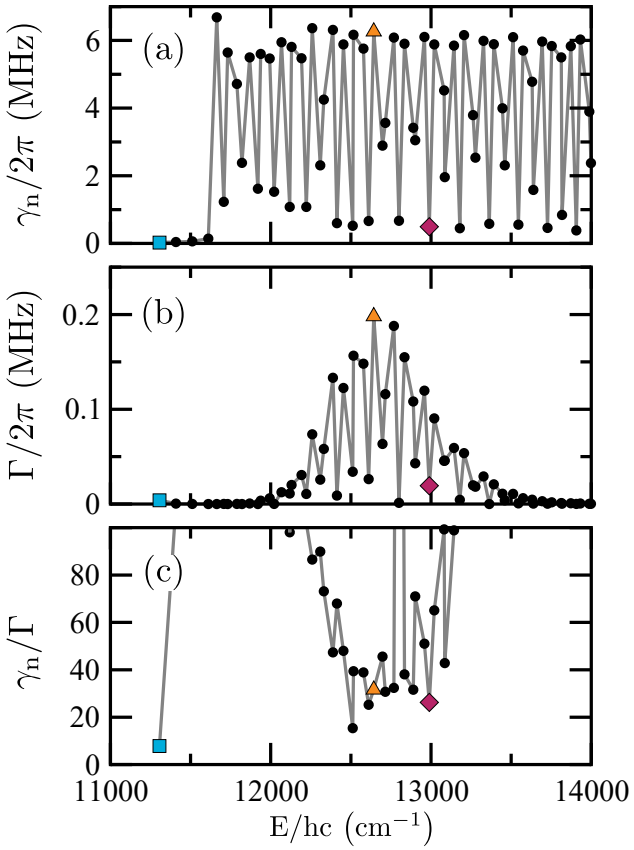

Figure 3.5: The natural linewidth γ_n **(a)** of eigenstates of the $J' = 0$ $A^1\Sigma^+$-$b^3\Pi_0$ complex of $^{23}Na^{87}Rb$ and their differential transition width Γ **(b)** from the ground $v = 0, J = 1$ $X^1\Sigma^+$ imaging state $|\varphi_{perp}\rangle$ for perpendicular imaging as functions of transition energy E. The transition energies are relative to the energy of $|\varphi_{perp}\rangle$. **(c)** The ratio γ_n/Γ as a function of transition energy. The cyan square, orange triangle, and magenta diamond correspond to the transitions shown in Fig. 3.3 featuring transition wavelengths of 884 nm, 791 nm, and 770 nm, respectively. The values of γ_n/Γ for the cyan square, the orange triangle, and the magenta diamond are 7.8, 32, and 26, respectively. The magnetic field in all graphs is 335.6 G.

are calculated to be $2\pi\times0.027$ MHz, $2\pi\times6.3$ MHz, and $2\pi\times0.50$ MHz, respectively.

Figure 3.5(b) shows the differential transition widths Γ. Their values are positive, oscillate with transition energy, and have a Gaussian envelope. For a transition with larger Γ, we have a larger absolute range of detunings in which the differential polarizability can reach the desired magnitude. In fact, Γ is largest when the target state has a large $A^1\Sigma^+$ admixture and the vibrational matrix element $\mu_{n'}$ is large. The latter occurs when the inner turning point of the vibrational motion on the $A^1\Sigma^+$ potential coincides with the equilibrium separation of the $X^1\Sigma^+$ potential. The 791 nm transition to the $n' = 29$ $A^1\Sigma^+$-$b^3\Pi_0$ eigenstate, already discussed in the context of Figs. 3.3 and 3.4(b), has the largest Γ. Finally, we observe that the differential transition widths for the 884 nm, 791 nm, and 770 nm, transitions are

$2\pi\times4.0\,\mathrm{kHz}$, $2\pi\times190\,\mathrm{kHz}$, and $2\pi\times19\,\mathrm{kHz}$, respectively.

Figure 3.5(c) shows the ratio γ_n/Γ as a function of transition energy from the $|\varphi_\mathrm{perp}\rangle$ state. This quantity gives insight to the "verticality" of the transition, wherein smaller ratios correspond to the fewest decay paths available to the targeted excited state. For example, for a target state that can only spontaneously decay to the ground state (same electronic, vibrational, and hyperfine levels as the imaging state), we find the lower bound for this ratio is

$$\frac{\gamma_\mathrm{n}}{\Gamma} = \frac{3}{|c_0|^2 - |c_1|^2/2}. \tag{3.9}$$

For the state $|\varphi_\mathrm{perp}\rangle$, this limiting ratio is 4.3. A lower bound ratio of 3 is found in the ideal case of a pure $|J=1,0\rangle$ state for perpendicular imaging, limited by the $J'=0$ target state's ability to decay to any of the three M states of the $J=1$ manifold. Transitions that realize this lower bound are known as vertical transitions. For the case of a $J=0$ imaging state with anisotropic polarizability induced by, *e.g.*, an applied electric field, the lower bound ratio for vertical transitions is also equal to 3, due to the dipole-allowed decay paths to $J=0$ and 2 states.

The ratio γ_n/Γ is larger than 10 for all transitions to $J'=0$ $\mathrm{A}^1\Sigma^+$-$\mathrm{b}^3\Pi_0$ eigenstates except for the $n'=0$ eigenstate, where its value is 7.8. Thus this 884 nm transition is closest to vertical. For all the transitions, the excited state does not only spontaneously decay to the imaging state but also to other ro-vibrational states of the $\mathrm{X}^1\Sigma^+$ potential as well as those of the $\mathrm{a}^3\Sigma^+$ potential. The most typical value for γ_n/Γ is between 20 and 40. Lastly, we calculate γ_n/Γ values of 32 and 26 for the 791 nm and 770 nm transitions, respectively. We note that these values are all reduced by a factor of 1.44 for the case of parallel imaging.

The next section summarizes how these results for γ_n/Γ and γ_{sc} relate to an interplay and trade-off with respect to maintaining low inelastic scattering rates and allowing for robust operation.

3.5 Summary of perpendicular imaging conditions for bulk gases

We have shown that polar molecules prepared in rotationally excited states can act as an anisotropic medium, resulting in birefringent phase shifts on an off-resonant probe laser field. Furthermore, our calculations show that these phase shifts are large enough to be detectable. For the three transitions identified in ^{23}Na^{87}Rb in the previous section, we summarize in Table 3.1 the detuning, in units of the respective transition linewidth, necessary to achieve a birefringent phase shift $\varphi_{\text{bulk}} = 1^\circ$ and the resulting inelastic loss rate γ_{sc}. Because the ratios of the natural linewidth to the transition linewidth, γ_{n}/Γ, differ for the various excited states considered, we see a range of detunings that are necessary to attain the 1° polarization rotation. Here, we have considered typical density values, $\rho = 10^{12}\,\text{cm}^{-3}$, for molecular gases formed from pre-cooled atoms [13, 73], and a sample length L equal to $30\,\mu$m (long, but readily achievable for single-beam trapping). For the inelastic loss rates presented in Table 3.1, we have considered a probe beam intensity of $0.02\,\text{mW/cm}^2$ (relating to the peak probe intensity for a beam with $50\,\mu$W of power and a 1 inch diameter).

Wavelength	$1^\circ\,\Delta\,(\Gamma)$	$1^\circ\,\Delta/2\pi$ (MHz)	γ_{n}/Γ	$\gamma_{\text{sc}}/2\pi$ (Hz)
884 nm	159	0.64	7.8	4.08
791 nm	134	25.43	32	16.91
770 nm	124	2.35	26	14.85

Table 3.1: Summary of relevant quantities for the three chosen transitions of the $A^1\Sigma^+$-$b^3\Pi_0$ system of ^{23}Na^{87}Rb. The first column gives the transition wavelength. The second and third columns give the detuning, in units of transition linewidths and MHz, respectively, necessary to attain a 1° polarization rotation on a molecular sample of density $10^{12}\,\text{cm}^{-3}$ and a sample length of $30\,\mu$m. The fourth column shows the ratio of the natural linewidth to the differential transition width. The last column is the inelastic scattering rate γ_{sc} when achieving 1° rotations for a probe intensity of $0.02\,\text{mW/cm}^2$. All quantities relate to the case of "perpendicular" imaging. In the case of "parallel" imaging, γ_n/Γ is reduced by a factor of 1.44 and the inelastic scattering rate γ_{sc} is reduced by a factor of 1.87 for an equivalent rotation angle ϕ.

In the previous section, advantages of choosing the target states corresponding to the 791 nm and 884 nm transitions were briefly discussed. The 791 nm transition is the strongest yet it maintains a reasonably small γ_{n}/Γ ratio. These work to keep the inelastic scattering rate low while reducing the amount of laser stability needed to maintain a particular value of detuning (in units of Γ). The 884 nm transition, albeit much weaker, has the lowest γ_{n}/Γ

ratio at 7.8 and is therefore subject to the smallest amount of imaging induced heating [1]. Because of the narrow differential transition width of 884 nm transition, its requirements for laser stabilization and its sensitivity to noise and drifts of the state energies will be more pronounced. However, because this dispersive imaging scheme can be operated dozens or hundreds of differential transition widths away from resonance, it is in general rather insensitive to such frequency variations.

The 770 nm transition sits at a compromise, in both transition strength and γ_n/Γ ratio, between the 791 and 884 nm transitions. The primary benefit is that experiments with ground state ^{23}Na^{87}Rb will necessarily have the laser stabilization infrastructure for this wavelength in place, as it is used in the production of ground state molecules by STIRAP. As the STIRAP "dump" (Stokes) laser is typically fixed to the $J = 0 \rightarrow J' = 1$ transition frequency by locking to a cavity by the Pound-Drever-Hall (PDH) method, a stable imaging beam detuned by Δ from the $J = 1 \rightarrow J' = 0$ transition may easily be engineered without the need for an additional stabilized laser. This could be accommodated by using acousto-optic modulators to introduce GHz-level frequency shifts ($2B \pm \Delta \sim h \times 4$ GHz for ^{23}Na^{87}Rb), or by dynamically changing the frequency offset used for PDH sideband locking (in the case that a broadband fiber electro-optic modulator can be utilized) prior to imaging. Given the availability of suitable imaging light in ^{23}Na^{87}Rb experiments [46], the realization of nondestructive dispersive imaging of ^{23}Na^{87}Rb molecular gases should be imminently achievable. If similar conditions also exist for other molecules, as may be expected, then this nondestructive technique would be readily applicable in many existing cold molecule experiments.

3.6 Imaging Single Molecules

A natural and impactful extension of this imaging scheme would be to enable the resolution of individually trapped molecules [10, 12, 74]. For an individual point-like scatterer, such as a single molecule tightly confined to a lattice site or optical tweezer, the peak polarization

[1] For each of the identified transitions for ^{23}Na^{87}Rb, if one considers the parallel imaging scheme as compared to perpendicular imaging, the ratio of γ_n/Γ is lower by a factor of 1.44 and the inelastic scattering rate γ_{sc} at an equivalent rotation angle ϕ is lower by a factor of 1.87

rotation will be smaller than the values we have discussed for bulk molecular gases. This is because individual molecules will have a maximum effective optical density (OD), while the signal from a bulk gas can be boosted by the collective, integrated contribution of many molecules along the imaging direction. To compensate for this loss of collective OD enhancement, operation closer to resonance is required to attain degree-level rotations from single molecules. Furthermore, as discussed in Ref. [62], a high numerical aperture imaging system is required to enable the detection of individual particles.

We first consider the achievable polarization rotation signal under the most ideal conditions: utilizing a state-of-the-art imaging system with an NA of 0.8 [75] and operating on the more vertical 884 nm transition. We additionally consider the case of "parallel" imaging, which reduces the amount of inelastic scattering by roughly a factor of two for the equivalent rotation signal. At a detuning of $\Delta = 19\,\Gamma$, a point-like scatterer would result in a peak polarization rotation of $\phi \approx 1.52°$. While this degree of rotation is comparable to what has been used to detect single atoms [62], one also has to account for how much scattering can be tolerated for the molecules. For an imaging intensity of $I = 0.02\,\mathrm{mW/cm^2}$, as was considered in Table 3.1, this would result in an inelastic scattering rate of 152 Hz.

We can restrict to an imaging time τ such that only one inelastic scattering event occurs and the molecule interacts with $N_p \approx I\tau\sigma/hf$ probe photons, where $\sigma \approx \lambda^2/\pi$ is the off-resonant scattering cross-section for imaging light of wavelength λ (frequency f). With this restriction, one finds that the maximum achievable signal-to-noise ratio (SNR) for shot-noise-limited performance, $\mathrm{SNR}_{max} = \phi\sqrt{\eta N_p}$ [76], just barely exceeds 1 even if we assume a perfect efficiency η for collection and detection. Under realistic conditions, the actual SNR will be reduced due to additional noise, reduced efficiency, by the use of imaging systems with more modest NA, and potentially by use of the "perpendicular" scheme or more lossy imaging transitions.

To achieve the high SNRs necessary for high-fidelity detection, this dispersive imaging technique would thus have to be combined with, *e.g.*, enhancement by a high-finesse optical cavity [77, 78] or by the addition of repumping lasers, which would enable more scattering events prior to the loss of population to dark states [79]. In the latter case, repumping in a way that is commensurate with polarization-based dispersive imaging could be achieved by

using $J = 0$ ground state molecules. Dispersive imaging on narrow, nearly vertical transitions [79, 80] could be enabled by the application of an electric field or optical fields, thereby breaking the degeneracy of the $J' = 1$ sublevels and inducing an anisotropic polarizability.

3.7 Discussion

In this paper we have presented a nondestructive technique for imaging excited rotational states of ultracold molecules using well known techniques from the toolbox of ultracold atoms. We described the anisotropic nature of excited rotational states and detailed how this can be translated to a measurable polarization rotation of a low intensity probe beam. For ^{23}Na^{87}Rb we identified electronic transitions one might use to image the first rotational excited state and presented expected polarization rotations for conditions in the current state-of-the-art ultracold molecule experiments.

These capabilities will be especially important for systems that lack alternative detection schemes based on optical cycling transitions, such as hetero-nuclear bi-alkalis and homo-nuclear alkali dimers. The nondestructive nature of the proposed imaging method for bulk gases is well-suited to applications in the study of cold chemistry. For instance, the continuous monitoring of a single sample of molecules may allow for the study of losses by chemical reaction [81], while avoiding sensitivity to shot-to-shot variations in the number of molecules produced.

Through the incorporation of cavity-based enhancement of dispersive signals, the discussed approach has potential to impact fundamental physics, such as in the search for bosonic dark matter particles [82]. One could continuously monitor molecular samples prepared in a "dark" rotational states that gives rise to no polarization rotation signal, looking for events in which population jumps to "bright" rotational states that yield a polarization rotation signal. Dispersive measurements aided by cavity enhancement could be utilized for measurement-based [78, 83–85] and coherent [78, 86] generation of squeezing of molecular rotation, which could then be transferred to alternate degrees of freedom to enable applications relevant to fundamental physics [15, 87, 88].

The extension of the proposed approach to the detection of individual molecules could

be enabled either by cavity enhancement of the dispersive phase shift or by the addition of one or more repump lasers when utilizing narrow, "vertical" imaging transitions. These ideas are not fully developed as of yet and will require future studies. Such an extension would be of critical importance for QIS applications in fiducial state preparation [89, 90] and qubit readout. Furthermore, this technique could enable effective quantum state preparation and high-fidelity detection in molecules, strengthening the relevance of molecules for use in quantum analog simulation [91, 92] and precision measurement [93, 94].

3.8 Paper Appendix I: Calculation of the Eigenstates of the $A^1\Sigma^+$-$b^3\Pi_0$ System

To calculate the dynamic polarizabilities $\alpha_{zz}(\omega)$ and $\alpha_{xx}(\omega)$, we sum up contributions from the ro-vibrational and scattering states of ground and excited electronic states using the approach developed in Ref. [95]. For the strongly coupled $A^1\Sigma^+$-$b^3\Pi_0$ system we rely on the electronic potentials surfaces, transition dipole moments, and spin-orbit coupling functions of Ref. [96]. The relevant R-dependent electric transition dipole moments $d_{f\leftarrow i}(R)$ between the pairs $(i, f) = (X^1\Sigma^+, A^1\Sigma^+)$ and $(i, f) = (a^3\Sigma^+, b^3\Pi)$ have been taken from Refs. [96, 97]. Transitions between the pairs $X^1\Sigma^+$-$b^3\Pi$ and $a^3\Sigma^+$-$A^1\Sigma^+$ of non-relativistic states are dipole forbidden. Moreover, the electric dipole moment operator only couples basis states with the same nuclear spin projection quantum numbers. For distant non-resonant electronic states, not shown in Fig. 3.3, we use the potentials and transition dipole moments of Ref. [72].

In this work, we are interested in the dynamic polarizabilities and the photon scattering rate near the resonance transitions to $J' = 0$ target states of the $A^1\Sigma^+$-$b^3\Pi_0$ system. The rotational states with $J' = 0$ only exist for electronic states with projection quantum number $\Omega^\sigma = 0^\pm$, where Ω is the projection of the total electron spin and angular momentum on the internuclear axis and $\sigma = \pm$ denotes a reflection symmetry. In alkali-metal dimers only $\Omega' = 0^+$ states can be excited from the $X^1\Sigma^+$ ground state. To further specify the target state we assembled the relevant 0^+ potentials of $^{23}Na^{87}Rb$ from Refs. [96, 98]. Fig. 3.3 shows the $X^1\Sigma^+$ potential and the energetically lowest two $\Omega' = 0^+$ relativistic potentials dissociating

to atom pair states with one atom electronically excited. The latter two potentials have been obtained by diagonalizing at each R a 2×2 potential matrix containing the non-relativistic $A^1\Sigma^+$ and $b^3\Pi$ electronic potentials coupled and shifted by an R-dependent relativistic spin-orbit interaction. For completeness, Fig. 3.3 also shows the $a^3\Sigma^+$ potential from Ref. [98] as the $b^3\Pi_0$ state can decay into this state by spontaneous emission. This process contributes to γ_n, the natural linewidth.

The couplings in the $J' = 0$ $A^1\Sigma^+$-$b^3\Pi_0$ system are sufficiently strong such that a quantitative representation of the molecular vibration requires a coupled-channel calculation starting from the non-relativistic basis of $|A^1\Sigma^+\rangle$ and $|b^3\Pi_0\rangle$ states, their potentials, and spin-orbit induced coupling. The normalized $J' = 0$ target vibrational wavefunctions are given by

$$|\psi_{t,n'}\rangle = \frac{1}{\sqrt{4\pi}} \left(f_{A,n'}(R)|A^1\Sigma^+\rangle + f_{b,n'}(R)|b^3\Pi_0\rangle \right) \times |i_{Na} m'_{Na}\rangle |i_{Rb} m'_{Rb}\rangle \,, \tag{3.10}$$

where the functions $f_{A,n'}(R)$ and $f_{b,n'}(R)$ are obtained from the coupled-channel calculation and index $n' = 0, 1, 2, \ldots$ labels eigenstates by order of their eigenenergies. For $J' = 0$ states the nuclear spin wavefunction is separable from that of the electrons and molecular rotation. The energy of two energetically nearest neighbor states with different m'_{Na} and m'_{Rb} are spaced by the nuclear Zeeman interaction and of order $h \times 0.1\,\mathrm{MHz}$ for our magnetic field strength. The quantities $a_{s,n'} = \int_0^\infty r^2 dr |f_{s,n'}(R)|^2$ are the admixtures of eigenstate n' in electronic components $s = A$ or B. For ease of notation we suppress the rotational and nuclear spin quantum numbers in denoting target states $|\psi_{t,n'}\rangle$. Effects of Coriolis-induced coupling to ro-vibrational levels of $\Omega' = 0^-$, 1, and 2 potentials of the $b^3\Pi$ state are negligible for our purposes.

3.9 Paper Appendix II: Derivation of Differential Transition Width

In this section we argue that Eqs. 3.5-3.6 offer a good approximation to the differential transition width Γ. First we note that the superposition of nuclear spin states in $|\varphi_{perp}\rangle$ in

Eq. 3.2 leads to contributions to $\Delta\alpha(\omega)$ from two nearly-degenerate target states with the same state label n' and quantum number $J' = 0$ and $M' = 0$, but different nuclear spin projections m'_{Rb} of ^{87}Rb. At $B = 335.6\,\mathrm{G}$ these two target states are split by $h\times 0.1\,\mathrm{MHz}$. We find that the value is on the order of or smaller than the natural linewidth of eigenstates of the $\mathrm{A}^1\Sigma^+$-$\mathrm{b}^3\Pi_0$ complex. In fact, as the superposition of states in $|\varphi_{\mathrm{perp}}\rangle$ also corresponds to a superposition of states with different rotational projection quantum numbers M, the $M = 0$ component contributes to $\alpha_{zz}(\omega)$ and the $M = 1$ component to $\alpha_{xx}(\omega)$. Then for detunings $|\Delta| \gg \gamma_n$, we can neglect the $h \times 0.1\,\mathrm{MHz}$ energy difference and define the differential transition width as in Eq. 3.5. Then for the n'-th $J' = 0$ ro-vibrational target state $|\psi_{\mathrm{t},n'}\rangle$ of the $\mathrm{A}^1\Sigma^+$-$\mathrm{b}^3\Pi_0$ system, we arrive at Eq. 3.6, where the vibrational matrix element is:

$$\mu_{n'} = \int_0^\infty R^2 \mathrm{d}R\, f_{\mathrm{A},n'}(R) d_{A\leftarrow X}(R) \varphi_{\mathrm{perp}}(R) \tag{3.11}$$

and $f_{\mathrm{A},n'}(R)$ and $\varphi_{\mathrm{perp}}(R)$ the radial wavefunction of the $\mathrm{A}^1\Sigma^+$ component of $|\psi_{\mathrm{t},n'}\rangle$ and the radial wavefunction of the imaging state $|\varphi_{\mathrm{perp}}\rangle$, respectively [see Appendix 3.8].

3.10 Paper Appendix III: Target States for Parallel Imaging Scheme

We can also probe the molecular system with light propagating parallel to the magnetic field direction, the so-called "parallel" probing scheme. In such a case, the probe laser is linearly polarized with the polarization lying in the plane perpendicular to the B-field. We selected one of the higher energy hyperfine-Zeeman states as our imaging state for parallel imaging. This level is the only state with $M_{\mathrm{tot}} = -4$ and is thus given by

$$|\varphi_{\mathrm{paral}}\rangle = \left| \mathrm{X}^1\Sigma^+; \begin{array}{c} v = 0, J = 1, M = -1 \\ m_{\mathrm{Na}} = -3/2, m_{\mathrm{Rb}} = -3/2 \end{array} \right\rangle . \tag{3.12}$$

It has the second highest energy of the $v = 0, J = 1$ $\mathrm{X}^1\Sigma^+$ hyperfine states. The only $M_{\mathrm{tot}} = +4$ state can be used as an imaging state as well. For these "circularly polarized" $|M| = 1$

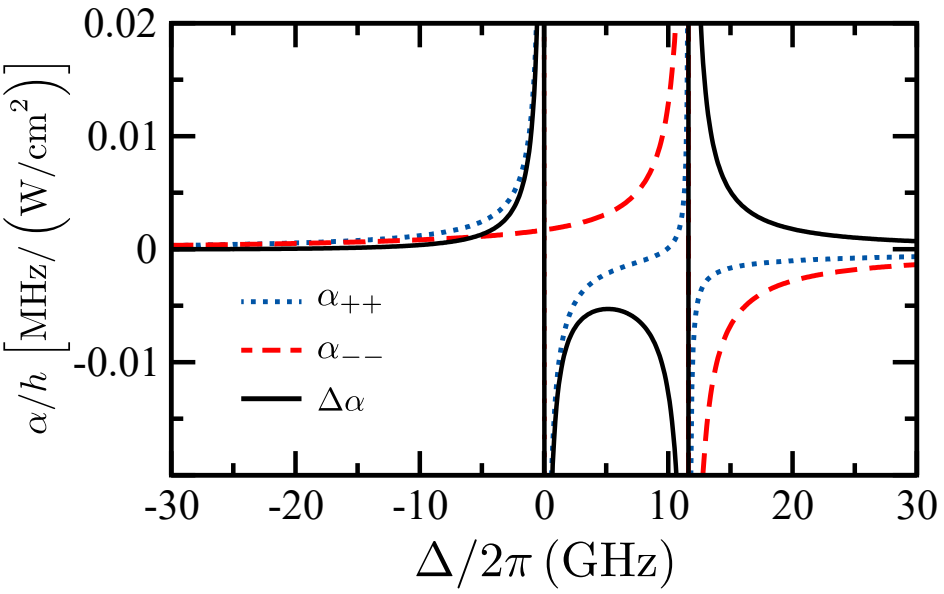

Figure 3.6: Dynamic polarizabilities $\alpha_{++}(\omega)$ and $\alpha_{--}(\omega)$ and corresponding differential dynamic polarizability $\Delta\alpha(\omega)$ for parallel imaging based on the $|\varphi_{\text{paral}}\rangle$ imaging state near the 770 nm transition of the ^{23}Na^{87}Rb molecule shown in Fig. 3.3. We use $B = 335.6\,\text{G}$.

states, the relevant differential polarizability is

$$\Delta\alpha(\omega) = \alpha_{++}(\omega) - \alpha_{--}(\omega), \tag{3.13}$$

where α_{++} and α_{--} are spherical tensor components of the rank-2 dynamic polarizability tensor. This differential polarizability relates to a circular birefringence of the molecules, which will give rise to direct rotation of the probe beam's linear polarization vector.

Figure 3.6 shows the dynamic polarizabilities $\alpha_{++}(\omega)$, $\alpha_{--}(\omega)$, and $\Delta\alpha(\omega)$ for the 770 nm transition to the $n' = 39$ state of the $A^1\Sigma^+$-$b^3\Pi_0$ complex. The poles at $\Delta = 0\,\text{GHz}$ and 11.65 GHz correspond to resonant transitions to $J' = 0$ and $J' = 2$ rotational states, respectively. The $J' = 0$ pole is absent in the curve for $\alpha_{--}(\omega)$ as only $M' = -2$ states are accessible for this polarization tensor component.

In the parallel probing scheme, the differential transition width Γ for the $J' = 0$ transition is larger than that for the perpendicular probing scheme. In fact, the parallel differential transition width is $(c_1^2 - c_2^2/2)^{-1} = 1.44$ times larger for all eigenstates n', leading to differential transition widths of $2\pi\times5.7\,\text{kHz}$, $2\pi\times274\,\text{kHz}$, and $2\pi\times27.8\,\text{kHz}$ for the 884 nm, 791 nm, 770 nm transitions, respectively. The natural linewidths for the parallel probing scheme are

the same as those for the perpendicular probing scheme. Thus, for the same detuning, the parallel probing scheme gives a slightly larger phase difference ϕ than the perpendicular probing scheme.

Finally, we note that the $M_{\text{tot}} = \pm 4$ states, which are most ideal for the parallel probing scheme, can also be utilized for the perpendicular probing scheme. In this case, the pole in the α_{zz} polarizability vanishes near the $J = 1$ to $J' = 0$ transition, while α_{xx} features a prominent pole, as the linear polarization along the $\hat{x}$ axis can drive both σ_+ and σ_- transitions. While the transition widths for these states in the perpendicular scheme are reduced by a factor of 2 from the values they take in the parallel scheme, they will nevertheless give rise to appreciable polarization rotation. More generally, a birefringent response should be possible for *any* state with $J \neq 0$ in either imaging scheme, while for each approach particular states will provide the largest possible rotation signals.

Chapter 4

Future Tasks and Outlook

The primary bulk of my PhD work has been to create an apparatus capable of making ground state ^{23}Na^{87}Rb molecules. This is truly a monumental task, and along the roadmap for molecule creation I've gone from empty lab to the ability to create sub-Doppler cooled gases of ^{23}Na and ^{87}Rb. However more must be done in the future. Thankfully, there's already been some preparation for the next two steps, which I will detail in this chapter. The next major milestone, after having adequate evaporative cooling, is to do Feshbach association into loosely bound ^{23}Na^{87}Rb, followed by Stimulated Raman Adiabatic Passage (STIRAP) to transfer the loosely bound molecules to their ro-vibrational ground state.

Once the molecule creation process is complete, I will wrap up and describe the first experiments we hope to do on our ground state ^{23}Na^{87}Rb, which is heavily influenced by the contents of Chapter 3.

4.1 Feshbach Association

Feshbach association of ^{23}Na^{87}Rb is, at the highest level, the adjustment of the combined ^{23}Na and ^{87}Rb energies such that they're degenerate with a bound state within the $a^3\Sigma^+$ potential. As has been mentioned extensively throughout this thesis, the energy of atomic states can be modified by the application of a magnetic field. Depending on the spin state of the two constituent atoms, there can be resonances at particular values of a magnetic field that just happen to coincide with some state within the $a^3\Sigma^+$ potential. Often, this phenomenon is described via the use of the "entrance" and "exit" channel picture. In this case, the atoms are entering via the $X^1\Sigma^+$ potential and the relative energy of the $a^3\Sigma^+$ potential is being modified to induce the resonance. In the vicinity of the energy crossing between a free atom-like state and a bound molecular state, the properties of scattering

atoms are strongly modified due to *dressing* by the nearby molecular state. Consequently, a Feshbach resonance corresponds to a divergence of the interspecies scattering length between ^{23}Na and ^{87}Rb. This is shown in Figure 4.1.

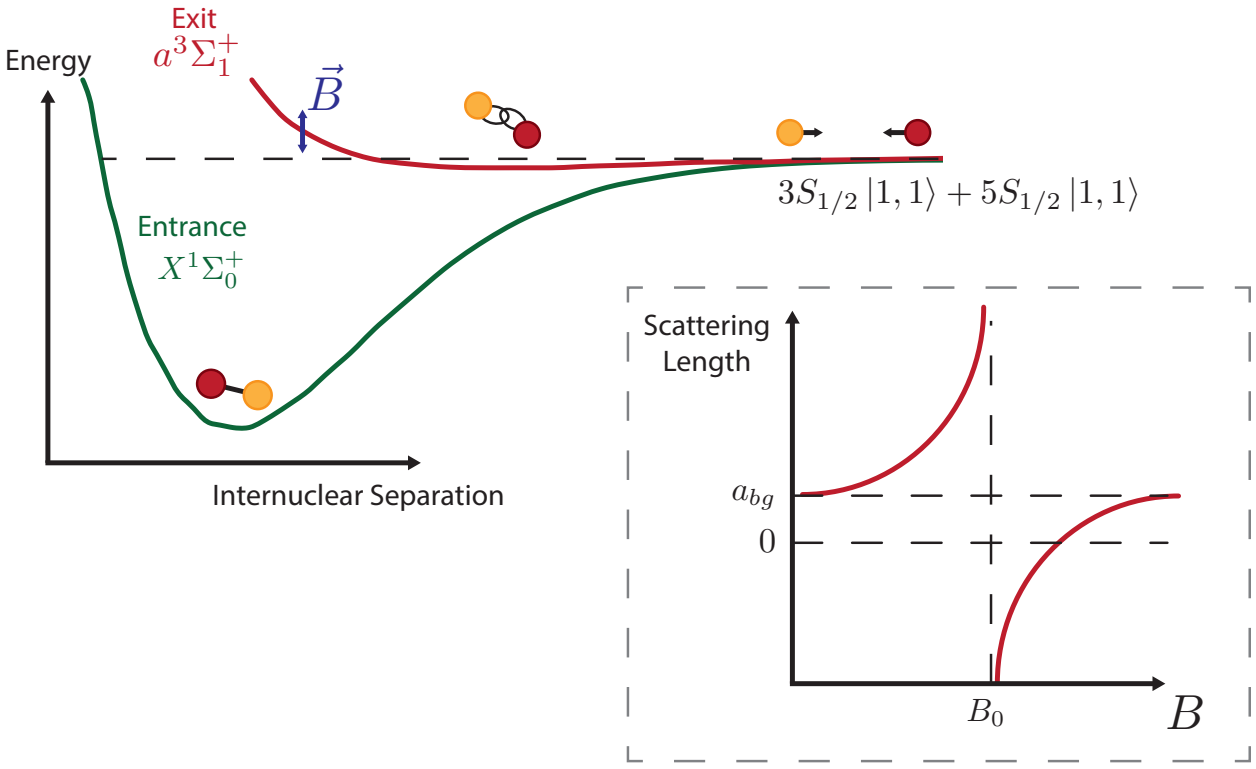

Figure 4.1: Cartoon diagram of Feshbach association of ^{23}Na^{87}Rb. On the left are the relevant entrance and exit channel potentials for ^{23}Na^{87}Rb. A sodium and rubidium atom in their $|F, m_F\rangle = |1,1\rangle$ ground states collide with an energy shown by the horizontal dashed black line. The relative energy of the $a^3\Sigma_1^+$ state is modified by the application of the magnetic field such that the population in the bound state can be prepared through adiabatic rapid passage from the free atom scattering state by crossing the Feshbach resonance. In the dashed box, a cartoon illustration is shown of the interspecies ^{23}Na and ^{87}Rb scattering length as a function of magnetic field around the resonance value B_0. The quantity a_{bg} corresponds to the background scattering length.

The Feshbach resonances of ^{23}Na and ^{87}Rb mixtures have been studied extensively by the group of Dajun Wang [44, 99]. For our purposes, the resonance located at 347.7 G for ^{87}Rb and ^{23}Na in their $|F, m_F\rangle = |1,1\rangle$ state is the target resonance. At this field, the atoms become degenerate with the $a^3\Sigma^+|v = 21, J = 1\rangle$ loosely bound molecular state.

In our experiment we are prepared to do Feshbach association via the use of the magnetic field coils mentioned in Section 2.2.4 and detailed in Appendix A. The calibration of the Feshbach fields, in terms of a particular current in our specific coils, will be done using rf

spectroscopy of internal state transitions. We can confirm our calibration by looking for strong atomic loss near the Feshbach resonance, as the divergence in the scattering length corresponds to a dramatic increase of three-body recombination. This loss of atoms can be measured using standard absorption and fluorescence imaging techniques.

The actual Feshbach association process involves "jumping" the magnetic field to a value above the resonance and then lowering the field at an optimal rate to a value below the resonance. The procedure requires a timing balance of crossing the resonance slowly enough to maintain adiabaticity in the production of the molecules while simultaneously going quickly enough to avoid too much loss through the enhanced three-body recombination. Waseem Bakr's group at Princeton determined a good magnetic field sweep rate of 2.5 G/ms [47] while Dajun Wang's group observed 3.9 G/ms. At the end of Feshbach association we aim to have on the order of 10^3 loosely bound molecules to then transfer into their ro-vibrational ground state as described in the next section.

4.2 Stimulated Raman Adiabatic Passage

The final stage that is necessary for creation of ro-vibrational ground state molecules is the use of a coherent two-photon process called Stimulated Raman Adiabatic Passage (STIRAP). This is an almost magical process that takes thousands of Kelvin worth of energy and removes it from the loosely bound Feshbach molecules and into a light field. One could ask the question why Feshbach molecules, being at higher energy and therefore an "excited" state, do not directly decay into the ro-vibrational ground state. The reason is two fold: first, the Feshbach molecules are created in the triplet $a^3\Sigma^+$ potential, and therefore there is no spin-conserving process to decay into the singlet $X^1\Sigma^+$ potential. The second reason is that the Franck-Condon factors that govern vibrational decay are very small for the Feshbach and ro-vibrational ground state, as the triplet potential does not have significant spatial overlap with the singlet potential. However, a two photon process can be used to coherently transfer population from one to the other. For ^{23}Na^{87}Rb this process involves light at 770 nm and 1248 nm for our selected STIRAP approach.

As previously mentioned, the Feshbach molecules live in a triplet configuration electronic

state and the target ro-vibrational ground state is a singlet. Therefore, an excited state that has components of both triplet and singlet must be found. For us, this comes from the mixing of the $A^1\Sigma^+$ and $b^3\Pi$ potentials. In much the same way the dissociated atomic pair of $3S_{1/2} + 5S_{1/2}$ form into the $a^3\Sigma$ and $X^1\Sigma^+$ potentials at close range, the dissociated $3S_{1/2} + 5P_{1/2}$ and $3S_{1/2} + 5P_{3/2}$ atomic states form their own potentials at short range too. However, unlike the $a^3\Sigma/X^1\Sigma^+$ combination, the $b^3\Pi$ potential has significant depth and spatial overlap with the $A^1\Sigma^+$ state. As a result of spin-orbit coupling, the states that exist in this excited electronic manifold have varying mixtures of singlet and triplet character [2]. It is within this potential where we can find the $(A^1\Sigma^+ - b^3\Pi)|v' = 55, J = 1\rangle$ target state to perform STIRAP.

The 1248 nm light addresses the transition from the Feshbach $a^3\Sigma^+|v = 21, J = 1\rangle$ state to the intermediate target state, while the 770 nm light provides the connection to the ro-vibrational ground state $X^1\Sigma^+|v = 0, J = 0\rangle$. One may be inclined to suggest that when the Feshbach molecules are made, we simply turn on the two light fields to connect the three states, however we must do this with care. As has been mentioned throughout this thesis, actually exciting a molecule into the excited electronic potential is a recipe for loss due to the plethora of decay channels within the molecule. Therefore, a scheme must be employed to adiabatically transfer the population from the Feshbach to the ro-vibrational ground state *without* actually populating the intermediate excited state. This is the purpose of STIRAP.

STIRAP is actually a general name given to a particular sequence of coupling pulses in a three-level system [100]. Consider Figure 4.2 below. States $|G\rangle, |E\rangle,$ and$|F\rangle$ are the ground, excited, and Feshbach states respectively. Two laser beams P and D, with Rabi frequencies $\Omega_P = -d_{EF}\mathcal{E}_P/\hbar$ and $\Omega_D = -d_{GE}\mathcal{E}_D/\hbar$, connect the $|F\rangle \rightarrow |E\rangle$ and $|G\rangle \rightarrow |E\rangle$ transitions, respectively. Here d_{ab} is the dipole matrix element connecting states a and b, $\mathcal{E}_a$ is the electric field amplitude of the laser a, and Δ is the detuning of lasers P and D from their respective transitions to $|E\rangle$. When considering the Hamiltonian of this three-level system we see there are three eigenstates, the most relevant of which is the dark state $|\Phi_0(t)\rangle = \cos\theta(t)|F\rangle - \sin\theta(t)|G\rangle$, where $\tan\theta(t) = \Omega_P(t)/\Omega_D(t)$. STIRAP involves dynamically adjusting the Rabi frequencies $\Omega_P(t)$ and $\Omega_D(t)$ in such a way as to start completely in state $|F\rangle$ and end in $|G\rangle$ so as not to populate $|E\rangle$, a state which is prone to

loss. As shown in the right side of Figure 4.2, this leads to a rather counter-intuitive laser pulse sequence that involves first coupling the unpopulated states $|G\rangle$ and $|E\rangle$ and then coupling $|E\rangle$ and $|F\rangle$.

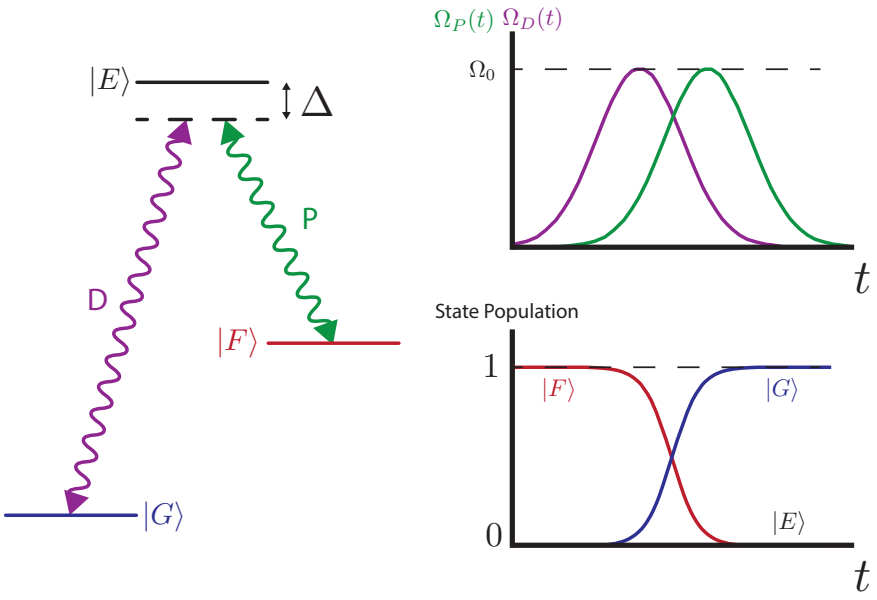

Figure 4.2: Cartoon diagram of STIRAP. The diagram on the left shows the three levels used in the transfer from the Feshbach $|F\rangle$ to the ground state $|G\rangle$ using "pump" and "dump" lasers P and D to off-resonantly (Δ) connect to an intermediary electronic excited state $|E\rangle$. At the top right shows the Rabi frequency (laser power) of the pump and dump lasers as a function of time in order to achieve the bottom right population transfer. STIRAP intentionally does not populate the intermediary excited state $|E\rangle$ in order to avoid radiative loss. Figure adapted from Ref. [100].

4.2.1 Pound-Drever-Hall Locking

The STIRAP procedure requires the maintenance of a coherent dark state resulting from the simultaneous and phase-coherent application of two very different laser fields. That this process works, for lasers separated by roughly 100 THz, is a remarkable testament to advances in laser frequency stabilization and metrology. A powerful method for both stabilizing the individual laser frequencies and maintaining their mutual phase coherence is through Pound-Drever-Hall locking to a common reference cavity. Consider our implementation of PDH in Figure 4.3.

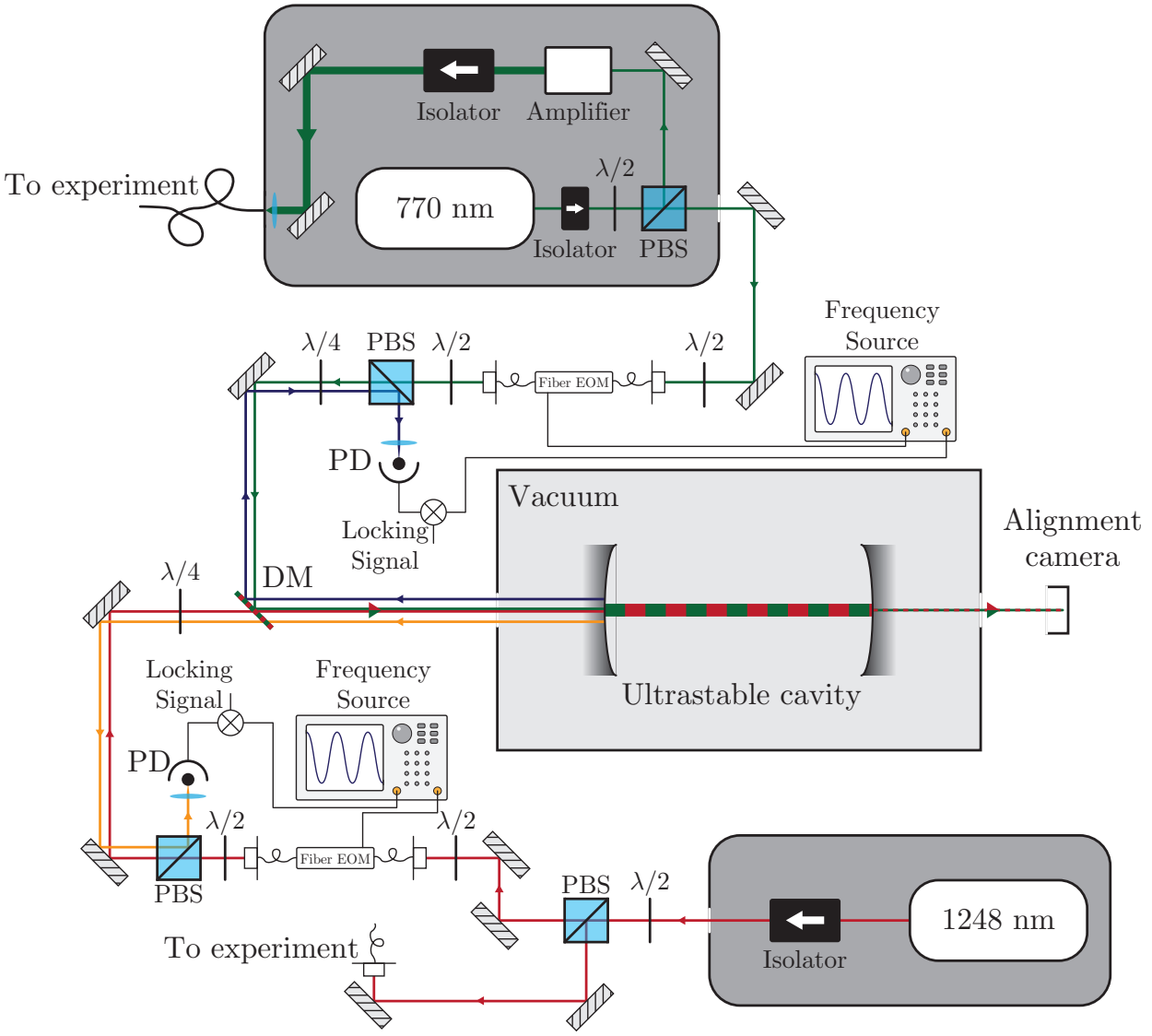

Figure 4.3: Laser system layout for doing Pound-Drever-Hall locking to an ultra-stable high-finesse cavity for use in STIRAP.

Let us think only of the 770 nm laser for the time being, both lasers are independently locked to a common cavity using their own separate PDH setups. The light leaves the laser and passes into an electro-optic modulator (EO Space PM-0S5-05-PFA-PFA-770-UL). We can consider the frequency of the incoming light as ω_0 and the EOM is being driven at frequency ω_m. Upon exiting the EOM, the laser now has multiple frequency components, primarily the carrier ω_0 and the two first order sidebands $\omega_0 \pm \omega_m$. These three distinct frequency beams are copropagating and pass through a polarizing beam splitter and

a quarter-wave plate set at 45 °. Afterward, they are directed into an ultrastable high-finesse cavity. The cavity is designed with two confocal mirrors placed approximately 6.7 cm apart as to give the cavity a *free spectral range* of ≈ 1.5 GHz. This corresponds to the spacing (in frequency) of the many cavity resonances. The mirrors are also designed to be highly reflective, with a reflectivity greater than 99.98 % so as to give the cavity a *finesse* of over 20000. The finesse corresponds to the "sharpness" of the resonance, or how precise the frequency must be in order to match the condition for light to enter the cavity.

Upon arrival at the outside of the cavity, we will first assume that the laser is not resonant with a cavity mode. In this case, the three light frequencies encounter an incredibly reflective mirror, and as such, they bounce off the entrance of the cavity and propagate backward along their entrance path. Since they will have passed through the QWP twice, with a reflection in between, their polarization is now vertical and the light is directed onto a photodiode. Now, we must consider the signal processing path.

At the photodiode, the three light frequencies will produce a set of beat note signals at frequency ω_m and $2\omega_m$ as a result of carrier-sideband and sideband-sideband interference. This signal is then mixed, as was the case in modulation transfer spectroscopy, with a local oscillator reference signal at frequency ω_m that was used to drive the EOM and apply the sidebands. When one of the three frequency components of the beam is resonant with a cavity mode, the beat signal on the photodiode changes. For instance, if the carrier wave is resonant with the cavity, it no longer immediately reflects off the first cavity mirror. Instead, it will transmit and enter the cavity, and a small fraction of the light will leak back out of the cavity to return with the two immediately reflected sidebands. This time, upon arriving at the photodiode, the leaked carrier light will have an additional phase component due to its travel within the cavity given by $\omega_0 * L/c$ where L is the length of the cavity. Without going into even more detail here, I would point the reader to Ref. [101] for a rigorous derivation of the locking signal that can be extracted from the PDH technique. However, the main idea is that the phase difference acquired by a resonant frequency component can be detected after demodulation with the local oscillator frequency in the mixing process, giving a dispersive signal on which the laser can lock.

To note, while I have described direct locking of the laser frequency to the cavity res-

onance, we will actually implement a double-modulation approach (enabled by the use of high-bandwidth fiber EOMs) and lock a large-offset sideband to the cavity (using PDH based on smaller frequency sidebands). In locking to a large-offset sideband, we enable the ability to tune the laser frequency over a large range. This is important, as the cavity resonances provide a stable *relative* frequency stability, but not an absolute reference. To calibrate the frequencies of the pump and dump beams, we will use a form of "STIRAP spectroscopy." This will involve first looking for the loss of Feshbach molecules with direct excitation of the pump transition, and then the dump laser will be calibrated by observing EIT/Autler-Townes splitting in the pump transition.

An extensive characterization of STIRAP on ^{23}Na^{87}Rb has been done by Dajun Wang's group, and I would point the reader to this reference for their process of laser frequency calibration [102]. After the implementation of STIRAP we aim to have thousands of ro-vibrational ground state ^{23}Na^{87}Rb, on which we can begin to explore the plethora of science available to ultracold molecules.

4.3 Outlook

Upon the creation of ultracold ^{23}Na^{87}Rb in its ro-vibrational ground state, the bounty of molecular science possibilities opens up to our experiment. At first, the ambition will be to implement the bulk imaging scheme described in Chapter 3. Most likely this will be done using the 770 nm transition outlined in the paper as it will be a laser we readily have available that will already be tuned to the proper molecular excited state.

Additionally, the imaging scheme we detailed relies on having a population of rotationally excited molecules, therefore we will also need to implement the tools to do so. Rotational states of molecules, as mentioned, are driven by GHz frequency electric fields. To this end, we have at our disposal a microwave horn antenna from Narda and a corresponding Mini-Circuits amplifier. The microwave frequency to drive the $|J = 0, m_J = 0\rangle \rightarrow |1, 0\rangle$ rotational state transition will be generated using a Vaunix LMS-802 "lab brick." The frequency of this transition is approximately 4.18 GHz [103].

Parallel to the implementation of our imaging scheme will likely also be considerations

for a second generation vacuum chamber for the experiment. In particular, the ability to have in-chamber electrodes for generating electric fields will be quite useful. These will allow for explicit polarization of the internal molecular electric dipoles, and as such, provide an additional mechanism by which to tune the dipole-dipole interaction of our molecular cloud. In addition, having non-dispenser sources of atoms prior to evaporation should aid in the creation of larger and denser samples of ground state molecules. Sodium's starting atom number stands to gain the most benefit should the MOT be loaded from a Zeeman slower or 2D MOT, rather than simply background gas from a dispenser.

At the beginning of this thesis I said that molecules are a veritable playground for physicists to understand and make use of our natural world. Though molecule experiments can be hard, they can pay off in a big way. It is my hope that in a short time this apparatus will see the realization of ^{23}Na^{87}Rb ground state molecules. In addition, I hope this document has served as a useful reference for my successors in this experiment.

Appendix A

The Feshbach Coil Making Guide

This document will detail the things necessary to make magnetic field coils with fine control over the current. All part numbers are McMaster-Carr unless otherwise specified.

A.1 The End Goal

What we will make is a set of magnetic field coils that can be in either a Helmholtz or anti-Helmholtz configuration for field/gradient as necessary. At a current of around 80 A the coils will be able to make either a field of 400 G or a field gradient of 150 G/cm.

The current will be controlled by a servo circuit and have an independent readout from a current transducer.

A.2 The Coils

Here are the physical materials necessary to make the coils:

1. **5174K1** - 1/8" hollow copper refrigerator tubing
2. **7856K34** - heat-shrink tubing

The coils will be wound in a 6 x 6 grid, on the holders described below, for a total of 36 turns per holder.

The Top Holder

The holder can be made of any durable material that you like. I recommend either Delrin® or aluminum. Regardless of what you use, if you make the coils as I did, you'll need a 6" diameter 4" long round of the material you choose. For me, this was **9986K35**.

In addition to the bulk material that will be machined for the holders, you should also buy some 1/2" thick (or slightly larger) Delrin rods. They come in a minimum length of 5 ft, **8576K15**. You will want 4 rods, each 3.575 in long, and they will be 1/4"-20 tapped on both ends.

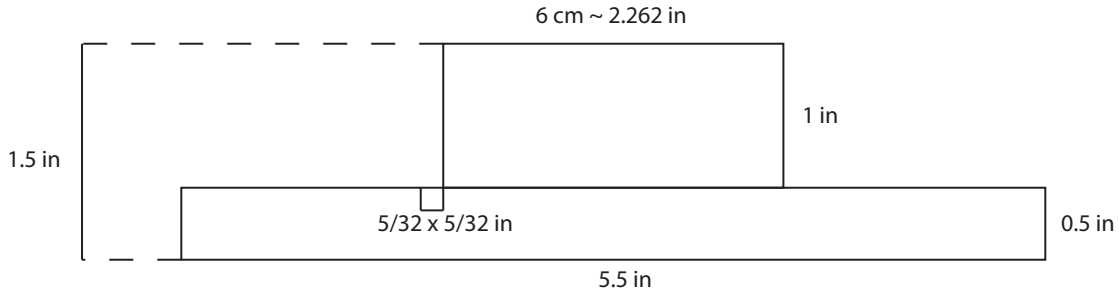

Figure A.1: Top coil holder seen from the side.

Delrin® is pretty easy to machine so there should be no big hangups. I would recommend turning down the diameter of the big stock that you order first, bore out the middle hole, cut the stock in half (so as to have two identical copies, which you do need), and finish off by turning down the diameter of each to "carve out" the center support. Though yours will be different since you want the top covering.

The Bottom Holder

All is the same here except you need to add 4 1/4"-20 tapped holes in a square pattern along the base of the holder. The placement isn't super critical. These will be used to mount to a plate that the entire holder assembly will rest on. The plate itself I made out of a 1/4" thick slab of aluminum. It's important that the aluminum plate has a 6cm hole placed in it (for beam clearance of course) and a set of similarly placed 1/4" through holes. Elsewhere on the plate you'll want to place another 4 1/4" through holes for mounting onto 1.5" posts that connect the entire assembly to the table. **Important:** the aluminum plate needs a thin channel cut from the outside through to the big circle in the middle. This will be to prevent eddy currents in the plate.

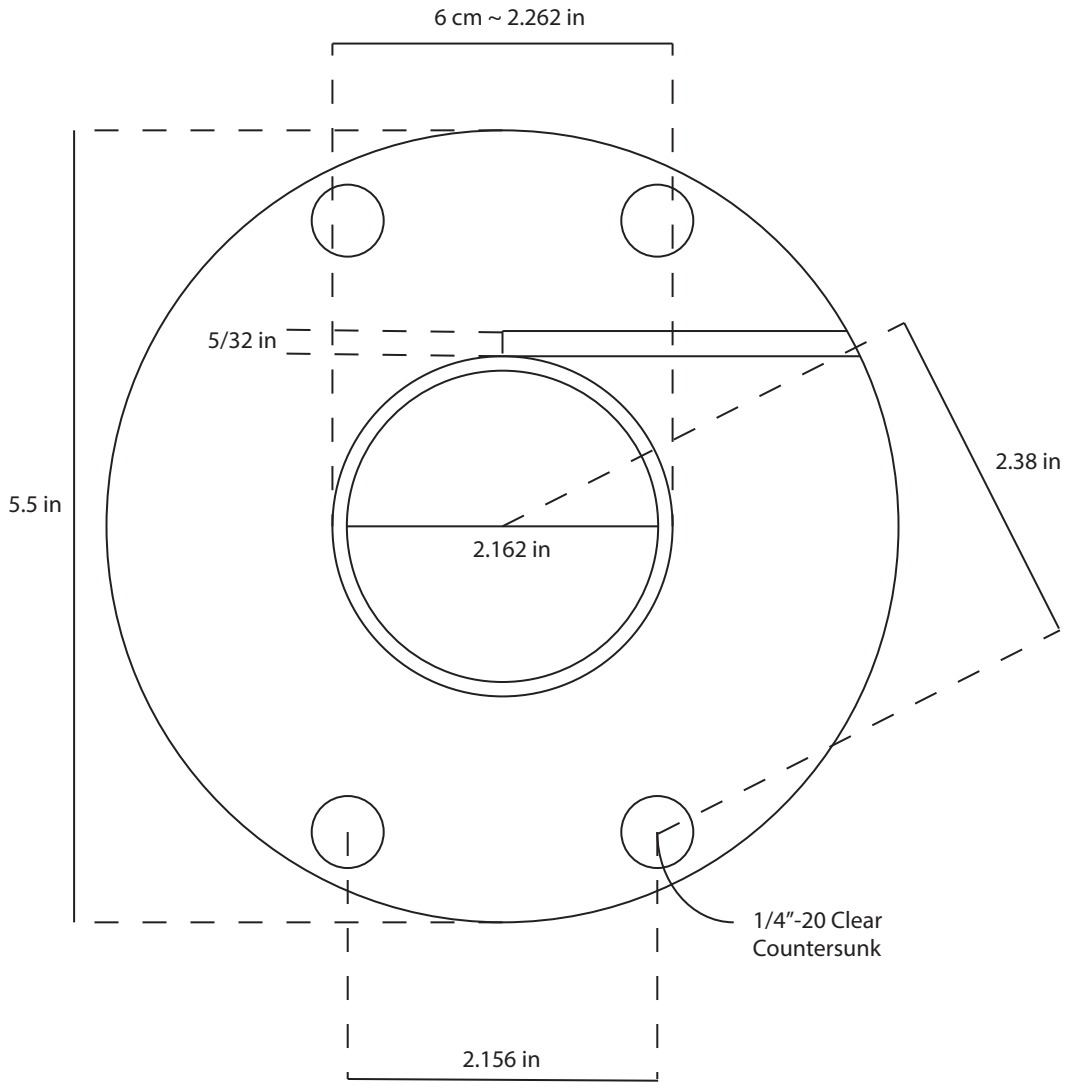

Figure A.2: Top coil holder seen from the top.

Winding

The winding of these coils was done using a rotary table. Your job is to find some clever way to mount the holder to the rotary table so that it's centered and stable. You'll start the winding of the coils in the channel that was cut out during machining. This end needs to be held at first to provide the forward going tension on the winding process. On the back end you need to apply tension as well, we did so via the use of Teflon guides made by the DeMarco group. The coils passed through this guide which serves the purpose of straightening out the tubing and providing the back tension.

You will be winding a 6 x 6 grid of coils on the top and bottom holder. You will want to

apply a thick coating of 2-ton epoxy (Amazon - **B01LZVD407**) between each layer.

A.3 Plumbing

Important: though you may not use exactly the same plumbing components, you must make sure **ALL components are either copper or brass**. This is to prevent electrolysis, which leads to corrosion.

General Note: All pipe fittings/threaded connections should have Teflon tape. All compression fittings should **not** have Teflon tape, as it interferes with the compression process. Here's a list of things you'll want:

1. From the wall (which I believe all supplies are 3/4" threaded, so the rest of the parts are calibrated to that), tee off both the supply and return lines with a cross: **4429K354**.

2. You'll likely not be running three lines to start, so you'll want some plugs for the unused stuff: **4429K283**.

3. You'll likely need at least four to six of these for general connectivity: **4568K191**.

4. When running water you want to have the thickest (within reason) ID tubing for the longest length possible. A good upper bound on "within reason" is 3/8" tubing: **5548K77**.

5. In my experience the compression fittings for the *plastic/nylon* tubing work better when the compression sleeve is itself plastic. Get a lot of these for when you mess up and need to re-do the connection: **50915K195** & **50915K193**.

6. From the tee to the MOSFET cooling plate (**35035K32**) you'll need a reducer and a compression fitting: **4429K737** & **50915K325**.

7. From the tubing to the cooling plate you'll need a straight connector: **50915K135**.

8. From the *supply* tee to the coils you'll again need a reducer and a compression fitting, the same as in 6. The tubing will terminate on or near the table to a breakout with a plug: **5627K502** & **50785K23**.

9. To connect the supply tubing to the breakout: **50915K324**.

10. On the other side of the breakout you'll be running 1/4" tubing (**5548K75**) until you get to the coils themselves. Connecting to the breakout: **50915K315**.
    The breakout is designed so that there will be an independent supply and return to the top and bottom coils. Were it all one loop, either the top or the bottom would be cooled by the warmed up water from the previous coil. This is clearly not ideal.

11. From the 1/4" tubing to the coils you have a choice for what fittings you'll want. In general it's good to reduce turns to aid in flow, so avoid right angles if you can: **50915K314** & **50915K211**.
    The compression sleeve that connects the fitting with the copper tubing needs to be brass, but this kind: **5272K602**, rather than the brass sleeve that comes with.

12. On the *return* side for both the FET cooling plate and the coils, you can just mirror the connections, breakout, etc. with the exception of...

13. The flowmeter. Our Omega FTB2003 flowmeter is installed on the return path below the two coil water recombination block. This flowmeter outputs a square-wave frequency based on the flow rate it detects. Our "standard" operating frequency is 33 Hz.

A.4 Electrical

So you want to run current through the coils to make a magnetic field? Well you're gonna need some electrons. Here's the overall schematic of all the paths your fundamental particles will need to take to give rise to your field:

The next sections will detail each of the components in the schematic above.

The Hall Probe/Current Transducer

Colloquially I have used "Hall probe" to describe the device that is measuring the current in our wires. This is the Danisense DS200ID and was bought through GMW Associates

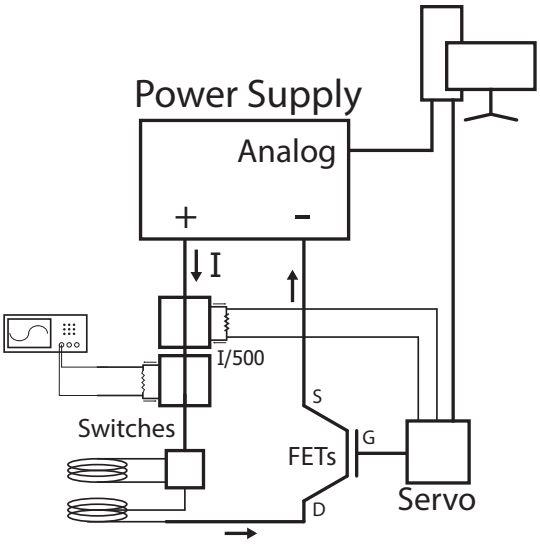

Figure A.3: Diagram of the entirety of the Feshbach coil current path.

(sales@gmw.com). The device is actually a current transducer, and it reads the current in the main wire and will send $1/500^{\text{th}}$ the current through a sense resistor that you will supply: (Digikey - **696-1708-ND**). This is a 50 Ω resistor that was selected such that at 80 A in the coils corresponds to a voltage across the sense resistor of a manageable 8 V. This also corresponds to the Cicero set voltage of the coils. A 2.0 V Cicero setpoint will correspond to a 20 A current.

A second transducer is also used that is independent of the servo circuit. It provides an out-of-loop monitor of the current that we send to an oscilloscope above the north computer.

An important note on setting the transducer up: it is important that the the 2/0 gauge wire going through the probe be secured well. Small movements inside the probe will give inaccurate readings on the current, and therefore the calibration of the servo circuit. For this reason, we machined a copper rod with terminal lugs on either end that has an OD that matches with the ID of the current transducer.

Switching

In order to switch from having Helmholtz coils or anti-Helmholtz I am using mechanical switches. These are simple SPST switches of which you will need four: (Mouser - **LEV200A4ANA**). They will be hooked up like so...

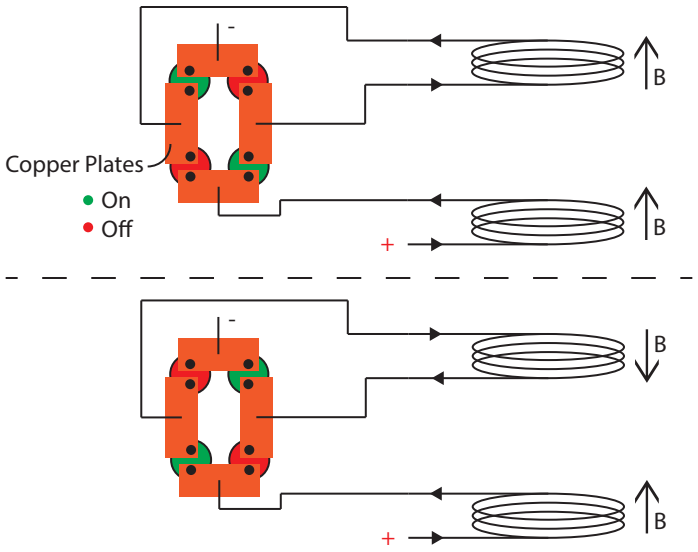

Figure A.4: Schematic of the automotive mechanical switches that are used to orient the current in either a Helmholtz or anti-Helmholtz configuration.

The switches are turned on or off by using a 12 V TTL switch, and they draw a lot of current (about 2 A/set). The power supply is connected to a series of FET switches that take in a TTL for either the anti-Helmholtz or Helmholtz configuration, and they have corresponding channels in Cicero.

The Servo Loop

The entire purpose of this circuit is to remove microwave noise that gets written onto the coils thanks to nature, as well provide fine control of the current in the coils that is set by some user controllable input voltage. Here is the functional schematic of the servo circuit.

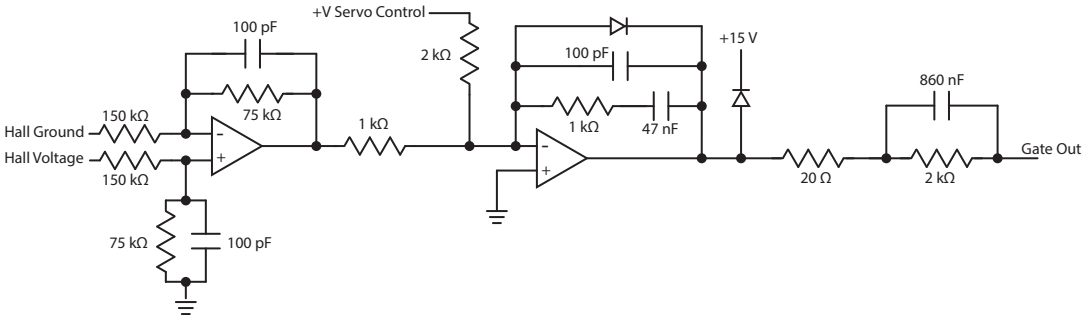

Figure A.5: Electrical schematic of the servo circuit PCB.

Functionally, this circuit does the following:

1. On the Hall Voltage input there is a drain to ground that is a high pass centered at 133 kHz.

2. The first op-amp is an integrator with a an output voltage given by

$$V_{\text{out}}(\omega) = \frac{2\times 10^5}{6\times 10^5 + 3i\omega}\left(1 + \frac{2\times 10^5}{4\times 10^5 + 3i\omega}\right) V_{\text{Hall V}}(\omega) - \frac{2\times 10^5}{4\times 10^5 + 3i\omega} V_{\text{ground}}(\omega).$$

   In the DC limit this is $V_{\text{out}} = (V_{\text{Hall}} - V_{\text{ground}})/2$, and the very high frequency limit $V_{\text{out}}(\omega \to \infty) = 0$.

3. The next op-amp does the actual servo-ing. It is a summing amplifier of the servo control voltage and the difference signal of the Hall voltages. Nominally this voltage will be negative, as the amplifier's goal is the make the sum of these two voltages be zero.

   i. The diode across the second op-amp forces the output to be greater than 0 V.

   ii. The diode between the second op-amp and the gate out is to prevent overloading the FETs by sending a maximum 15 V to the gate (which is a completely open FET).

   iii. The bandpass filter before the gate out is so that the second op-amp will send low frequency corrections to the FETs, and high frequency corrections will be controlled by the integrator around the second op-amp.

Here is a parts list of all that you will need to make the circuit board (through-hole unless otherwise mentioned):

1. 8×100 nF Surface Mount Capacitor

2. 5×100 pF Capacitor

3. 1×47 nF Capacitor

4. 1×860 nF Capacitor

5. $2 \times 1\,\mu$F Capacitor

6. $2 \times 10\,\mu$F Capacitor
7. $2 \times 1\,$kΩ Resistor
8. $2 \times 2\,$kΩ Resistor
9. $2 \times 5.1\,$kΩ Resistor
10. $1 \times 20\,\Omega$ Resistor
11. $4 \times 150\,$kΩ Resistor
12. $4 \times 75\,$kΩ Resistor
13. $1 \times 50\,\Omega$ Resistor
14. 2$\times$ 1N4148 Diode
15. 3$\times$ OP27 series Op-Amps

Note: I was unable to find exactly a 2 kΩ resistor and a 860 nF capacitor, so I used 820 nF and 2.1 kΩ, as they have roughly the same time constant.

FETs

The variable resistor that the servos will use to control the current are a set of MOSFETs (Digikey - **IXFN230N10-ND**). As mentioned before these will be mounted to a cooling plate that connects to your plumbing manifold. For the currents we will be driving, it is safest to have two FETs in parallel to help break up the current load.

Power Supply (big)

Here it's a good idea to make sure the power supply is of course rated for high power, has some form of external control over its terminal voltages (like analog or GPIB), and provides a healthy voltage ceiling for say a 200 A max drive.
To elaborate, I currently am using the DeMarco supply which has a 0-8 V/500 A rating. I don't need 500 A but I could use more than 8 V (due to the resistance of the coils), so

were I to buy my own supply I'd look for something like 0-20 V/200 A. Both have the same overall 4 kW rating, but the latter is more adapted to our specific purpose. Note: the mains power supply plug for running high power equipment are 230 V_{AC}/30 A plugs called NEMA L15-30. I used an extension cord from McMaster: **5839K37**.

Power Supply (small)

We use a low noise linear power supply for powering the servo and Hall probe (Digi-key - **271-2280-ND**).

One note is that the ground pin is not directly connected to the case of this power supply, so care should be taken to make that connection explicitly.

Enclosures

One of the main reasons to go to great lengths to control the current of the coils is so that around the Feshbach resonance we have a noise free, precisely controlled current and therefore field. The main source of noise in this circuit will be stray microwaves. These will be written on everywhere, so the method to combat this is to house all of the electronic components into metal enclosures. Now admittedly, I overbought (in that I have more space in the boxes than I can possibly use), but the boxes should work none the less.

One of the most important considerations is the "star ground." This is a highly important terminal through which you will connect several components **independently**. These include:

1. The servo needs to be powered by a +15/-15 V power supply. The ground terminal of this power supply needs to be connected to the star ground.

2. The negative terminal of the bulk power supply will be connected to the star ground (this in particular should be a thick wire, something like **6948K89**. In fact, use this for all star ground connections if possible.)

3. The enclosure will be connected to the star ground. To do this, you will need to remove paint strategically such that all three boxes and the overall enclosure have a metal on

metal contact point, and then find a way to fasten the wire onto the enclosure that connects to star ground.

If it is not on this list, do not connect it to star ground. The servo circuit has its own ground, the transducer has its own ground, the FETs should be mounted on the cooling plate that is electrically isolated from the enclosure, and so on.

A.5 Summary

Hopefully this guide has provided information on both the workings of the Feshbach coils, as well as how to construct them, or at least general best practices in construction when considering machining, plumbing, electrical, etc.

Appendix B

Codes and Programs

In this short appendix I will transcribe the code used to do atom imaging analysis in our experiment. This code is designed to work in Mathematica, alongside a custom-made Mathematica package that is installed on the Gadway Lab computers.

```
Sample Code for a Time of Flight Measurement of Rubidium. Code assumes running
    the SweetSuitePackGadgeV201, which can be found in the Gadway Lab Box Folder.

In[216]:= sn = 5; (*Image Number that starts the data set*)
inputvars = {5, 10, 15, 20};
reps = 1;
vars = Flatten[Table[#, reps] & /@ inputvars];
xlabel = "TOF (ms)" ;
en = sn + Length[vars] - 1
labels = inputvars;
ruborna = "Rb"

Out[221]= 8

Out[223]= "Rb"

Cam66

In[224]:= path = PathFinder[sn, en, "Cam66"]; (*finds the filepath to pull the
    images from*)

During evaluation of In[224]:= Detected images 5-8 within specified range

In[225]:= rawimages = GetDatBIN[path, "66"]; (*imports the images as 2D arrays*)

imgdims = Reverse[Dimensions[rawimages][[2 ;; 3]]];
center = {600, 1100};
span = {999, 1300};
croppedimages =
rawimages[[;; ,
Round[center[[2]] - span[[2]]/2 + 1] ;; Round[center[[2]] + span[[2]]/2],
Round[center[[1]] - span[[1]]/2 + 1] ;;
Round[center[[1]] + span[[1]]/2]]] ; (*crops the image to a region of interest*)
```

```
centerbg = {100, 100}; (*defines a region of no atoms to calculate a background (
    used in florescence imaging)*)
spanbg = {50, 50};
cropimgbg =
rawimages[[;; ,
Round[center[[2]] - span[[2]]/2 + 1] ;; Round[center[[2]] + span[[2]]/2],
Round[center[[1]] - span[[1]]/2 + 1] ;; Round[center[[1]] + span[[1]]/2]]];
bgaverage = Mean[Flatten[#]] & /@ (Mean /@ Partition[cropimgbg, reps]);
images = Mean /@ Partition[croppedimages, reps];
flimages = Mean /@ Partition[croppedimages, reps] - bgaverage;
size = 200;
ArrayPlot[1 (images[[#]]), ColorFunction -> "Gadient",
ColorFunctionScaling -> False, PlotLabel -> labels[[#]],
MaxPlotPoints -> size {imgdims[[2]]/imgdims[[1]], 1}/2,
AspectRatio -> Dimensions[images[[1]]][[1]]/Dimensions[images[[1]]][[2]],
ImageSize -> size, Method -> {"GridLinesInFront" -> True},
PlotRangePadding -> 0, DataReversed -> True] & /@
Range[Length[images]][[Ordering[inputvars[[;; Length[images]]]]]] (*generates a
    false color 2D image of the atomic density*)

(* Print[Style["using constants for " <>ruborna,Red]];
nums=If[ruborna\[Equal]"Na",NaFitFluDat[Transpose[#],0.088*10^-3,False]&/@\
images,
If[ruborna\[Equal]"Rb",RbFitFluDat[Transpose[#],0.088*10^-3,False]&/@images,\
Print["c'mon"]]] *)

(* Power in Absorption imaging beam: ~300 \[Mu]W for Rb and ~160 \[Mu]W for \
Na *)
Print[Style["using constants for " <> ruborna, Red]];
nums = FitDatAbs2[ruborna, Transpose[#], 0*10^6*2 \[Pi], 300*^-6,
pixelsizeCam66, ImageMagnification66, 9.5*^-3, False] & /@ images (*calls upon a
    function written to calculate the atom number, size, density, and position*)

In[241]:= datn = Transpose[{inputvars[[;; Length[images]]], nums[[;; , 1]]}];
datsigx = Transpose[{inputvars[[;; Length[images]]], nums[[;; , 2]]}];
datsigy = Transpose[{inputvars[[;; Length[images]]], nums[[;; , 3]]}];
datdens = Transpose[{inputvars[[;; Length[images]]], nums[[;; , 4]]}];
datxp = Transpose[{inputvars[[;; Length[images]]], nums[[;; , -2]]}];
datyp = Transpose[{inputvars[[;; Length[images]]], nums[[;; , -1]]}];
ars = Transpose[{inputvars[[;; Length[images]]], datsigx[[;; , 2]]/
       datsigy[[;; , 2]]}];

In[248]:= ListPlot[Sort[datn], FrameLabel -> {xlabel, "Atom Number"},
PlotMarkers -> Automatic]
ListPlot[Sort[ars], FrameLabel -> {xlabel, "Aspect Ratio"},
PlotMarkers -> Automatic]
ListLinePlot[Sort[datsigx], FrameLabel -> {xlabel, "Horiz. Size"},
```

```
PlotMarkers -> Automatic];
ListLinePlot[Sort[datsigy], FrameLabel -> {xlabel, "Vert. Size"},
PlotMarkers -> Automatic];
ListLinePlot[Sort[datdens], FrameLabel -> {xlabel, "Density"},
PlotMarkers -> Automatic];
ListLinePlot[Sort[datxp], FrameLabel -> {xlabel, "X Position"},
PlotMarkers -> Automatic];
ListLinePlot[Sort[datyp], FrameLabel -> {xlabel, "Y Position"},
PlotMarkers -> Automatic];

In[255]:= If[ruborna == "Na", TempFitDatAbs[datsigx, datsigy, MNa, True],
If[ruborna == "Rb", TempFitDatAbs[datsigx, datsigy, MRb, True],
Print["c'mon"]]] (*calculates a temperature, if the variables were a time of
    flight expansion time*)
```

References

[1] J. E. Jones and S. Chapman, "On the determination of molecular fields." Proceedings of the Royal Society of London. Series A, Containing Papers of a Mathematical and Physical Character **106**, 441–462 (1924).

[2] L. D. Carr, D. DeMille, R. V. Krems, and J. Ye, "Cold and ultracold molecules: science, technology and applications," New J. Phys. **11**, 055049 (2009).

[3] B. Podolsky, "Quantum-mechanically correct form of hamiltonian function for conservative systems," Phys. Rev. **32**, 812–816 (1928).

[4] S. E. Maxwell, N. Brahms, R. deCarvalho, D. R. Glenn, J. S. Helton, S. V. Nguyen, D. Patterson, J. Petricka, D. DeMille, and J. M. Doyle, "High-flux beam source for cold, slow atoms or molecules," Phys. Rev. Lett. **95**, 173201 (2005).

[5] L. D. van Buuren, C. Sommer, M. Motsch, S. Pohle, M. Schenk, J. Bayerl, P. W. H. Pinkse, and G. Rempe, "Electrostatic extraction of cold molecules from a cryogenic reservoir," Phys. Rev. Lett. **102**, 033001 (2009).

[6] H. L. Bethlem, G. Berden, and G. Meijer, "Decelerating neutral dipolar molecules," Phys. Rev. Lett. **83**, 1558–1561 (1999).

[7] R. Fulton, A. I. Bishop, and P. F. Barker, "Optical stark decelerator for molecules," Phys. Rev. Lett. **93**, 243004 (2004).

[8] S. Chervenkov, X. Wu, J. Bayerl, A. Rohlfes, T. Gantner, M. Zeppenfeld, and G. Rempe, "Continuous centrifuge decelerator for polar molecules," Phys. Rev. Lett. **112**, 013001 (2014).

[9] H. J. Williams, L. Caldwell, N. J. Fitch, S. Truppe, J. Rodewald, E. A. Hinds, B. E. Sauer, and M. R. Tarbutt, "Magnetic trapping and coherent control of laser-cooled molecules," Phys. Rev. Lett. **120**, 163201 (2018).

[10] L. Anderegg, L. W. Cheuk, Y. Bao, S. Burchesky, W. Ketterle, K.-K. Ni, and J. M. Doyle, "An optical tweezer array of ultracold molecules," Science **365**, 1156–1158 (2019).

[11] D. J. McCarron, M. H. Steinecker, Y. Zhu, and D. DeMille, "Magnetic trapping of an ultracold gas of polar molecules," Phys. Rev. Lett. **121**, 013202 (2018).

[12] L. R. Liu, J. D. Hood, Y. Yu, J. T. Zhang, N. R. Hutzler, T. Rosenband, and K.-K. Ni, "Building one molecule from a reservoir of two atoms," Science **360**, 900–903 (2018).

[13] L. De Marco, G. Valtolina, K. Matsuda, W. G. Tobias, J. P. Covey, and J. Ye, "A degenerate fermi gas of polar molecules," Science **363**, 853–856 (2019).

[14] M. Duda, X.-Y. Chen, A. Schindewolf, R. Bause, J. von Milczewski, R. Schmidt, I. Bloch, and X.-Y. Luo, "Transition from a polaronic condensate to a degenerate fermi gas of heteronuclear molecules," arXiv:2111.04301 .

[15] V. Andreev, D. Ang, D. DeMille, J. Doyle, G. Gabrielse, J. Haefner, N. Hutzler, Z. Lasner, C. Meisenhelder, B. O'Leary, C. Panda, A. West, E. West, X. Wu, and A. Collaboration, "Improved limit on the electric dipole moment of the electron," Nature **562**, 355–360 (2018).

[16] M. S. Safronova, D. Budker, D. DeMille, D. F. J. Kimball, A. Derevianko, and C. W. Clark, "Search for new physics with atoms and molecules," Rev. Mod. Phys. **90**, 025008 (2018).

[17] B. Yan, S. Moses, B. Gadway, J. Covey, K. Hazzard, A. Rey, D. Jin, and J. Ye, "Observation of dipolar spin-exchange interactions with lattice-confined polar molecules," Nature **501**, 521–525 (2013).

[18] Z. Eldredge, Z.-X. Gong, J. T. Young, A. H. Moosavian, M. Foss-Feig, and A. V. Gorshkov, "Fast quantum state transfer and entanglement renormalization using long-range interactions," Phys. Rev. Lett. **119**, 170503 (2017).

[19] B. Neyenhuis, B. Yan, S. A. Moses, J. P. Covey, A. Chotia, A. Petrov, S. Kotochigova, J. Ye, and D. S. Jin, "Anisotropic polarizability of ultracold polar ^{40}K^{87}Rb molecules," Phys. Rev. Lett. **109**, 230403 (2012).

[20] S. A. Will, J. W. Park, Z. Z. Yan, H. Loh, and M. W. Zwierlein, "Coherent microwave control of ultracold ^{23}Na^{40}K molecules," Phys. Rev. Lett. **116**, 225306 (2016).

[21] J. J. Hudson, B. E. Sauer, M. R. Tarbutt, and E. A. Hinds, "Measurement of the electron electric dipole moment using ybf molecules," Phys. Rev. Lett. **89**, 023003 (2002).

[22] R. Barnett, D. Petrov, M. Lukin, and E. Demler, "Quantum magnetism with multicomponent dipolar molecules in an optical lattice," Phys. Rev. Lett. **96**, 190401 (2006).

[23] A. V. Gorshkov, S. R. Manmana, G. Chen, E. Demler, M. D. Lukin, and A. M. Rey, "Quantum magnetism with polar alkali-metal dimers," Phys. Rev. A **84**, 033619 (2011).

[24] B. Capogrosso-Sansone, C. Trefzger, M. Lewenstein, P. Zoller, and G. Pupillo, "Quantum phases of cold polar molecules in 2d optical lattices," Phys. Rev. Lett. **104**, 125301 (2010).

[25] V. W. Scarola, E. Demler, and S. Das Sarma, "Searching for a supersolid in cold-atom optical lattices," Phys. Rev. A **73**, 051601 (2006).

[26] C. Menotti, C. Trefzger, and M. Lewenstein, "Metastable states of a gas of dipolar bosons in a 2d optical lattice," Phys. Rev. Lett. **98**, 235301 (2007).

[27] A. Bühler and H. P. Büchler, "Supersolid phase in atomic gases with magnetic dipole interaction," Phys. Rev. A **84**, 023607 (2011).

[28] H. P. Büchler, E. Demler, M. Lukin, A. Micheli, N. Prokof'ev, G. Pupillo, and P. Zoller, "Strongly correlated 2d quantum phases with cold polar molecules: Controlling the shape of the interaction potential," Phys. Rev. Lett. **98**, 060404 (2007).

[29] A. Micheli, G. Brennen, and P. Zoller, "A toolbox for lattice-spin models with polar molecules," Nat. Phys. **2**, 341–347 (2006).

[30] D. Luo, J. Shen, M. Highman, B. K. Clark, B. DeMarco, A. X. El-Khadra, and B. Gadway, "Framework for simulating gauge theories with dipolar spin systems," Phys. Rev. A **102**, 032617 (2020).

[31] J. Park, Z. Yan, H. Loh, S. Will, and M. Zwierlein, "Second-scale nuclear spin coherence time of ultracold 23na40k molecules," Science **357**, 372–375 (2017).

[32] P. D. Gregory, J. A. Blackmore, S. L. Bromley, J. M. Hutson, and S. L. Cornish, "Robust storage qubits in ultracold polar molecules," Nature Physics **17**, 1149–1153 (2021).

[33] M. A. Nichols, Y.-X. Liu, L. Zhu, M.-G. Hu, Y. Liu, and K.-K. Ni, "Detection of long-lived complexes in ultracold atom-molecule collisions," Phys. Rev. X **12**, 011049 (2022).

[34] W. G. Tobias, K. Matsuda, J.-R. Li, C. Miller, A. N. Carroll, T. Bilitewski, A. M. Rey, and J. Ye, "Reactions between layer-resolved molecules mediated by dipolar spin exchange," Science **375**, 1299–1303 (2022).

[35] P. D. Gregory, J. A. Blackmore, F. M. D, L. M. Fernley, S. L. Bromley, J. M. Hutson, and S. L. Cornish, "Molecule–molecule and atom–molecule collisions with ultracold RbCs molecules," New Journal of Physics **23**, 125004 (2021).

[36] N. Balakrishnan, "Perspective: Ultracold molecules and the dawn of cold controlled chemistry," The Journal of Chemical Physics **145**, 150901 (2016).

[37] G. Quéméner, M.-G. Hu, Y. Liu, M. A. Nichols, L. Zhu, and K.-K. Ni, "Model for nuclear spin product-state distributions of ultracold chemical reactions in magnetic fields," Phys. Rev. A **104**, 052817 (2021).

[38] J.-R. Li, W. Tobias, K. Matsuda, C. Miller, G. Valtolina, L. D. Marco, R. Wang, L. Lassablière, G. Quéméner, J. Bohn, and J. Ye, "Tuning of dipolar interactions and evaporative cooling in a three-dimensional molecular quantum gas," Nature Physics **17**, 1144 (2021).

[39] P. D. Gregory, M. D. Frye, J. A. Blackmore, E. M. Bridge, R. Sawant, J. M. Hutson, and S. L. Cornish, "Sticky collisions of ultracold rbcs molecules," Nat. Commun. **10**, 3104 (2019).

[40] Q. Guan, M. Highman, E. J. Meier, G. R. Williams, V. Scarola, B. DeMarco, S. Kotochigova, and B. Gadway, "Nondestructive dispersive imaging of rotationally excited ultracold molecules," Phys. Chem. Chem. Phys. **22**, 20531–20544 (2020).

[41] D. A. Steck, "Rubidium 87 d line data," available online at steck.us/alkalidata (revision 2.2.2, 9 July 2021).

[42] E. L. Raab, M. Prentiss, A. Cable, S. Chu, and D. E. Pritchard, "Trapping of neutral sodium atoms with radiation pressure," Phys. Rev. Lett. **59**, 2631–2634 (1987).

[43] D. A. Steck, "Sodium 23 d line data," available online at steck.us/alkalidata (revision 2.2.1, 21 November 2019).

[44] Z. Guo, F. Jia, B. Zhu, L. Li, J. M. Hutson, and D. Wang, "Improved characterization of feshbach resonances and interaction potentials between ^{23}Na and ^{87}Rb atoms," Phys. Rev. A **105**, 023313 (2022).

[45] B. Gadway and B. Yan, "Strongly interacting ultracold polar molecules," J. Phys. B: At. Mol. Opt. Phys. **49**, 152002 (2016).

[46] M. Guo, B. Zhu, B. Lu, X. Ye, F. Wang, R. Vexiau, N. Bouloufa-Maafa, G. Quéméner, O. Dulieu, and D. Wang, "Creation of an ultracold gas of ground-state dipolar ^{23}Na^{87}Rb molecules," Phys. Rev. Lett. **116**, 205303 (2016).

[47] J. S. Rosenberg, L. Christakis, E. Guardado-Sanchez, Z. Z. Yan, and W. S. Bakr, "Observation of the hanbury brown and twiss effect with ultracold molecules," arXiv:2111.09426 .

[48] D. J. McCarron, S. A. King, and S. L. Cornish, "Modulation transfer spectroscopy in atomic rubidium," Measurement Science and Technology **19**, 105601 (2008).

[49] A. Keshet and W. Ketterle, "A distributed, graphical user interface based, computer control system for atomic physics experiments," Review of Scientific Instruments **84**, 015105 (2013).

[50] E. Donley, T. Heavner, F. Levi, M. Tataw, and S. Jefferts, "Double-pass acousto-optic modulator system," Review of Scientific Instruments - REV SCI INSTR **76** (2005), 10.1063/1.1930095.

[51] J. Dalibard and C. Cohen-Tannoudji, "Laser cooling below the doppler limit by polarization gradients: simple theoretical models," J. Opt. Soc. Am. B **6**, 2023–2045 (1989).

[52] R. Grimm, M. Weidemüller, and Y. B. Ovchinnikov, "Optical dipole traps for neutral atoms," arXiv:9902072 .

[53] Y.-J. Lin, A. R. Perry, R. L. Compton, I. B. Spielman, and J. V. Porto, "Rapid production of ^{87}Rb bose-einstein condensates in a combined magnetic and optical potential," Phys. Rev. A **79**, 063631 (2009).

[54] F. Wang, X. Li, D. Xiong, and D. Wang, "A double species23na and87rb bose–einstein condensate with tunable miscibility via an interspecies feshbach resonance," J. Phys. B: At. Mol. Opt. Phys. **49**, 015302 (2015).

[55] D. Xiong, F. Wang, X. Li, T.-F. Lam, and D. Wang, "Production of a rubidium bose-einstein condensate in a hybrid trap with light induced atom desorption," arXiv:1303.0333 .

[56] C. C. Bradley, C. A. Sackett, and R. G. Hulet, "Analysis of in situ images of bose-einstein condensates of lithium," Phys. Rev. A **55**, 3951–3953 (1997).

[57] M. R. Andrews, M.-O. Mewes, N. J. van Druten, D. S. Durfee, D. M. Kurn, and W. Ketterle, "Direct, nondestructive observation of a bose condensate," Science **273**, 84–87 (1996).

[58] D. K. Hoffmann, B. Deissler, W. Limmer, and J. Hecker Denschlag, "Holographic method for site-resolved detection of a 2d array of ultracold atoms," Appl. Phys. B **122**, 227 (2016).

[59] J. Smits, A. P. Mosk, and P. van der Straten, "Imaging trapped quantum gases by off-axis holography," Opt. Lett. **45**, 981–984 (2020).

[60] P. B. Wigley, P. J. Everitt, K. S. Hardman, M. R. Hush, C. H. Wei, M. A. Sooriyabandara, P. Manju, J. D. Close, N. P. Robins, and C. C. N. Kuhn, "Non-destructive shadowgraph imaging of ultra-cold atoms," Opt. Lett. **41**, 4795–4798 (2016).

[61] M. Gajdacz, P. L. Pedersen, T. Mørch, A. J. Hilliard, J. Arlt, and J. F. Sherson, "Non-destructive faraday imaging of dynamically controlled ultracold atoms," Rev. Sci. Instrum. **84**, 083105 (2013).

[62] R. Yamamoto, J. Kobayashi, K. Kato, T. Kuno, Y. Sakura, and Y. Takahashi, "Site-resolved imaging of single atoms with a faraday quantum gas microscope," Phys. Rev. A **96**, 033610 (2017).

[63] K. S. Hardman, P. B. Wigley, P. J. Everitt, P. Manju, C. C. N. Kuhn, and N. P. Robins, "Time-of-flight detection of ultra-cold atoms using resonant frequency modulation imaging," Opt. Lett. **41**, 2505–2508 (2016).

[64] K. E. Wilson, Z. L. Newman, J. D. Lowney, and B. P. Anderson, "In situ imaging of vortices in bose-einstein condensates," Phys. Rev. A **91**, 023621 (2015).

[65] J. H. V. Nguyen, D. Luo, and R. G. Hulet, "Formation of matter-wave soliton trains by modulational instability," Science **356**, 422–426 (2017).

[66] J. Aldegunde, H. Ran, and J. M. Hutson, "Manipulating ultracold polar molecules with microwave radiation: The influence of hyperfine structure," Phys. Rev. A **80**, 043410 (2009).

[67] A. Petrov, C. Makrides, and S. Kotochigova, "External field control of spin-dependent rotational decoherence of ultracold polar molecules," Mol. Phys. **111**, 1731–1737 (2013).

[68] M. Li, A. Petrov, C. Makrides, E. Tiesinga, and S. Kotochigova, "Pendular trapping conditions for ultracold polar molecules enforced by external electric fields," Phys. Rev. A **95**, 063422 (2017).

[69] J. Aldegunde and J. M. Hutson, "Hyperfine structure of alkali-metal diatomic molecules," Phys. Rev. A **96**, 042506 (2017).

[70] M. Guo, X. Ye, J. He, G. Quéméner, and D. Wang, "High-resolution internal state control of ultracold na 23 rb 87 molecules," Physical Review A **97** (2018), 10.1103/PhysRevA.97.020501.

[71] M. Scully and M. Zubairy, *Quantum Optics* (Cambridge University Press, 1997).

[72] R. Vexiau, D. Borsalino, M. Lepers, A. Orbán, M. Aymar, O. Dulieu, and N. Bouloufa-Maafa, "Dynamic dipole polarizabilities of heteronuclear alkali dimers: optical response, trapping and control of ultracold molecules," Int. Rev. Phys. Chem. **36**, 709–750 (2017).

[73] K.-K. Ni, S. Ospelkaus, M. H. G. de Miranda, A. Pe'er, B. Neyenhuis, J. J. Zirbel, S. Kotochigova, P. S. Julienne, D. S. Jin, and J. Ye, "A high phase-space-density gas of polar molecules," Science **322**, 231–235 (2008).

[74] J. T. Zhang, Y. Yu, W. B. Cairncross, K. Wang, L. R. B. Picard, J. D. Hood, Y.-W. Lin, J. M. Hutson, and K.-K. Ni, "Forming a single molecule by magnetoassociation in an optical tweezer," arXiv:2003.07850 .

[75] W. S. Bakr, J. I. Gillen, A. Peng, S. Fölling, and M. Greiner, "A quantum gas microscope for detecting single atoms in a hubbard-regime optical lattice," Nature **462**, 74–77 (2009).

[76] J. J. Hope and J. D. Close, "Limit to minimally destructive optical detection of atoms," Phys. Rev. Lett. **93**, 180402 (2004).

[77] R. Poldy, B. C. Buchler, and J. D. Close, "Single-atom detection with optical cavities," Phys. Rev. A **78**, 013640 (2008).

[78] Z. Chen, J. G. Bohnet, J. M. Weiner, K. C. Cox, and J. K. Thompson, "Cavity-aided nondemolition measurements for atom counting and spin squeezing," Phys. Rev. A **89**, 043837 (2014).

[79] J. Kobayashi, K. Aikawa, K. Oasa, and S. Inouye, "Prospects for narrow-line cooling of krb molecules in the rovibrational ground state," Phys. Rev. A **89**, 021401 (2014).

[80] R. Bause, M. Li, A. Schindewolf, X.-Y. Chen, M. Duda, S. Kotochigova, I. Bloch, and X.-Y. Luo, "Tune-out and magic wavelengths for ground-state ^{23}na^{40}k molecules," arXiv:1912.10452 .

[81] S. Ospelkaus, K.-K. Ni, D. Wang, M. H. G. de Miranda, B. Neyenhuis, G. Quéméner, P. S. Julienne, J. L. Bohn, D. S. Jin, and J. Ye, "Quantum-state controlled chemical reactions of ultracold potassium-rubidium molecules," Science **327**, 853–857 (2010).

[82] A. Arvanitaki, S. Dimopoulos, and K. Van Tilburg, "Resonant absorption of bosonic dark matter in molecules," Phys. Rev. X **8**, 041001 (2018).

[83] A. Kuzmich, N. P. Bigelow, and L. Mandel, "Atomic quantum non-demolition measurements and squeezing," Europhys. Lett. **42**, 481–486 (1998).

[84] A. Kuzmich, L. Mandel, J. Janis, Y. E. Young, R. Ejnisman, and N. P. Bigelow, "Quantum nondemolition measurements of collective atomic spin," Phys. Rev. A **60**, 2346–2350 (1999).

[85] J. Appel, P. J. Windpassinger, D. Oblak, U. B. Hoff, N. Kjærgaard, and E. S. Polzik, "Mesoscopic atomic entanglement for precision measurements beyond the standard quantum limit," Proc. Natl. Acad. Sci. **106**, 10960–10965 (2009).

[86] I. D. Leroux, M. H. Schleier-Smith, and V. Vuletić, "Implementation of cavity squeezing of a collective atomic spin," Phys. Rev. Lett. **104**, 073602 (2010).

[87] W. B. Cairncross, D. N. Gresh, M. Grau, K. C. Cossel, T. S. Roussy, Y. Ni, Y. Zhou, J. Ye, and E. A. Cornell, "Precision measurement of the electron's electric dipole moment using trapped molecular ions," Phys. Rev. Lett. **119**, 153001 (2017).

[88] J. Kobayashi, A. Ogino, and S. Inouye, "Measurement of the variation of electron-to-proton mass ratio using ultracold molecules produced from laser-cooled atoms," Nature Communications **10**, 3771 (2019).

[89] M. Endres, H. Bernien, A. Keesling, H. Levine, E. R. Anschuetz, A. Krajenbrink, C. Senko, V. Vuletic, M. Greiner, and M. D. Lukin, "Atom-by-atom assembly of defect-free one-dimensional cold atom arrays," Science **354**, 1024–1027 (2016).

[90] D. Barredo, S. de Léséleuc, V. Lienhard, T. Lahaye, and A. Browaeys, "An atom-by-atom assembler of defect-free arbitrary two-dimensional atomic arrays," Science **354**, 1021–1023 (2016).

[91] M. Lewenstein, A. Sanpera, V. Ahufinger, B. Damski, A. Sen, and U. Sen, "Ultracold atomic gases in optical lattices: Mimicking condensed matter physics and beyond," Advances in Physics **56**, 243–379 (2007).

[92] I. Bloch, J. Dalibard, and W. Zwerger, "Many-body physics with ultracold gases," Rev. Mod. Phys. **80**, 885–964 (2008).

[93] A. D. Ludlow, M. M. Boyd, J. Ye, E. Peik, and P. O. Schmidt, "Optical atomic clocks," Rev. Mod. Phys. **87**, 637–701 (2015).

[94] C. L. Degen, F. Reinhard, and P. Cappellaro, "Quantum sensing," Rev. Mod. Phys. **89**, 1–39 (2017).

[95] S. Kotochigova and E. Tiesinga, "Controlling polar molecules in optical lattices," Phys. Rev. A **73**, 041405(R) (2006).

[96] O. Docenko, M. Tamanis, R. Ferber, E. A. Pazyuk, A. Zaitsevskii, A. V. Stolyarov, A. Pashov, H. Knöckel, and E. Tiemann, "Deperturbation treatment of the $a\,^1\Sigma^+ - -b\,^3\Pi$ complex of narb and prospects for ultracold molecule formation in $x\,^1\Sigma^+(v = 0; j = 0)$," Phys. Rev. A **75**, 042503 (2007).

[97] M. Aymar and O. Dulieu, "Calculations of transition and permanent dipole moments of heteronucle ar alkali dimers nak, narb and nacs," Mol. Phys. **105**, 1733–1742 (2007).

[98] A. Pashov, O. Docenko, M. Tamanis, R. Ferber, H. Knöckel, and E. Tiemann, "Potentials for modeling cold collisions between na (3s) and rb (5s) atoms," Phys. Rev. A **72**, 062505 (2005).

[99] F. Wang, D. Xiong, X. Li, D. Wang, and E. Tiemann, "Observation of feshbach resonances between ultracold na and rb atoms," Phys. Rev. A **87**, 050702 (2013).

[100] N. V. Vitanov, A. A. Rangelov, B. W. Shore, and K. Bergmann, "Stimulated raman adiabatic passage in physics, chemistry, and beyond," Rev. Mod. Phys. **89**, 015006 (2017).

[101] E. D. Black, "An introduction to pound–drever–hall laser frequency stabilization," American Journal of Physics **69**, 79–87 (2001).

[102] M. Guo, R. Vexiau, B. Zhu, B. Lu, N. Bouloufa-Maafa, O. Dulieu, and D. Wang, "High-resolution molecular spectroscopy for producing ultracold absolute-ground-state ^{23}Na^{87}Rb molecules," Phys. Rev. A **96**, 052505 (2017).

[103] J. Lin, J. He, X. Ye, and D. Wang, "Anisotropic polarizability of ultracold ground-state ^{23}Na^{87}Rb molecules," Phys. Rev. A **103**, 023332 (2021).